Utah State University

# DigitalCommons@USU

8-2018

# Towards the Prediction of Climate Extremes with Attribution Analysis Through Climate Diagnostics and Modeling: Cases from Asia to North America

Boniface Opoku Fosu
*Utah State University*

TOWARDS THE PREDICTION OF CLIMATE EXTREMES WITH ATTRIBUTION

ANALYSIS THROUGH CLIMATE DIAGNOSTICS AND MODELING: CASES

FROM ASIA TO NORTH AMERICA

by

Boniface Opoku Fosu

A dissertation submitted in partial fulfillment
of the requirements for the degree

of

DOCTOR OF PHILOSOPHY

in

Climate Science

Approved:

_____           _____
Shih-Yu S. Wang, Ph.D.                     Robert Gillies, Ph.D.
Major Professor                            Committee Member


_____           _____
Jin-Ho Yoon, Ph.D.                         Brendan M. Buckley, Ph.D.
Committee Member                           Committee Member


_____           _____
Yoshi Chikamoto, Ph.D.                     Mark R. McLellan, Ph.D.
Committee Member                           Vice President for Research and
                                           Dean of the School of Graduate Studies


UTAH STATE UNIVERSITY
Logan, Utah

2018

ABSTRACT

Towards the Prediction of Climate Extremes with Attribution Analysis Through Climate

Diagnostics and Modeling: Cases from Asia to North America

by

Boniface O. Fosu, Doctor of Philosophy

Utah State University, 2018

Major Professor: Dr. Shih-Yu S. Wang
Department: Plants, Soils, and Climate

This work is focused on extreme climate detection, attribution and predictions. Three interrelated, yet regionally unique climate phenomena were investigated to characterize changes in the variability of climate that lead to extremes. This was augmented by the development of tools to supplement the prediction of climate extremes on the subseasonal to interannual timescales.

First, the impact of anthropogenic climate change on atmospheric stability and aerosol concentration in basin terrain was investigated, with a specific focus on the IndoGangtic Plains (IGP). This was achieved by utilizing an empirical diagnostics methodology paired with the direct simulation of aerosols. It was found that the winter atmosphere in the IGP is becoming more stable, attributable to both greenhouse gases (GHG's) and aerosols. Since a more stable atmosphere traps more aerosols, it is shown that aerosols in the IGP can increase in the absence of a change in their emission sources, which is a process caused by increased anthropogenic GHG that was previously not realized.

Furthermore, a positive feedback exits whereupon aerosol-induced stabilization increases the accumulation of aerosols in the IGP.

The second part of this work evaluated the 2014/15 cold season snowpack drought in Washington state and its climate forcing. The so-called snowpack drought in Washington state resulted from unprecedented warmth that caused cold season precipitation to fall as rain rather than snow in the mountain ranges of Washington State. Synoptic attribution analysis revealed that a significant portion of the circulation anomalies associated with the drought emanated from naturally driven North Pacific climate variability in the form of the North Pacific Index (NPI) with modulation from the North Pacific Oscillation. Notwithstanding, anthropogenic warming, acted to exacerbate the impacts of the drought. In addition, a unique cyclical relationship between temperature and precipitation (averaged along the mountain ranges of Washington - Cascades) was uncovered that is apparently driven by the low frequency variability of the NPI.

Next, we analyzed the synoptic-scale mechanisms and attribution of extreme precipitation events in the central US, focusing on three days of extreme rainfall in late December 2015 that led to severe flooding along the Mississippi river with Missouri being the most impacted. The meteorological context of this event was analyzed, as well as the synoptic diagnosis and forecast attribution of the atmospheric circulation that contributed to the event's severity. The midlatitude synoptic waves that led to the extreme precipitation and ensuing flooding were traced to the Madden Julian Oscillation (MJO), which had an amplification effect on the trans-Pacific Rossby wave train likely associated with the strong El Niño of December 2015. The influence of anthropogenic climate change on the relationship between the El Niño Southern Oscillation (ENSO) and precipitation across the

Central US was also assessed using single forcing experiments of several models that participated in the Coupled Model Intercomparison Project (CMIP5). The models revealed an apparent regime change in ENSO-related precipitation anomalies across the central US, suggesting a likely amplification effect of anthropogenic warming on the December event. Through the analysis of NCEP's Climate Forecast System (CFSv2), it was also determined that when it comes to the MJO skillful subseasonal predictions with lead times exceeding two weeks are rarely achievable.

Lastly, the mechanisms linking the onset of the El Nino-Southern Oscillation to two North Pacific ENSO precursor patterns, i.e. the Western North Pacific mode (WNP) and the Pacific Meridional Mode (PMM) a year in advance were studied using a decomposition of the upper ocean mixed layer (SST) budget, coupled with the mass streamfunction representation of the Pacific Walker Circulation. Strong upward equatorial heat flux anomalies and advection occur in concert with a warming SST in both the WNP and the PMM during the development of an El Niño (sign reversed for La Nina), illustrating how the WNP and PMM are inherently linked to equatorial ocean dynamics and the dominant mechanisms that lead to SST changes during ENSO development. In the early stages of ENSO development, equatorial SST anomalies lag heat fluxes by about a season while the development of the PMM generally lags the WNP by another season. In comparison to the PMM, the WNP has a more robust temporal and spatial relationship with the Pacific Walker circulation, which is an inherent part of ENSO variability.

(142 pages)

PUBLIC ABSTRACT

Towards the Prediction of Climate Extremes with Attribution Analysis Through Climate

Diagnostics and Modeling: Cases from Asia to North America

Boniface O. Fosu

This project summarizes the findings of research organized in two parts. The first involved the characterization of changes in the variability of climate that lead to extreme events. The second focused on the predictability of extreme climate on time-scales ranging from short forecast lead-times to long-lead climate predictions exceeding a year.

Initial studies focused on three interrelated, yet regionally unique extreme climate phenomena. First, the relationship between increasing greenhouse gas (GHG) emissions and particulate matter (PM) concentration in basin terrain was investigated. Next, we evaluated changes in large-scale atmospheric circulation associated with two climate phenomena at either extreme side of the water cycle -- droughts and floods. In the final analysis, an attempt was made to understand the mechanisms that link two North Pacific ENSO precursor patterns to the ENSO cycle.

# ACKNOWLEDGMENTS

CONTENTS

LIST OF TABLES

LIST OF FIGURES

LIST OF ACRONYMS

| Acronym | | Meaning |
|---|---|---|
| 1 | CESM. | Community Earth System Model |
| 2 | CESM-LENS. | CESM-Large Ensemble Project |
| 3 | CFSR. | Climate Forecast System Reanalysis |
| 4 | CMIP5. | Coupled Model Intercomparison Project Phase 5 |
| 5 | ENSO | El Niño-Southern Oscillation |
| 6 | IGP. | IndoGangetic Plains |
| 7 | IndO. | Northern/Tropical Indian Ocean |
| 8 | IPCC. | Intergovernmental Panel on Climate Change |
| 9 | NCEP | National Center for Environmental Prediction |
| 10 | NCAR. | National Center for Atmospheric Research |
| 11 | MJO. | Madden-Julian Oscillation |
| 12 | MCA. | Maximum Covariance Analysis |
| 13 | NPO. | North Pacific Oscillation |
| 14 | PMM. | Pacific Meridional Mode |
| 15 | PWC. | Pacific Walker Circulation |
| 16 | S2S. | Subseasonal-to-Seasonal |
| 17 | SST. | Sea Surface Temperature |
| 18 | SSTA. | Sea Surface Temperature Anomalies |
| 19 | WRF. | Weather Research and Forecasting model |
| 20 | WRF-Chem. | WRF model coupled with Chemistry |
| 21 | WNP | Western North Pacific |
| 22 | WWV | Warm Water Volume |

CHAPTER 1

INTRODUCTION

The Intergovernmental Panel on Climate Change defines an extreme event as the occurrence of a value of a weather or climate variable above (or below) a threshold value near the upper (or lower) ends ('tails') of the range of observed values of the variable. Some climate extremes (e.g., droughts, floods) may be the result of an accumulation of weather or climate events that are, individually, not extreme themselves (though their accumulation is extreme). Even if not extreme in a statistical sense, weather or climate events can still lead to extreme conditions, either by crossing a critical threshold in a physical system, or by occurring simultaneously with other events. A weather system such as a tropical cyclone can have an extreme impact, depending on where and when it approaches landfall, even if the specific cyclone is not extreme relative to other tropical cyclones (Seneviratne et al., 2012).

Whiles weather and climate extremes have always happened, there is a growing scientific consensus that they are becoming more frequent and destructive. Different types of research approaches taken, including statistical analysis of observed data, climate modelling and physical reasoning have strongly attributed these changes to human-induced climate change (Hay and Mimura 2010, Rodriguez et al., 2009, Coumou and Rahmstorf 2012). Notwithstanding, the extent to which a given extreme weather or climate event is attributed, especially to anthropogenic climate change is often very challenging from a physical standpoint (e.g. Stott et al. 2016).

If a weather or climate event is truly extreme in the present climate, then it requires unusual meteorological conditions, meaning climate change could be at most only a contributing factor (Shepherd 2016). The failure to recognize this fact can lead to apparently contradictory conclusions concerning the same event (Otto et al. 2012). Yet, even a small contributing factor can have enormous consequences in the context of an extreme event. The scientific question is then to determine that contribution – this requires a fundamental understanding of the mechanisms that link specific extreme weather and climate events to human induced climate change without undermining the role of natural climate variability.

The above literature is a summary of the viewpoints that have led to the overarching goal of this work, that is: to investigate how notable changes in the variation in the mean state of climate are dynamically linked to the occurrence of extreme weather and climate, while testing the suitability or otherwise of conventional attribution methods, generating a baseline level of understanding and skill for the improvement numerical weather and climate models, as well as predictions. Through the application of a variety of climate data, climate diagnostic methods, dynamical and statistical techniques, and climate modelling, the following objectives are addressed to accomplish the main goal.

**Objectives**

1. To identify large-scale atmospheric and oceanic features at appropriate spatial and temporal scales that connect to cyclical variations in wet and dry climate.

2. To characterize changes in climate variability and their links to extremes of weather and climate.

3. The development of meaningful tools to supplement the prediction of climate extremes on the subseasonal to seasonal timescales, as well as long range predictions exceeding a year.

**References**

Coumou D and Rahmstorf S. 2012. A decade of weather extremes. Nature Climate Change 2, 491-496

Hay J and Mimura N. 2010. The changing nature of extreme weather and climate events: risks to sustainable development. Geomatics, Natural Hazards and Risk, 1:1, 3-18

IPCC (2007) Summary for Policymakers. Climate Change 2007. The Physical Science Basis, 2007 Working Group I Contribution to IPCC Fourth Assessment Report: Climate Change 2007, Geneva

Otto FEL, Massey N, van Oldenborgh GJ, Jones RG, Allen MR. Reconciling two approaches to attribution of the 2010 Russian heat wave. 2012. Geophys Res Lett. 39:L04702.

Seneviratne SI, Nicholls N, Easterling D, Goodess CM, Kanae S, Kossin J, Luo Y, Marengo J, McInnes K, Rahimi M, Reichstein M, Sorteberg A, Vera C and Zhang X. 2012. Changes in climate extremes and their impacts on the natural physical environment. In: Managing the Risks of Extreme Events and Disasters to Advance Climate Change Adaptation [Field CB and coauthors (eds.)]. A Special Report of Working Groups I and II of the Intergovernmental Panel on Climate Change (IPCC). Cambridge University Press, Cambridge, UK, and New York, NY, USA, pp. 109-230.

Shepherd TG. 2016. A common framework for approaches to extreme event attribution. Curr Clim Change Reports 2:28–38.

Stott PA, Christidis N, Otto FEL, Sun Y, Vanderlinden J-P, van Oldenborgh GJ, Vautard R, von Storch H, Walton P, Yiou P, Zwiers FW. 2016. Attribution of extreme weather and climate-related events. WIREs Clim. Change 7: 23 – 41

Rodriguez J, Vos F, Below R and Guha-Sapir D. 2009. Annual Disaster Statistical Review 2008: The numbers and trends. Centre for Research on the Epidemiology of Disasters (CRED), Universite´ catholique de Louvain, Brussels, Belgium, 33 pp

CHAPTER 2

GREENHOUSE GASES STABILIZING WINTER ATMOSPHERE IN THE INDO-
GANGETIC PLAINS MAY INCREASE AEROSOL LOADING[1]

ABSTRACT

The concentration of aerosols along the Indo-Gangetic Plains (IGP) and their adverse effects on human health and the environment are increasing. In winter, the IGP is prone to high anthropogenic aerosol loading (i.e. particulate matter - PM). In this study, three reanalysis datasets including the MERRA Aerosol Reanalysis were analyzed to characterize the relationship between winter atmospheric stability and aerosols. Due to the lack of long-term aerosol observations, an empirical relationship between PM and the atmospheric temperature lapse rate was derived. It is shown that PM and stability have a strong relationship at the lower troposphere. Analyses of CMIP5 single-forcing experiments indicate that the recent stabilization of the atmosphere in the IGP can be explained by both greenhouse gas and (GHG) aerosol forcing. Since a more stable atmosphere traps more PM, stabilization alone can increase aerosols even in the absence of changes in emission sources. Regional simulation with fixed anthropogenic aerosol loading also supports this finding. Thus, enhanced stabilization caused by both aerosols and GHG in the atmosphere can further increase winter aerosol loading in the IGP.

---

## 1. Introduction

In recent decades, the Indo-Gangetic Plains (IGP) has become a hotspot of rising anthropogenic aerosol emissions, as evidenced by measurements of moderate resolution imaging spectroradiometer (MODIS) aerosol optical depth (AOD) – Figure 1a, and remarked upon by various studies (Vijayakumar et al., 2007; Kar et al., 2010). The increased concentration of anthropogenic aerosols, coupled to their bearing on climate change and effect on human health, has resulted in a marked proliferation of research into atmospheric aerosols. Past studies (Gautam et al., 2011; Srivastava et al., 2012) have found that the concentration of anthropogenic aerosols in the IGP is not as straightforward as a function of source, but is complicated by topography and seasonality; this is akin to what occurs with particulate matter (PM) (e.g. PM2.5) in many terrain basins (Gillies et al., 2010; Wang et al., 2012).

The winter months within the IGP feature a stable boundary layer due to cool temperatures and weak ambient wind flow [November–January, Figure 1c], hence the potential for high-aerosol loading; this being contrary to the summer monsoon season where high temperatures accompany strong monsoonal winds [May–July, Figure 1b]. Aerosol measurements, using the angstrom exponent of aerosols that increases with decreasing size (Figure 2), reveal that the make-up of atmospheric aerosols in the IGP do indeed vary seasonally – i.e. smaller aerosols (e.g. black carbon) are predominant in winter and larger ones (e.g. dust) in summer. The large extent of human induced (anthropogenic) aerosols in winter therefore underscores the importance of studying any corresponding changes in the local climate. Moreover, when it comes to under- standing the IGP's aerosol sensitivity to the changing atmospheric thermal structure driven by anthropogenic global

warming, a lack of systematic research coupled to the paucity of a long-term observational aerosol data record is problematic; this motivated the research undertaken and presented here.

In this study, we utilized atmospheric and aerosol reanalysis data in conjunction with climate model out- puts to characterize atmospheric stability and examine the relationship between atmospheric stability conditions and anthropogenic aerosols. The diagnostic analyses were followed by the derivation of an empirical relationship between atmospheric aerosol loading and stability, which subsequently was used to quantify the concentration of aerosols in the IGP, and how it interacts with changing atmospheric stabilization.

## 2. Data and Methods

### 2.1. Data Sources

The following reanalysis datasets were utilized: the ERA-Interim reanalysis (Dee et al., 2011), the University of Delaware (UDEL) precipitation datasets (Willmott and Matsuura, 2001), NASA's MERRA (Rienecker et al., 2011), and the NCEP/NCAR 40-year reanalysis datasets (Kalnay et al., 1996). For attribution, 11 models that participated in the Coupled Model Intercomparison Project (CMIP5) (Taylor et al., 2012) were used. These single-forcing experiments only go up to 2005. Table 1 details the acronym, full name, and full description of each model.

Data from the space borne MODIS instrument (Hsu et al., 2004) and the Aerosol Robotic network (Holben et al., 1998) were used for the depiction of aerosol loading and proper- ties. We also examined PM derived from the MERRA Aerosol Reanalysis

(MERRAero) (Rienecker et al., 2011) from 2003 to 2013. In MERRAero, PM can be obtained from the surface mass concentrations of dust, sulfate (SO), black carbon (BC), organic carbon and sea salt. Over the IGP, SO and BC emissions are significantly higher in the winter than in the summer; this is due to differences in weather and industrial activity. This article focuses on the relationship between 'anthropogenic aerosol' emissions and stability for the period defined as 'winter', therefore dust was excluded from the analysis to minimize possible biases.

## 2.2. Methodology

The study area along the IGP is outlined in Figure 1a; this area features particularly large aerosol loadings due to its high-population density. Given the maxi- mum PM in the seasonality of the IGP, we focused on the winter months of November and December (ND). To depict atmospheric stability, we used lapse rate, as it is directly relevant to vertical motion and, subsequently, the dispersion and concentration of aerosols in the atmosphere. Both the actual (T) and potential temperature ($\theta$) were used to compute lapse rate (i.e. $-d\theta[T]/dp$). To make compositing possible, all utilized reanalysis datasets were regridded onto the same 2.5∘ grid spacing using a third order Bessel interpolation. Attribution involved repetition of the lapse rate analysis with different forcing composites of CMIP5 model out- puts. To test the evolution of PM concentrations in the IGP without time-varying anthropogenic aerosol emissions, the Weather Research and Forecasting model coupled with Chemistry (WRF-Chem) version 3.8.1 (Grell et al., 2005) was used. The experimental setup, main physics and chemical schemes used for the simulations are listed in Table 2.

**3. Results and Discussion**

3.1. Instability

Figure 3 shows the changes in the atmospheric stability displayed as vertical profiles of lapse rate anomaly as a function of time. Linear trends at each pressure level, computed as the least square best fit to the lapse rate over the entire underlying period of 35 years, are overlaid in contours. The climatological mean of the lapse rate was removed prior to computations to depict year-to-year changes. As a consequence of removing the long-term mean, one is able to observe two distinct periods in variability, i.e. one in the past centered around the 1990s that is indicative of a period that is less atmospherically stable, compared to the other centered around 2010 where the situation is reversed. All the three reanalysis datasets (Figures 3a–c) indicate the development of increasingly atmospheric stable conditions from the surface to about 700 hPa. Also evident is a similar occurrence in the middle-to-upper troposphere with the exception of NCEP1 (Figure 3a). Regardless of marginal distinctions between the three observational datasets, a consistent picture arises from the composite plot (Figure 3d), one that signals a stability modification for the entire troposphere. In other words, a shift has occurred, one from a climatologically stable winter atmosphere environment to one of greater stability; this implies extended or strengthened winter temperature inversions over the IGP.

To attribute the shift in the observed lapse rates, we analyzed a composite of 11 CMIP5 models. Due to the limited temporal extent of CMIP5 data (up to 2005), only a comparable 35-years time span (i.e. 1970–2005) with respect to the reanalysis datasets was used: Starting with the natural runs (Figure 3e), there is no clear-cut shift toward increased

atmospheric stability as the lapse rate anomalies tend toward neutrality – this is not surprising due to the cancelation of natural variability among the different simulations over time. The greenhouse gas (GHG) forcing (Figure 3f) runs do, however, reveal a similar interdecadal shift in comparison with that in Figure 3d toward a more pronounced stable atmosphere in the middle-to-upper troposphere around 2005. The modeled GHG forcing is not particularly synchronous with the observations, as a more stable atmosphere develops much earlier than that observed despite the same direction. This is expected, however, since the GHG-only forcing would induce more pronounced warming than the observation, enhancing the stabilization effect earlier.

In the aerosol run (Figure 3g), an increasingly stable boundary layer is also present, with corresponding positive (and somewhat accelerated) trends in most of the troposphere. The combination of all three forcings (Figure 3h), i.e. the ensemble (ALL or historical experiment) scenarios, results in uniform stabilization throughout the tropospheric column, but once again, it reflects a disparity with the reanalysis composite (Figure 3d) in the timing of the shift in stability, i.e. about a decade earlier. Apparently, the models tend to also overestimate stabilization in the middle tropo- sphere in comparison to the reanalysis. Nevertheless, the observations are clear as to the change that has occurred and the CMIP5 results suggest that there is an effect to enhanced stabilization that partly lies in anthropogenic GHG's and aerosols.

Caution is necessary here in interpreting the model results. The CMIP5 free runs cannot be compared to calendar years, and aerosol effects are only partially represented in the majority of the models (e.g. Kiehl, 2007). Even models that include atmospheric chemistry modules have shown large uncertainties in aerosols (e.g. Kinne et al., 2006).

3.2. Empirical Assessment of Aerosols

Since most CMIP5 models do not have built-in inter- active or dynamic aerosol modules, and given that the time span of available aerosol data is limited, an empirical modeling approach serves as a means to estimate long-term regional aerosol levels. Hence, we derived a statistical relationship between PM and lapse rate using linear regression, following Wang et al., 2015. The choice of an optimal lapse rate level for temperature was achieved by averaging between the 925 and 800 hPa levels. Several tests with different instability indices (Figure 4) revealed that any correspondence of PM with lapse rate diminishes somewhat beyondv700 hPa, consistent with the finding of Mishra and Shibata (2012). It is worth noting that the use of either actual or potential temperature does not change the relationship between PM and instability at lower altitudes.

Figure 5a shows a scatter plot between PM anomaly and lapse rate at the optimal level for both actual ($\Delta$T) and potential ($\Delta\boldsymbol{\theta}$) temperatures over time. Long-term trends were first removed to minimize anthropogenic sources and interdecadal variability. From the regression in Figure 5a, it is clear that PM [y(t)] and lapse rate [x(t)] exhibit a good linear relationship. Overall, the inter-comparison shows a close agreement between the two variables as indicated by the moderate-to-strong correlation. In fact, the large spatial extent of the datasets used, coupled to the relatively large size of the domain lend confidence to the strong statistical association.

Using the linear regression model (Figure 5a), it is possible to reconstruct $\Delta$PM [y(t)] as a function of lapse rate [x(t)], where lapse rate is the proxy for inferring stability or otherwise. To do this, we used lapse rate data at selected pressure levels, extracted from the four CMIP5 forcing composites (Figures 5b–e). From the reconstruction, we can infer

past PM levels and changes in PM concentration under different climate forcing experiments. In the HISTORICAL-forcing (Figure 5b) scenario, PM increases with time and appears driven by both increasing GHG (Figure 5d) and aerosols (Figure 5e). For the natural conditions (Figure 5c), there is little to no change. The most striking trend revealed is in Figure 5d, which suggests that under GHG forcing, the concentration of aerosols in the IGP would continue to rise assuming PM emission sources remained constant – this is a possibility that was hitherto unknown.

3.3. Direct Simulation of Aerosols

One might recall that, apart from aerosols them- selves, GHG's can also induce stabilization in the IGP (Figure 3f). Stable atmospheric conditions inhibit the dispersion of aerosols through vertical mixing leading to the accumulation of more particulates – even with constant PM source emissions. To corroborate the empirically derived PM and the associated increases as shown in Figure 5, we performed the aforementioned WRF-Chem experiment whereupon anthropogenic aerosol emissions were set constant at the year 2000 level while GHG concentrations and warming continued. The simulated PM, which is shown in Figure 6, exhibits a clear increase even without the time-varying anthropogenic aerosols. The marked interannual variability also indicates that PM does undergo climatic modulations in the region. Both the climate effect and the GHG-induced warming can be seen in the simulated temporal evolution of temperature lapse rate anomaly in the IGP, plotted in Figure 6 alongside the simulated PM.

The WRF-Chem simulation lends support to the notion that increasing GHG emissions as a singular factor can lead to a consequent increase in PM concentrations. In

the same way, PM rise (Figure 5e) results in aerosol-induced stabilization (Figure 3g), which induces a positive feedback and so, traps more aerosols in the boundary layer – a known phenomenon (Lau et al., 2005). Another implication from the long-term trends is that GHG's have a longer atmospheric residence time and so, prolongs atmospheric stability conditions enhancing aerosol loading.

3.4. Other Measures

Several variables were analyzed to show seasonal synoptic changes in the IGP, which primarily serve as validation for the outcome of the earlier lapse rate computations. Figure 7 shows the seasonal long-term changes (slope) in 800 hPa potential temperature. The atmosphere appears to have warmed up significantly in winter (Figure 7a) in contrast to a net cooling in summer (Figure 7c). Furthermore, we analyzed the slopes of winter precipitation and 2-m temperatures (T2m) within 2 different periods of time: precipitation is observed to have declined over the last 34 and 20 years (Figure 8a), along with surface cooling (Figure 8b).

Concomitant to the rainfall decline is the hypothesis that aerosols increase the lifetime of clouds inducing an increase in the concentration of smaller droplets, which in turn lead to decreased drizzle production and reduced precipitation efficiency (Bollasina et al., 2008; Ganguly et al., 2012). The impact of aerosols on precipitation is by no means a straightforward conclusion. It is important to note studies such as Kim et al. (2016) that have associated the high concentration of aerosols over northern India to enhanced rainfall in the late spring and early monsoon months, followed by a suppression of monsoon rainfall over all of India. This is consistent with the elevated heat pump hypothesis by Lau et al.

(2005). The vast extent of the deduction such as we have discussed illustrates the complexity of aerosol forcing on climate, and under- scores the need for more research to be conducted in this area.

Also apparent is a reduction in T2m (Figure 8b), which together with the decreasing IGP precipitation are aligned with increased aerosol concentrations and enhanced stability conditions (Figures 3a–h), especially at lower altitudes. The surface cooling (Figure 8b) coupled to a warming trend aloft (Figure 7a) is not consistent with a normal environmental lapse rate of decreasing temperature with height, and therefore reinforces the inferences of a more stable atmosphere. The results presented here suggest that the trapping of light absorbing aerosols (e.g. BC) through the enhancement of a thermal inversion layer suppresses boundary layer convection, and is consequential as it constrains vertical motion. Consequently, the light absorbing aerosols aloft serve to strengthen the inversion cap on the boundary layer through warming, and may feedback to cool the surface (Markowicz, 2003), increasing the stability of the troposphere. The upshot is the trapping of more aerosols especially so in basin-type terrain.

## 4. Conclusion

The research presented here looked at aerosol-climate interactions in the context of regional climate change. The study involved the interactions between winter aerosols in the IGP and atmospheric stability using several reanalysis datasets and CMIP5 models outputs. The lapse rate analysis across the IGP shows that the atmosphere is becoming more stable, and both GHG's and aerosols have a role in this stabilization. Through an empirical model approach and WRF-Chem simulation, it is shown that aerosols/PM in the

IGP can increase in the absence of a change in their emission sources – a process caused by increased anthropogenic GHG that was previously not realized. Moreover, a positive feedback exits whereupon aerosol-induced stabilization increases the accumulation of PM. Collectively the consequences of a warming atmosphere is in the modulation of aerosol concentrations compounded by the IGP's basin-like orography. In the face of increasing anthropogenic GHG's, aerosol loading in the region will worsen whereupon exacerbation of pollution and winter smog should be a future expectation.

**References**

Bollasina M, Nigam S, Lau KM. 2008. Absorbing aerosols and sum- mer monsoon evolution over South Asia: an observational portrayal. Journal of Climate 21: 3221–3239.

Dee DP, Uppala SM, Simmons AJ, Berrisford P, Poli P, Kobayashi S, Andrae U, Balmaseda MA, Balsamo G, Bauer P, Bechtold P, Bel- jaars ACM, van de Berg L, Bidlot J, Bormann N, Delsol C, Dragani R, Fuentes M, Geer AJ, Haimberger L, Healy SB, Hersbach H, Hólm EV, Isaksen L, Kållberg P, Köhler M, Matricardi M, McNally AP, Monge-Sanz BM, Morcrette J-J, Park B-K, Peubey C, de Rosnay P, Tavolato C, Thépaut J-N, Vitart F. 2011. The ERA-Interim reanal- ysis: configuration and

performance of the data assimilation system. Quarterly Journal of the Royal Meteorological Society 137: 553–597.

Ganguly D, Rasch PJ, Wang H, Yoon J-H. 2012. Climate response of the South Asian monsoon system to anthropogenic aerosols. Journal of Geophysical Research 117: D13209.

Gautam R, Hsu NC, Tsay SC, Lau KM, Holben B, Bell S, Smirnov A, Li C, Hansell R, Ji Q, Payra S, Aryal D, Kayastha R, Kim KM. 2011. Accumulation of aerosols over the Indo-Gangetic plains and southern slopes of the Himalayas: distribution, properties and radiative effects during the 2009 pre-monsoon season. Atmospheric Chemistry and Physics 11: 12841–12863.

Gillies RR, Wang S-Y, Yoon J-H, Weaver S. 2010. CFS prediction of winter persistent inversions in the intermountain region. Weather and Forecasting 25: 1211–1218.

Grell GA, Peckham SE, Schmitz R, McKeen SA, Frost G, Skamarock WC, Eder B. 2005. Fully coupled "online" chemistry within the WRF model. Atmospheric Environment 39(37): 6957–6975.

Holben BN, Eck TF, Slutsker I, Tanré D, Buis JP, Setzer A, Vermote E, Reagan JA, Kaufman YJ, Nakajima T, Lavenu F, Jankowiak I, Smirnov A. 1998. A federated instrument network and data archive for aerosol characterization. Remote Sensing of Environment 60: 1–16.

Hsu NC, Tsay SC, King MD, Herman JR. 2004. Aerosol properties over bright-reflecting source regions. IEEE Transactions on Geoscience and Remote Sensing 42: 557–569.

Kalnay E, Kanamitsu M, Kirtler R, Collins W, Deaven D, Gandin L, Iredell M, Saha S, White G, Woollen J, Zhu Y, Chelliah M, Ebisuzaki W, Higgins W, Janowiak J, Mo

KC, Ropelewski C, Wang J, Leetma A, Reynolds R, Jenne R, Joseph D. 1996. The NCEP/NCAR 40-year reanalysis project. Bulletin of the American Meteorological Society 77: 437–471.

Kar J, Deeter MN, Fishman J, Liu Z, Omar A, Creilson JK, Trepte CR, Vaughan MA, Winker DM. 2010. Wintertime pollution over the Eastern Indo-Gangetic Plains as observed from MOPITT, CALIPSO and tropospheric ozone residual data. Atmospheric Chemistry and Physics 10: 12273–12283, doi: 10.5194/acp-10-12273-2010.

Kiehl JT. 2007. Twentieth century climate model response and climate sensitivity. Geophysical Research Letters 34: 1–4.

Kim MK, Lau WK, Kim KM, Sang J, Kim YH, Lee WS. 2016. Ampli- fication of ENSO effects on Indian summer monsoon by absorbing aerosols. Climate Dynamics 46: 1–15.

Kinne S, Schulz M, Textor C, Guibert S, Balkanski Y, Bauer SE, Berntsen T, Berglen TF, Boucher O, Chin M, Collins W, Dentener F, Diehl T, Easter R, Feichter J, Fillmore D, Ghan S, Ginoux P, Gong S, Grini A, Hendricks J, Herzog M, Horowitz L, Isaksen I, Iversen T, Kirkevåg A, Kloster S, Koch D, Kristjansson JE, Krol M, Lauer A, Lamarque JF, Lesins G, Liu X, Lohmann U, Montanaro V, Myhre G, Penner JE, Pitari G, Reddy S, Seland O, Stier P, Takemura T, Tie X. 2006. An AeroCom initial assessment – optical properties in aerosol component modules of global models. Atmospheric Chemistry and Physics 6: 1815–1834.

Lau K-M, Kim K-M, Hsu C. 2005. Observational evidence of effects of absorbing aerosols on seasonal-to-interannual anomalies of the Asian monsoon. CLIVAR Exchanges 10(3): 7–9.

Markowicz KM. 2003. Influence of relative humidity on aerosol radia- tive forcing: an ACE-Asia experiment perspective. Journal of Geo- physical Research 108: 8662.

Mishra AK, Shibata T. 2012. Climatological aspects of seasonal vari- ation of aerosol vertical distribution over central Indo-Gangetic belt (IGB) inferred by the space-borne lidar CALIOP. Atmospheric Envi- ronment 46: 365–375.

Rienecker MM, Suarez MJ, Gelaro R, Todling R, Bacmeister J, Liu E, Bosilovich MG, Schubert SD, Takacs L, Kim G-K, Bloom S, Chen J, Collins D, Conaty A, da Silva A, Gu W, Joiner J, Koster RD, Lucchesi R, Molod A, Owens T, Pawson S, Pegion P, Redder CR, Reichle R, Robertson FR, Ruddick AG, Sienkiewicz M, Woollen J. 2011. NASA's modern-era retrospective analysis for research and applications. Journal of Climate 24: 3624–3648.

Srivastava A, Dey S, Tripathi SN. 2012. Aerosol Characteristics over the Indo-Gangetic Basin: Implications to Regional Climate. In Atmo- spheric Aerosols - Regional Characteristics – Chemistry and Physics, Abdul-Razzak H (ed). Intech Publishers, doi: 10.5772/47782.

Taylor KE, Stouffer RJ, Meehl GA. 2012. An overview of CMIP5 and the experiment design. Bulletin of the American Meteorological Society 93: 485–498.

Vijayakumar SN, Moorthy KK, Alappattu DP, Kunhikrishnan PK, George S, Nair PR, Babu SS, Abish B, Satheesh SK, Tripathi SN, Niranjan K, Madhavan BL, Srikant V, Dutt CBS, Badarinath KVS, Reddy RR. 2007. Wintertime aerosol characteristics over

the Indo-Gangetic Plain (IGP): impacts of local boundary layer pro- cesses and long-range transport. Journal of Geophysical Research 112: D13205, doi: 10.1029/2006JD008099.

Wang SY, Gillies RR, Martin R, Davies RE, Booth MR. 2012. Connect- ing subseasonal movements of the winter mean ridge in western North America to inversion climatology in Cache Valley, Utah. Journal of Applied Meteorology and Climatology 51: 617–627.

Wang S-Y, Hipps L, Chung O-Y, Gillies RR, Martin R. 2015. Long-term winter inversion properties in a mountain valley of the western U.S. and implication on air quality. Journal of Applied Meteorology and Climatology 54(12): 2339–2352.

Willmott CJ, Matsuura K. 2001. Terrestrial air temperature and pre- cipitation: monthly and annual time series (1950–1999). http:// climate.geog.udel.edu/ (accessed 7 March 2016).

**Figures**
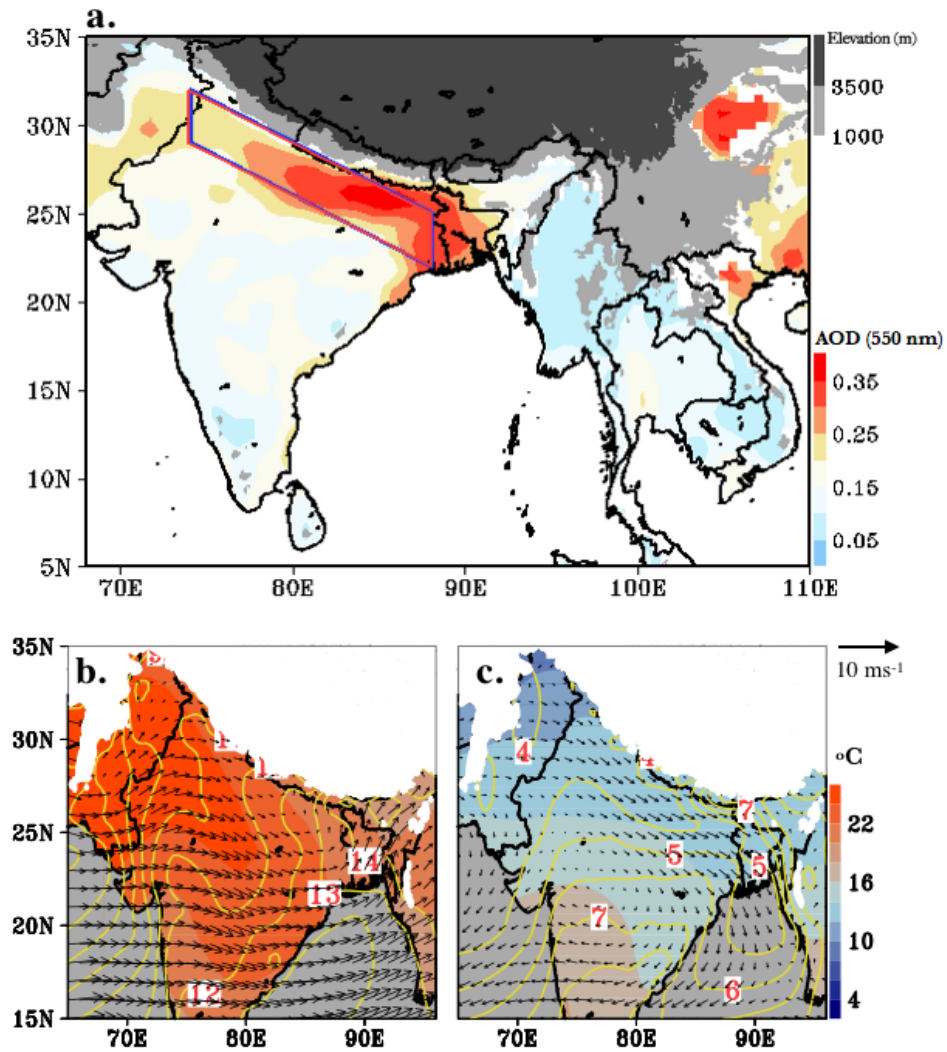


**Figure 2-1 a)** Mean (2003-2012) MODIS aerosol optical depth. The section of the IndoGangetic Plains under investigation is delineated by the red box. **b)** Mean (1979-2014) meteorological conditions (ERA-I) in summer, and **c)** winter. Specific humidity is contoured (gkg$^{-1}$), 850 hPa air temperature is shaded ($^{o}$C), and wind fields are superimposed as vectors (ms$^{-1}$)
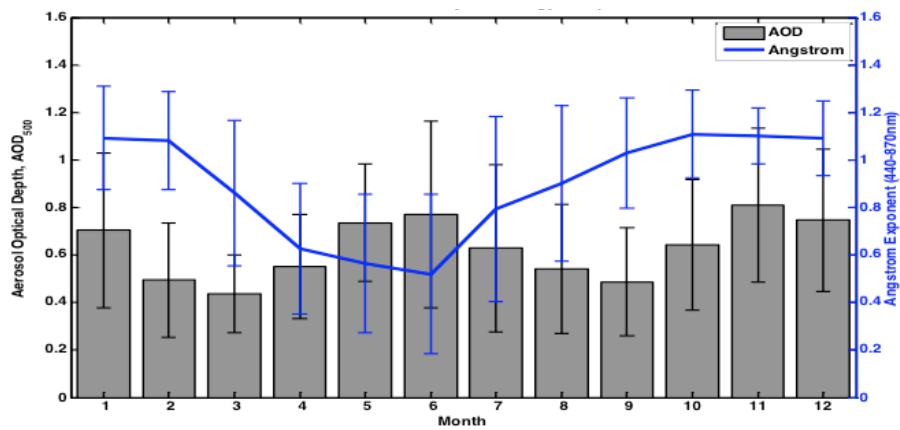
**Figure 2-2** Monthly climatology of aerosol optical depth and angstrom exponent from 2000-2012 (AERONET).
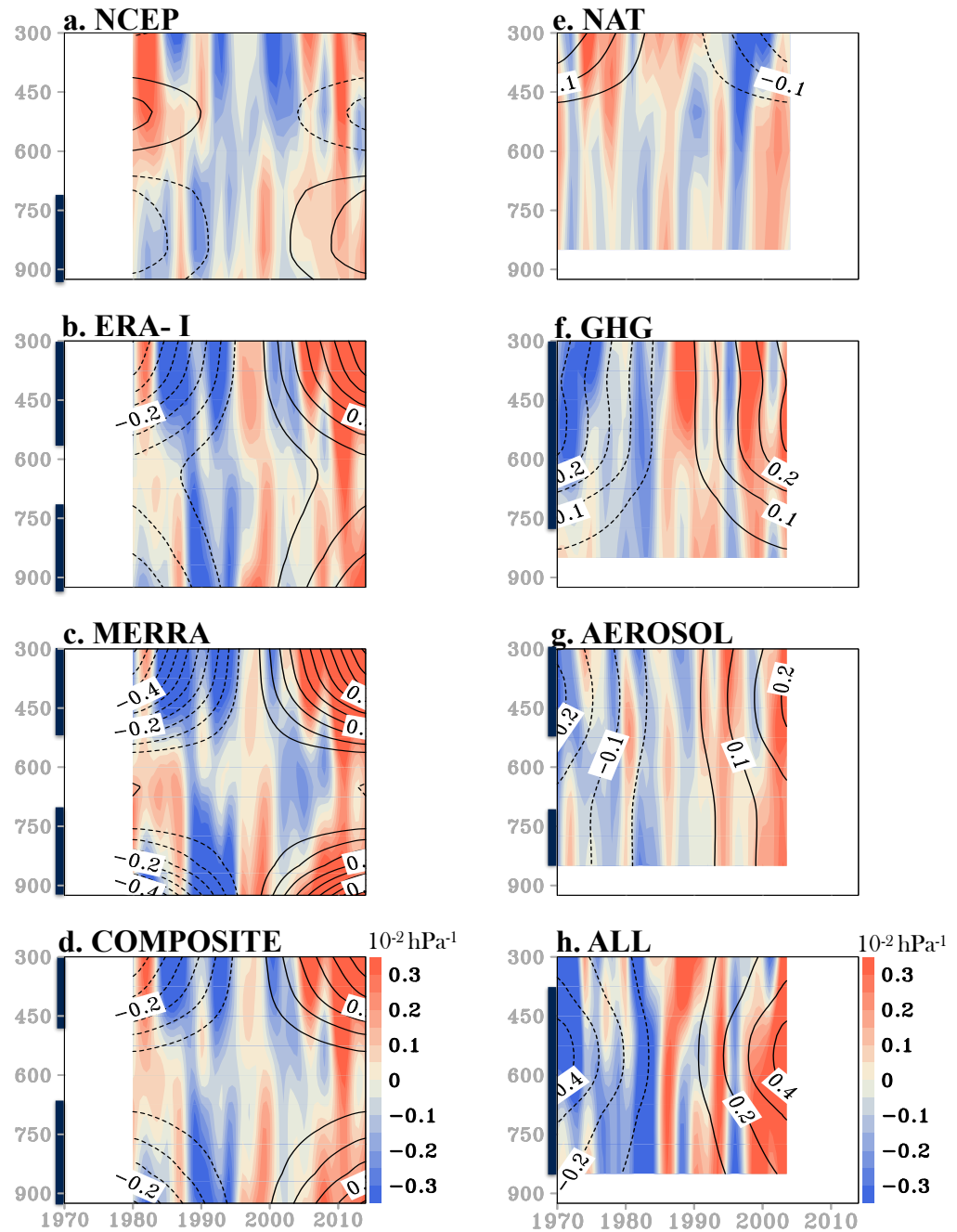
**Figure 2-3** a-d) Domain averaged changes in mean Nov-Dec lapse rate anomalies (Δ[-dθ/dp]) (shading). Liner trends in Δ[-dθ/dp] are displayed here as black contours with an interval of 0.1 10-2 hPa-1. The thick (dotted) black contours are positive (negative) trends in lapse rate, indicative of an increase (a decrease) in stability during the underlying periods. e-h) Same as previous plot but for different CMIP5 forcing runs. Each plot is an ensemble of 11 models, comprising each models' maximum available members. The thick bars along the vertical axes indicate levels for which regression coefficients are statistically significant at 95% confidence
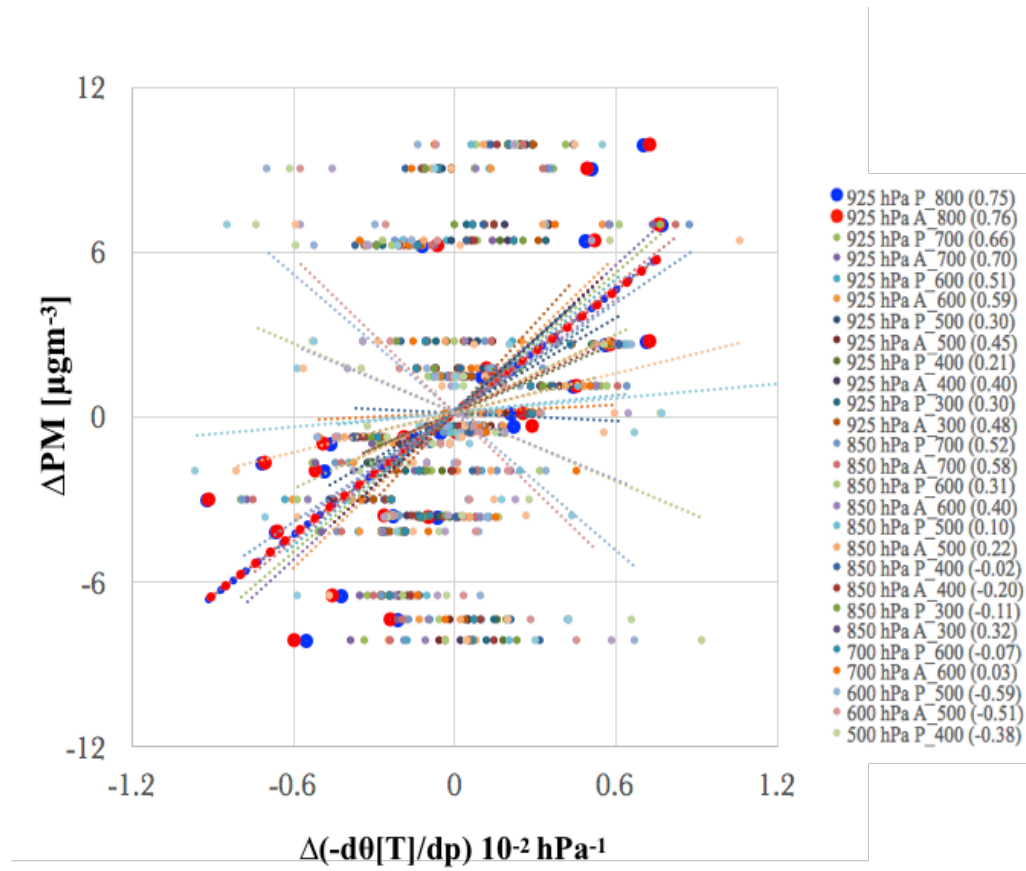
**Figure 2-4** Scatter plot of changes in PM (MERRAero) and lapse rate (ERA-I) at different pressure levels for Nov and Dec months, from 2002 to 2013. Both potential and actual temperature were used, denoted by P and A on the legend respectively. The long-term trend in each dataset was removed. In parentheses are the correlation coefficients (R), between PM and each lapse rate proxy. The dotted lines in corresponding colors are the least squares best fit to each set, with the optimal level (925 -800 hPa) emboldened.
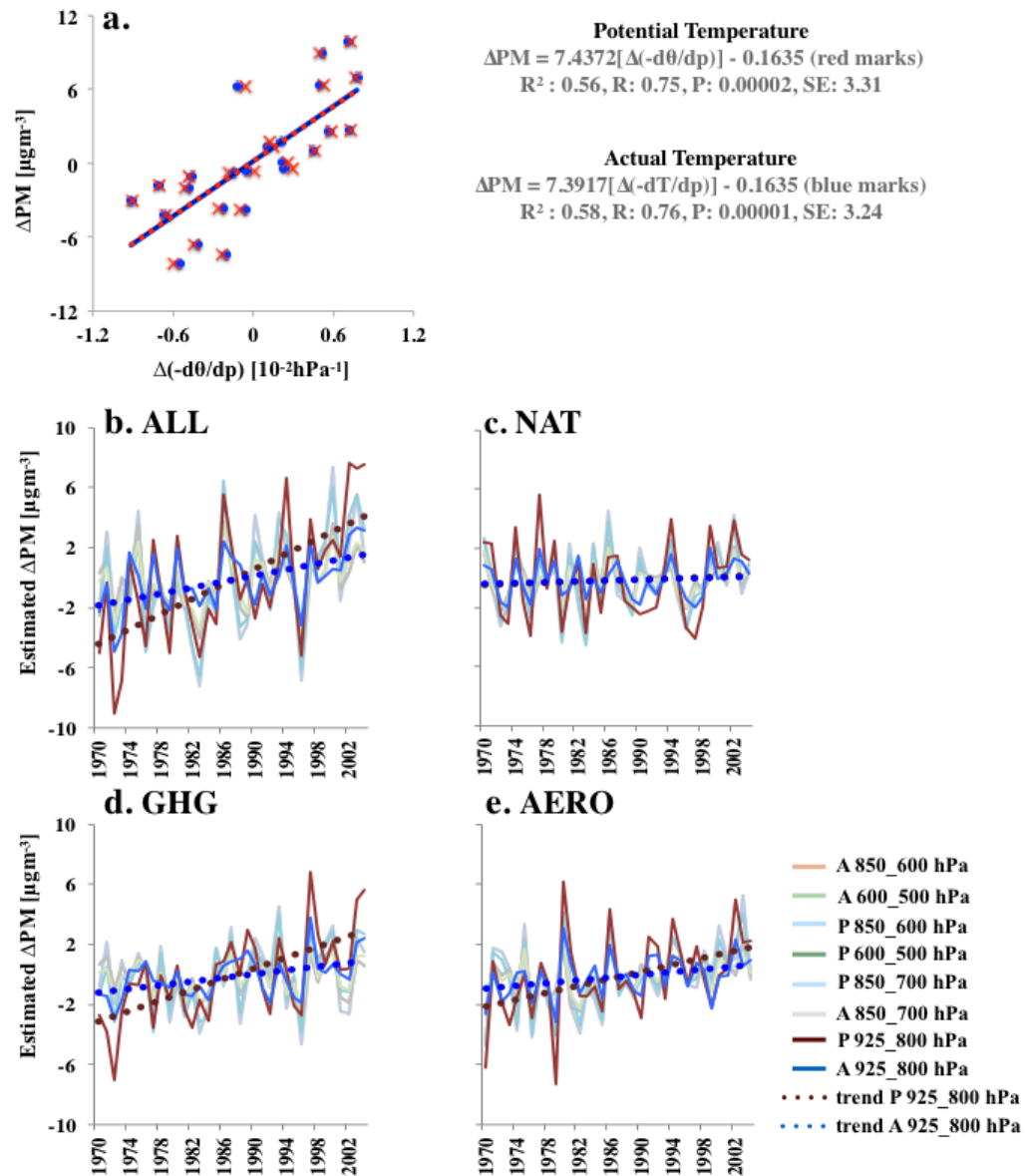
**Figure 2-5 a)** Scatter plot of PM (MERRAero) and lapse rate (ERA-I) for Nov and Dec months, with the linear least squares best fit to the data. Each lapse rate proxy is an average between two pressure levels as shown on the legend. The regression equation, correlation coefficient(R), coefficient of determination ($R^2$) and the standard error (SE) are shown on the plot. **b-e)** CMIP5 (composite of 11 models, Table 1) estimates of PM with different forcing data, based on the regression equation in (**a).** The optimal level is 925-800 hPa - shown in red for potential temperature and blue for actual temperature, overlaid with their respective linear trends in the same colors.
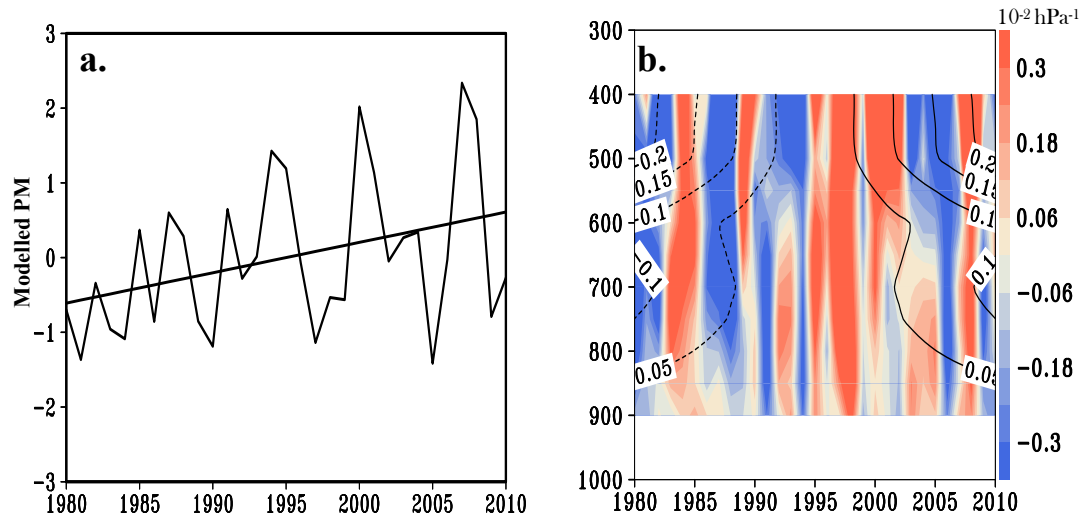
**Figure 2-6 a)** WRF-Chem simulations: **a)** Domain averaged surface mass concentration of PM (normalized), from 1980-2010. **b)** Mean Nov-Dec lapse rate anomalies ($\Delta[-d\theta/dp]$) (shading) relative to the 1980-2010 base period. Liner trends in $\Delta[-d\theta/dp]$ are displayed here as black contours. The experimental setup, physical and chemical schemes used for the simulations are shown in Table 2
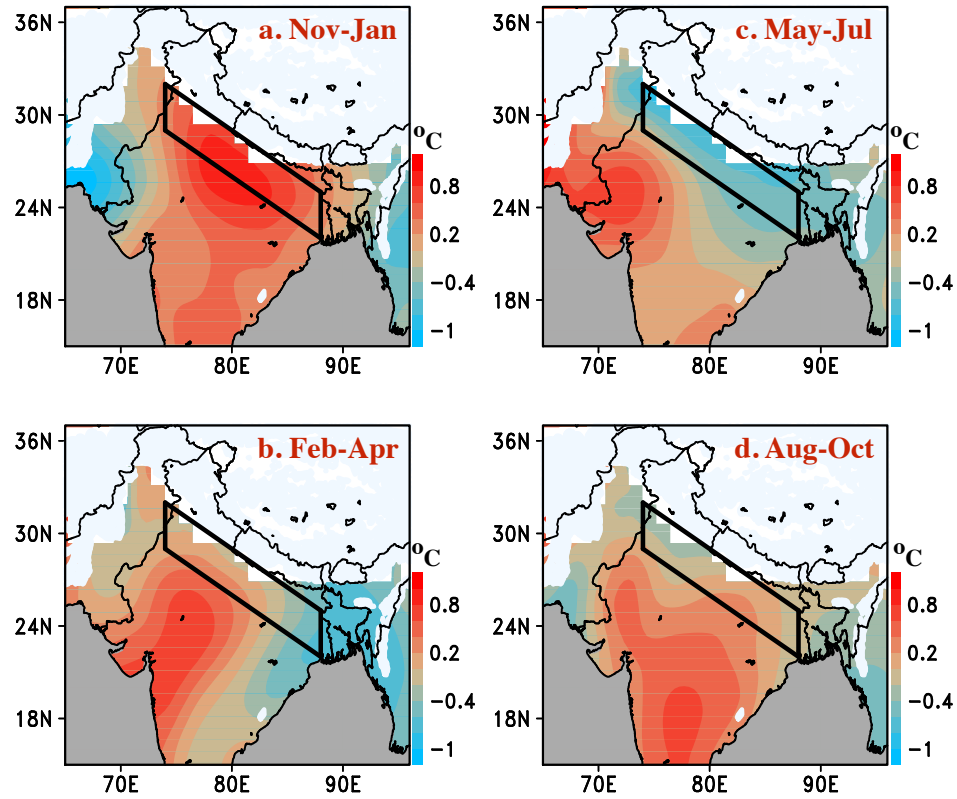
**Figure 2-7 a)** Seasonal potential temperature (MERRA) slope at the 800 hPa level (1980-2013). The Tibetan plateau and altitudes above1000 m have been masked out. Units have been converted to per 34-years.
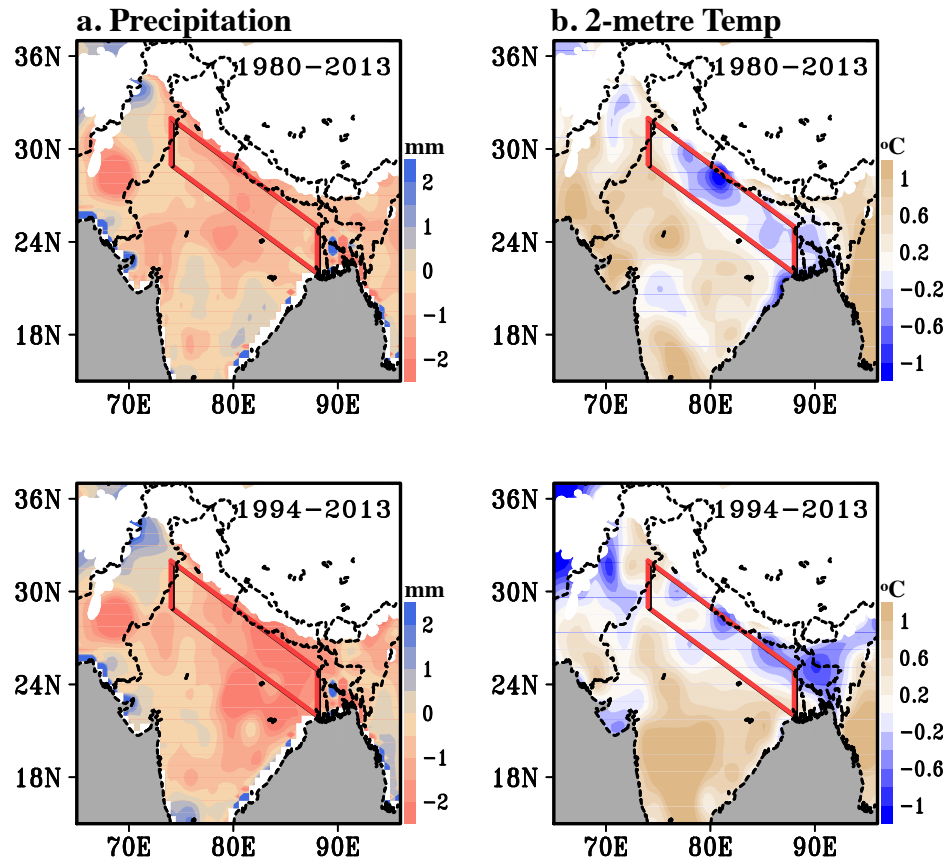
**Figure 2-8** Slope of precipitation (UDEL) and 2-metres temperature (ERA-I), for different time periods. The Tibetan plateau and altitudes above 1500 m have been masked out. Units have been converted to per 34-years (1980-2013) and per 20-years (1994-2013).

**Table 2-1** CMIP5 specifics as used in the study. The CMIP5 models we used that utilize interactive aerosol and prognostic cloud microphysics are emboldened.

| Acronym | Full name of Model | Centre/Institute | Resolution (lon. lat.) | Ensemble Size (max) |
|---|---|---|---|---|
| **CanESM2** | **Canadian Earth System Model, version 2** | **Canadian Center for Climate Modeling and Analysis, Canada** | **2.8° x 2.8°** | **5** |
| CCSM4 | Community Climate System Model, version 4 | National Center for Atmospheric Research, USA | 1.25°x1.0° | 5 |
| **CESM1-CAM5** | **Community Earth System Model, version 1, with Community Atmospheric Model, version 5** | **National Science Foundation (NSF)–Department of Energy (DOE)–NCAR, USA** | **1.25°x1.0°** | **2** |
| CNRM-CM5 | Centre National de Recherches Météorologiques Coupled Global Climate Model, version 5 | National Centre for Meteorological Research, France | 1.4° x 1.4° | 5 |
| **FGOALS_g2** | **Flexible Global Ocean-atmosphere-Land System Model, grid point version 2** | **LASG, Institute of Atmospheric Physics, Chinese Academy of Sciences, China** | **2.8° x 1.6°** | **4** |
| **GFDL-CM3** | **Geophysical Fluid Dynamics Laboratory Climate Model version 3** | **NOAA Geophysical Fluid Dynamics Laboratory, USA** | **2.5° x 2.0°** | **5** |
| GFDL-ESM2 | Canadian Earth System Model, version 2 Canadian Center for Climate Modeling and Analysis, Canada | NOAA Geophysical Fluid Dynamics Laboratory, USA | 2.5° x 2.0° | 3 |
| GISS-E2-H | Goddard Institute for Space Studies Atmospheric Model E, version 2, coupled with the Hybrid Coordinate Ocean Model (HyCOM) | NASA Goddard Institute for Space Studies, USA | 2.5° x 2.0° | 5 |
| GISS-E2-R | Goddard Institute for Space Studies Atmospheric Model E, version 2, coupled with the Hybrid Coordinate | NASA Goddard Institute for Space Studies, USA | 2.5° x 2.0° | 5 |
| IPSL-CM5A-MR | L'Institute Pierre-Simon Laplace Coupled Model, version 5A, medium resolution Institute Pierre-Simon Laplace, France | Institute Pierre-Simon Laplace, France | 2.5° x 1.25° | 2 |
| **NorESMI-M** | **Norwegian Earth System Model, version 1, intermediate resolution** | **Norwegian Climate Center, Norway** | **2.5° x 1.9°** | **3** |

**Table 2-2** Experimental setup, major physical and chemical schemes used for the WRFChem simulations of PM

| Scheme | Reference |
|---|---|
| Short wave radiation scheme | Goddard [Chou and Suarez 1999] |
| Long wave radiation scheme | RRTM [Mlawer et al. 1997] |
| Cumulus scheme | Grell 3D ensemble scheme |
| Microphysics scheme | Lin scheme [Lin et al. 1983] |
| Planetary boundary layer scheme | YSU scheme [Hong et al. 2006] |
| Land surface model | Noah [Chen et al. 1996] |
| Aerosol chemistry | RADM2 Chemistry[Chang, 1989] &GOCART aerosols [Chin et al. 2002] |
| Biogenic emissions | Gunther scheme [Guenther et al. 1993] |

**Experimental Setup**
The experiment was forced by initial condition and lateral boundary condition derived from the ECMWF Interim Reanalysis (Dee et al. 2011) and emission rates created from PREP-CHEM-SRC 1.5 (Freitas et al. 2011). Anthropogenic aerosol emissions were set constant (year 2000 levels) from January 1979 to December 2010. The simulation was conducted within 15$^o$S - 45$^o$N and 55$^o$E - 129$^o$N, with a grid resolution of 100 km.

CHAPTER 3

THE 2014/15 SNOWPACK DROUGHT IN WASHINGTON STATE AND ITS

CLIMATE FORCING[2]

ABSTRACT

In what has since been nicknamed the "snowpack drought" of 2015, the 2014/15 cold season drought in Washington State and much of the Pacific Northwest (PNW) resulted from exceedingly high temperatures notwithstanding normal precipitation statewide, which caused cold season precipitation to fall as snow rather than rain in the Mountains. The authors show that a significant portion of the circulation anomalies associated with the 2014/15 snowpack drought can be explained by North Pacific climate variability in the form of the North Pacific Index (NPI) with a modulation from the North Pacific Oscillation. It is also found that there exists a unique cyclical relationship between temperature and precipitation along the Cascades, that is predominantly driven by the 15-years low frequency variability of the NPI. This is a finding that can be utilized as a supplemental tool for projecting future snowpack droughts and goes further to show that perturbations in the natural climate state can drive years of extreme warmth and drought even when precipitation is normal. Furthermore, a spectral coherence amplitude analyses involving the 15-years lowpass NPI and the 15-years sliding correlation between cold season precipitation and temperature (i.e. P-T SCORR) along the cascades was carried out

using data from the thirty-member Community Earth System Model version 1 (CESM1) large ensemble project. The results did not project significant changes in the peak amplitudes of the cross-spectra, suggesting that both P-T SCORR and the NPI modulation are natural variability that are not projected to change under warming.

## 1. Introduction

The State of Washington declared a drought emergency in May 2015 following a drastic decline in snowpack over the adjoining Cascades (Figure 1a). Unlike past droughts that were mainly caused by precipitation deficits (e.g. the 2005 drought – Anderson et al., 2005), the 2014/15 cold season (Nov-Mar) produced near-normal precipitation statewide (Figure 1b). In what has since been nicknamed the "snowpack drought" of 2015 (http://www.ecy.wa.gov/drought/), the drought was more a result of unprecedented warmth (Figure 1c) that caused cold-season precipitation to fall as rain rather than snow on the mountains. A small change in temperature can alter the water balance by reducing the precipitation falling as snow, which results in declined snow water equivalent and summer streamflow (Mote 2006, Stewart et al. 2004). This 2014/15 situation thereby sets an example for the known effect of atmospheric warming on reducing mountain snowpack in the Pacific Northwest (PNW), a known risk that has been reported by a sizable body of research (e.g., Stoelinga et al. 2010, Mote et al. 2014, Abatzoglou et al. 2014).

Reduction in the PNW snowpack also increases the risk of wildfires, the latter of which is evidenced by the remarkable 2015 wildfire season, the largest in the states' history. Since snowpack is the major source of water storage in much of the Western United States, a substantial reduction in any cold season would have serious ramifications on farming and

water resources in the following spring and summer. A Washington Department of Agriculture report (http://agr.wa.gov/FP/Pubs/docs/) estimates the 2015 drought alone has caused more than $335 million in losses to the State's agricultural industry. In this study, we investigate the role natural climate variability played in the 2015 Washington State drought and situate it in the context of anthropogenic climate change.

## 2. Datasets and Methodology

The observed mean surface air temperatures (T) and precipitation (P) were obtained from monthly records of PRISM's High Resolution Spatial Climate Data (https://climatedataguide.ucar.edu). For the analysis of Northern Pacific climate variability, NOAA's Extended Reconstructed Sea Surface Temperature (SST) v4 was used (Huang et al. 2015). Circulation patterns were based on streamfunction ($\Psi$) derived from the NCEP/NCAR global wind reanalysis (Kalnay et al. 1996). NCEPS's daily two-meter ($T_{2m}$) air temperature dataset (Kristler et al, 2001) and CPC's Unified Gauge-Based Analysis of Daily Precipitation were used for the estimation of snow-precipitation ratio (S/P) and snow frequency (SF); the latter was also used to characterize dry spells following Gillies et al. (2012). Precipitation was fully classified as snow at $T_{2m} \leq 0$ °C. Since most Washington's snowpack is stored in the Cascades, we focused on the cold season of November-March over the mountain ranges outlined in Figure 1a; i.e. all-time series were area-averaged from the domain referred to as the Cascades.

Historical and future simulations with the Community Earth System Model version 1 (CESM1) (Hurrell et al. 2014) were analyzed to examine external climate forcing to drought variability in the region and to project possible long-term changes. Thirty ensemble

members produced by CESM1 with a spatial resolution of $0.9^{\circ}$ longitude $\times$ $1.25^{\circ}$ latitude through the Large Ensemble Project (Kay et al. 2014) were used. The simulations cover two periods: (1) 1920–2005 with historical forcing, including greenhouse gases, aerosols, ozone, land use change, solar and volcanic activity, and (2) 2006–2080 with RCP8.5 forcing that represents a high-emission pathway (Taylor et al. 2012). The ensemble spread of initial conditions is generated by the commonly used 'round-off differences' method (Kay et al. 2014).

## 3. Result and Discussion

The simultaneous correlation between precipitation (P, Figure 1b) and temperature (T, Figure 1c) along the Cascades (Figure 1a) in the past century has been weak ($r < 0.1$); however, the coherency between P and T appears to fluctuate over time. To examine the unique combination of near-normal precipitation (P) and high temperatures (T) experienced in the 2014/15 cold season, we computed the sliding correlation between observed P and T over the domain along the Cascades shown in Figure. 1a. Figure 1d shows the sliding correlation (SCORR) between P and T within various windows ranging from 7 to 21 years, revealing a cyclical pattern in the coherency of P with T on inter-decadal timescales. The correlation between P and T was mostly positive during the first third of the century, after which negative correlations prevailed until the late 1970's, then the correlation pattern reversed back to positive. Even though the correlation coefficients are only marginally significant at the peaks and troughs (for the 15-year window the significant SCORR at the 95% interval is .48), the SCORR pattern bears a visual similarity to the low frequency variations within the North Pacific, expressed by the North Pacific Index (Figure

1e). Calculated from the area-weighted sea level pressure over the region 30°N-65°N, 160°E-140°W, the NPI measures the intensity changes of the Aleutian low, which affects cyclone frequency and passages over the PNW (Trenberth and Hurrell, 1994). The SCORR pattern mimics the timing of major shifts in the sign of the NPI; a negative regime from 1947-1976, with positives dominating from 1925-1946 and from 1977 through the present. Since the NPI and the Pacific Decadal Oscillation (PDO) are significantly correlated, the PDO has a similar inter-decadal coherence with P and T. Here, we focus on the NPI since the PDO is deemed an oceanic response to integrated atmospheric forcing (Newman et al. 2016) and strictly speaking, should not be directly regarded as a climate driver of the PNW. In Table 1, we list an array of climate indices and their correlation coefficient with the P-T SCORR using the 15-year window, and both the NPI and PDO stand out as being significant at $p<0.01$.

Next, the weather processes that encompass the NPI regimes and dry spells in the Cascades are examined. An extreme dry spell was defined as a prolonged period of at least 10 days without substantial precipitation accumulation (< 5 mm). As shown in Figure 1e, more and prolonged dry spells (red dots) tend to occur in the positive NPI regime during which temperature and precipitation tend to be positively correlated. In the opposing phase, less intense dry spells are observed, with negative correlations between temperature and precipitation. A third scenario exists, whereupon a correlation of near zero exist between P and T. The 2014/15 event falls under such zero-correlation regime, and is evidence that natural climate variability can drive years of extreme warmth and drought even when precipitation is normal.

To understand the circulation and SST patterns associated with wet and dry spells along the Cascades, Figure 2a shows the 250 mb streamfunction and SST differences between low and high snow frequency years. Low snow years are associated with a SST pattern that is analogous to the positive phase of the PDO (or the Interdecadal Pacific Oscillation that has a stronger tropical signal), with a warm tongue of water situated off the coast of California accompanied by an anomalous ridge over the PNW. The 2014/15 circulation anomalies (Figure 2b) produced a similar yet amplified pattern including the high pressure over the West Coast and a low pressure over northeastern North America. This pair of circulations echo the dipole pattern associated with the 2013/14 California drought (Wang et al. 2014, 2015; Funk et al. 2015) that occurred again in 2015. The circulation anomalies associated with the NPI (Figure 2c) resembles the low-snow frequency situation, as was previous documented (e.g., Mote 2006). By comparison, the 2014/15 circulation also bears resemblance to the pattern of North Pacific Oscillation (NPO; Rogers 1981) (Figure 2d), with a similar (yet shifted) high-pressure ridge over the western U.S. and warm SST anomalies in the northeastern Pacific. However, the 2014/15 SST anomalies feature a much warmer water around the PNW coast, referred to as a "blob" of warmer water consolidated into the PDO's region of ocean fluctuation that was strengthened by the stagnation of high pressure in the Gulf of Alaska (Bond et al. 2015).

To analyze further the collective effects of NPI and NPO on the 2014/15 circulation anomalies, we computed the regression coefficients of streamfunction and SST anomalies with the NPI and NPO from 1949/50 to 2013/14, and weighted the coefficients against the observed values of the 2014/15 season; this led to a statistical estimate of the anomalies that are individually attributable to each mode. Then, a linear "attribution" analysis was

carried out by removing the combined regressed patterns of the NPI and NPO from the 2014/15 anomalies (here, the NPO signal was "regressed out" from the NPI). The residual (Figure 2e) shows a weak swath of warmer SST across the North Pacific with some patches of cool waters, suggesting that the key SST feature in the 2014/15 situation near the PNW has been considerably reduced. The drought-inducing ridge engulfing the West Coast (Figure 2b) was also reduced by more than one half with a displaced center. The residual SST could be explained by possible warming effects of anthropogenic greenhouse gases, as was argued by Weller et al. (2015). Since the Cascades' surface air temperature is significantly correlated with the offshore SST (Figure 3), these results hint a collective effect from anthropogenic warming and combined NPI-NPO modulation on the 2014/15 anomaly that led to low snowfall.

The limited length of observational data poses a challenge in verifying the inferred NPI modulation on the fluctuating P-T relationship (i.e. P-T SCORR). Thus, to ascertain possible changes in this NPI and the P-T SCORR relationship in future, we performed the same analysis as in the observations using data from the CESM1's 30-member ensemble. The CESM1's 30-member ensemble appears to capture the NPI in both the historical and future runs (using the same definition as in the observation), without any noticeable trend in the RCP8.5 runs (Figure 4a). Likewise, the model does not suggest any perceptible future deviation from the SCORR pattern between P and T (Figure 4b) either. This result suggests that the P-T SCORR and the NPI modulation is a naturally driven variability that is not projected to change. More to this, the spectral coherence between the observed NPI (15-years low pass) and the 15-years SCORR between P and T was computed. To address uncertainty in the coherence at low frequencies/long periods, we computed the spectral

coherence for two periods: 101 (Figure 5a) and 59 (Figure 5b) years. The spectral coherency reveals dominant periodicities at 30-50 years, which is consistent with the NPI's periodicity. Here the low frequency band should be interpreted with caution owing to the limited data length. Nonetheless, both the historical (Figure 5c) and future (Figure 5d) simulations of the CESM1 reproduced this 30-50-year spectral peak of the coherency. This performance is in line with the CESM1's noted ability in reproducing the broad North Pacific SST variability (Yoon et al. 2015) and the supposed stationarity of the NPI (Figure 4a). Under the future scenario (RCP 8.5), the model projects an amplified spectral coherency of SCORR with NPI while the frequency remains unchanged. However, the increase in spectral coherency only marginally passes the red noise spectrum and therefore does not suggest confidently that global warming would change the correspondence between the P-T regime and the NPI.

Despite these results, anthropogenic warming continues to pose a threat to the Cascades snowpack as shown in Figure 6a. The post-1970 increase in observed T coincides with the rising trend of simulated T and these correspond to the expected decreasing trend in the projected S/P (Figure 6b). However, the accelerated increase in observed temperature and the record warmth in 2014/15 could be an early indication that, even though precipitation in the PNW does not change in the future, the persistent warming will increase the likelihood of a normal P and high T situation like 2014/15 or worse, a high T and low P scenario as suggested in the negative SCORR regime of Figure 1d. In terms of risk assessment, these results suggest that any superimposition of a high temperature with low precipitation would exacerbate drought, making it potentially more severe than the 2014/15

situation with normal precipitation. The CESM1 projections lend support to such a possibility in the future.

## 4. Summary

In the winter of 2014/15, the average temperature along the Cascades was the highest on record and occurred in tandem with the emergence of extremely positive SST anomalies that developed off the coast of the PNW. The high-pressure ridge increased the PNW temperatures to a record level while reducing the snow frequency. Diagnostic analysis presented here suggests that a significant portion of the circulation patterns associated with the 2014/15 snowpack drought can be explained by the North Pacific climate variability in the form of the NPI with a modulation from the NPO. Even though the effect of North Pacific climate variability on the PNW is well known (Stoelinga et al. 2010, Mote et al. 2014, Abatzoglou et al. 2014), this study uncovered a unique cyclical relationship between temperature and precipitation that is apparently driven by the low frequency variability of the NPI. This process is especially concerning considering recent findings that despite little long-term trend in average West Coast precipitation, precipitation may be falling in more concentrated bursts (Prein et al. 2016) due to changes in certain circulation patterns (Swain et al. 2016; Lehmann and Coumou 2015). Under the warming climate, increasing air temperature embedded in stagnated ridge systems off the West Coast (Diffenbaugh et al. 2015) can reduce snowpack even without an apparent precipitation deficit – a situation that was realized in the 2014/15 snowpack drought of Washington.

**References**

Abatzoglou, J. T., D. E. Rupp, and P. W. Mote, 2014: Seasonal Climate Variability and Change in the Pacific Northwest of the United States. J. Climate, 27, 2125–2142, doi: 10.1175/JCLI-D-13-00218.1.

Anderson, B., and Coauthors, 2006: 2005 Drought Response Report to the Legislature. Washington Department of Ecology and Water Resources Program. Publication No. 06-11-001, 55 pp.

Bond, N. A., M. F. Cronin, H. Freeland, and N. Mantua, 2015: Causes and impacts of the 2014 warm anomaly in the NE Pacific. Geophys. Res. Lett., 42, 3414–3420. doi: 10.1002/2015GL063306.

Diffenbaugh, N. S., D. L. Swain, and D. Touma, 2015: Anthropogenic warming has increased drought risk in California. Proceedings of the National Academy of Sciences of the United States of America, 112(13), 3931–3936. http://doi.org/10.1073/pnas.142238511.

Funk, C., S. Shukla, A. Hoell, and B. Livneh, 2015: Assessing the contributions of East African and west Pacific warming to the 2014 boreal spring East African drought. Bull. Amer. Meteor. Soc. 96 (12), S77–S81.

Gillies, R. R., S.-Y. Wang, and M. R. Booth, 2012: Observational and synoptic analyses of the winter precipitation regime change over Utah. Journal of Climate, 25, 4679-4698, doi:10.1175/JCLI-D-11-00084.1.

Huang, B., and Coauthors, 2015: Extended reconstructed sea surface temperature version 4 (ERSST.v4). Part I: Upgrades and intercomparisons. J. Clim., **28**, 911–930, doi:10.1175/JCLI-D-14-00006.1.

Hurrell, J. W. and Coauthors, 2013. The Community Earth System Model: a framework for collaborative research. Bull. Am. Meteorol. Soc. **94**, 1339–1360, doi:10.1175/BAMS-D-12-00121.1.

Kalnay, E., and Coauthors,1996: The NMC/NCAR 40-Year Reanalysis Project. Bull. Am. Meteorol. Soc., **77**, 437–471.

Kay, J. E., and Coauthors, 2015: The community earth system model (CESM) large ensemble project : A community resource for studying climate change in the presence of internal climate variability. Bull. Am. Meteorol. Soc., **96**, 1333–1349, doi:10.1175/BAMS-D-13-00255.1.

Kistler, R., and Coauthors, 2001: The NCEP-NCAR 50-year reanalysis: Monthly means CD-ROM and documentation. Bull. Am. Meteorol. Soc., **82**, 247–267.

Lehmann, J., and D. Coumou, 2015: The influence of mid-latitude storm tracks on hot, cold, dry and wet extremes, Sci. Rep. 5, 17491, doi:10.1038/srep17491.

Mote, P. W., 2006: Climate-driven variability and trends in Mountain Snowpack in Western North America. J. Clim., **19**, 6209–6220, doi:10.1175/JCLI3971.1.

Mote, P., A. K. Snover, S. Capalbo, S. D. Eigenbrode, P. Glick, J. Littell, R. Raymondi, and S. Reeder, 2014: Ch. 21: Northwest. Climate Change Impacts in the United States:

The Third National Climate Assessment, J. M. Melillo, Terese (T.C.) Richmond, and G. W. Yohe, Eds., U.S. Global Change Research Program, 487-513. doi:10.7930/J04Q7RWX.

Newman, M. and Coauthors, 2016: The Pacific Decadal Oscillation, Revisited. J. Climate, 29, 4399–4427, doi: 10.1175/JCLI-D-15-0508.1.

Prein, A. F., G. J. Holland, R. M. Rasmussen, M. P. Clark, and M. R. Tye, 2016: Running dry: The U.S. Southwest's drift into a drier climate state, Geophys. Res. Lett., 43, 1272-1279, doi:10.1002/2015GL066727.

Rogers, J. C., 1981: The north Pacific oscillation. Journal of Climatology,1(1), 39-57.

Stewart, I. T., D. R. Cayan, and M. D. Dettinger, 2004: Changes in snowmelt runoff timing in western North America under a business as usual' climate change scenario. Clim. Chang., **62**, 217–232, doi:10.1023/B:CLIM.0000013702.22656.e8.

Stoelinga, M. T., M. D. Albright, and C. F. Mass, 2010: A New Look at Snowpack Trends in the Cascade Mountains. J. Climate, **23**, 2473–2491, doi: 10.1175/2009JCLI2911.1.

Swain, D. L., D. E. Horton, D. Singh, and N. S. Diffenbaugh, 2016: Trends in atmospheric patterns conducive to seasonal precipitation and temperature extremes in California, Science Advances, 2, e1501344.

Taylor, K. E., R. J. Stouffer, and G. A. Meehl, 2012: An overview of CMIP5 and the experiment design. Bull. Am. Meteorol. Soc., **93**, 485–498, doi:10.1175/BAMS-D-11-00094.1.

Trenberth, K. E., and J. W. Hurrell, 1994: Decadal atmosphere-ocean variations in the Pacific. Clim. Dyn., **9**, 303–319, doi:10.1007/BF00204745.

Wang, S. Y., L. Hipps, R. R. Gillies, and J. H. Yoon, 2014: Probable causes of the abnormal ridge accompanying the 2013-2014 California drought: ENSO precursor and anthropogenic warming footprint. Geophys. Res. Lett., **41**, 3220–3226, doi:10.1002/2014GL059748.

Wang, S. Y. S., W. R. Huang, and J. H. Yoon, 2015: The North American winter "dipole" and extremes activity: A CMIP5 assessment. Atmos. Sci. Lett., **345**, 338–345, doi:10.1002/asl2.565.

Weller, E., S.-K Min, D. Lee, W. Cai, S.-W. Yeh, and J.-S. Kug, 2015: Human contribution to the 2014 record high sea surface temperatures over the western tropical and northeast Pacific Ocean [in ''Explaining Extremes of 2014 from a Climate Perspective'']. Bull. Am. Meteorol. Soc. 96(12), S100–S104. doi:10.1175/ BAMS-D-15-00055.1.

Yoon, J.-H., S.-Y. Wang, R. R. Gillies, B. Kravitz, L. Hipps, and P. Rasch, 2015: Increasing Water Cycle Extremes in California and in Relation to ENSO Cycle Under Global Warming. Nature Communications, doi: 10.1038/ncomms9657.

**Figures**
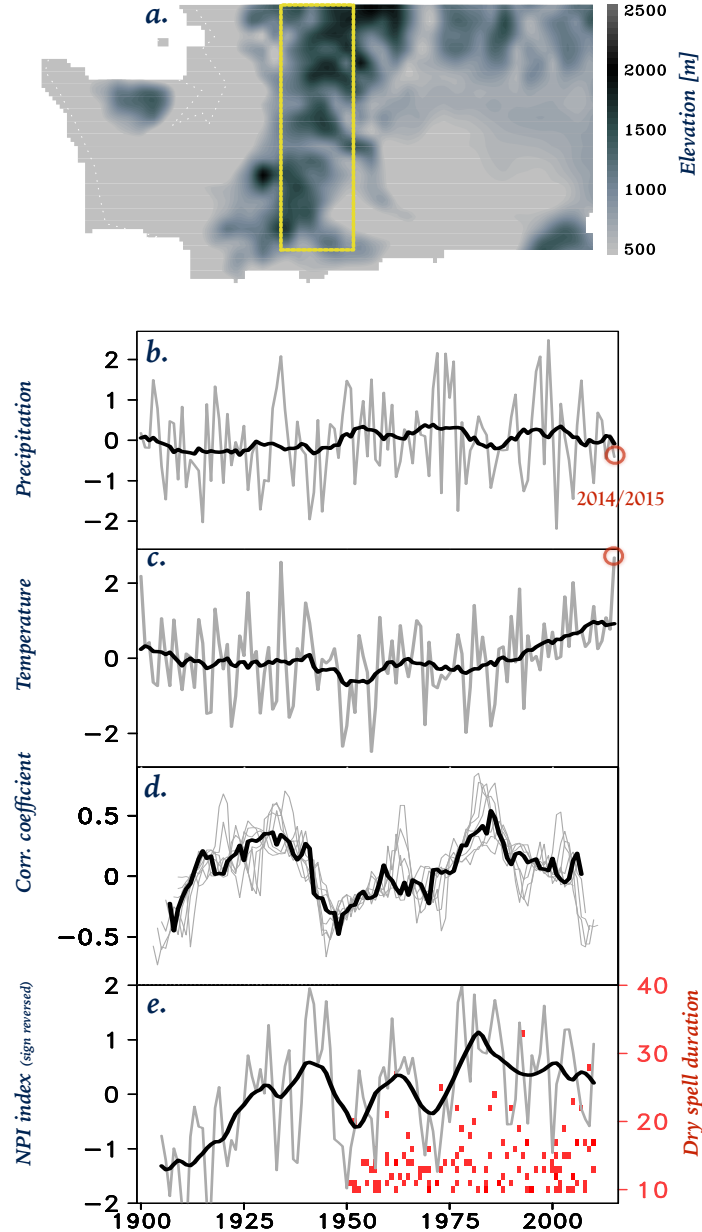


**Figure 3-1 a:** Topographical map of Washington - the yellow box delineates the study domain. **b-c:** Domain averaged time series of normalized cold season precipitation and temperature, both in gray, and their respective 15 years lowpass curves in black. **d:** 15-years sliding correlation between P and T, in black. The gray lines show the sliding correlation curves for different windows ranging from 7 to 21-years in 2 years' increments. Years on the x-axis represent the central year of the sliding window. **e:** 15 years running mean (black) of the NP index (gray), constructed from the area-weighted sea level pressure over the region 30°N-65°N, 160°E-140°W. The NPI sign has been flipped so that positive refers to a deepening of the Aleutian low, which also will correspond to positive PDO phase. The red dots are intense dry spells, and their duration [days].
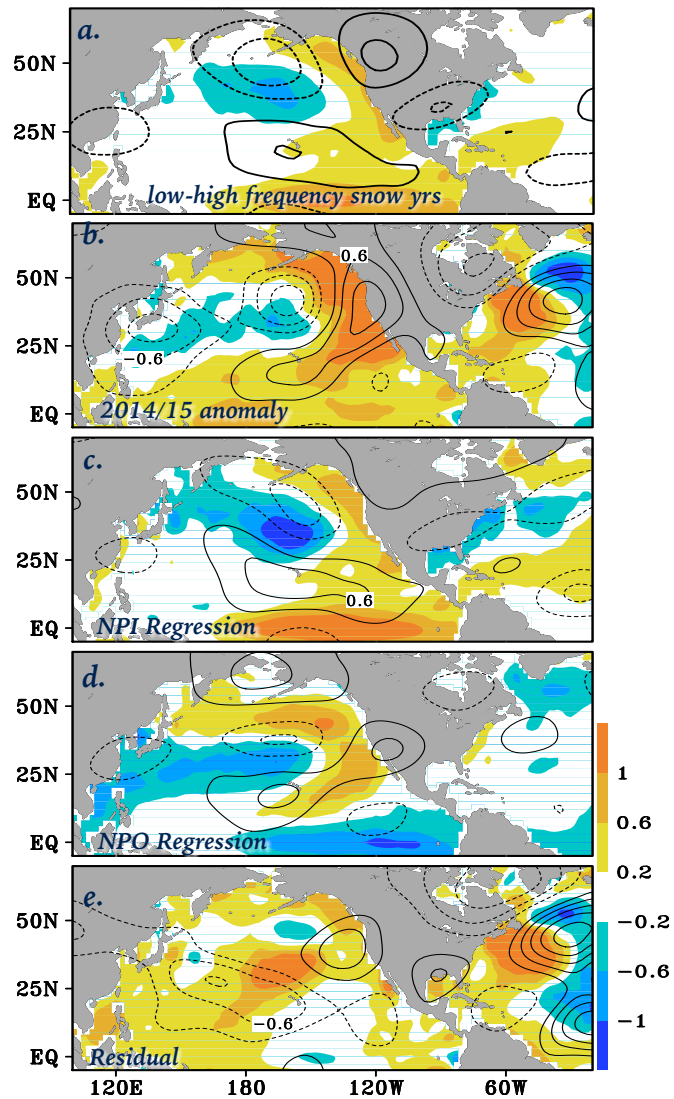
**Figure 3-2 a:** Composite differences in cold season circulation [250 mb $\psi$ in contours, interval: 0.3 106m2s-1] and SST (shading) between 31 low and 31 high snow frequency years selected between 1950 and 2014. **b:** The observed SST and 250mb streamfunction anomalies for 2014/15 cold season. **c:** A linearly regressed reconstruction of SST and 250mb streamfunction anomalies related to the NPI, from the 1949/50 cold season to 2013/14, weighed against the strength of the NPI in the 2014/15 season NPI. **d:** Same as (c) but for the NPO **e:** Difference between (b) and (c), (i) (i.e. the leftover not linearly explained by the NPI).
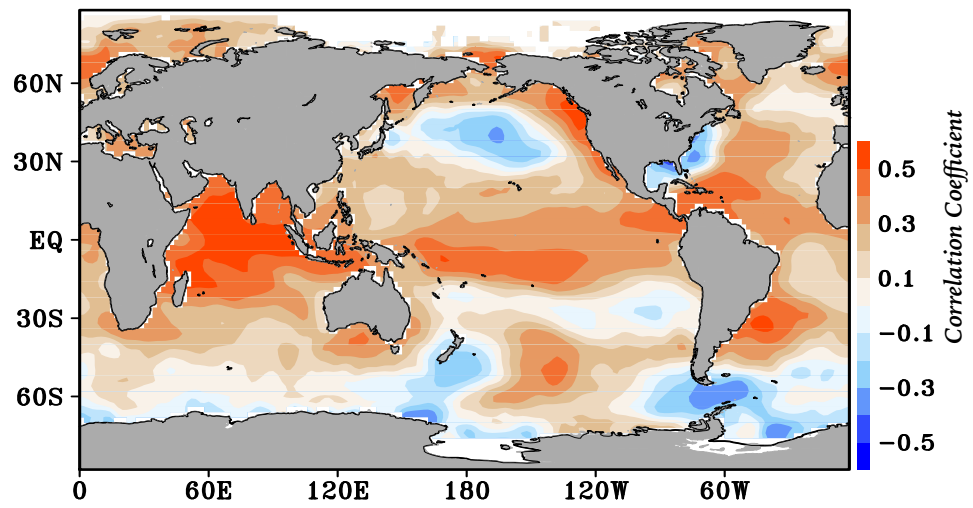
**Figure 3-3** Correlation between Cascades temperature and global SST
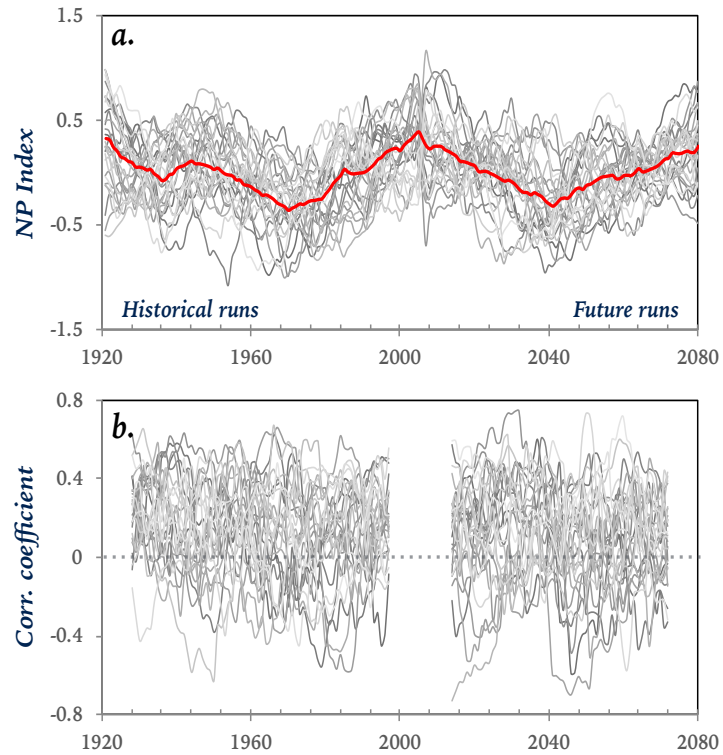
**Figure 3-4 a:** The 15-years running mean of the NPI, constructed as the area-weighted sea level pressure over the region 30°N-65°N, 160°E-140°W for 30 CESM1 ensemble members (in gray), and their ensemble mean (in red), for both historical and future RCP8.5 runs; adjoined. **b:** 15 years sliding correlation between temperature and precipitation. Years on the x-axis represent the central year of the 15 years sliding window.
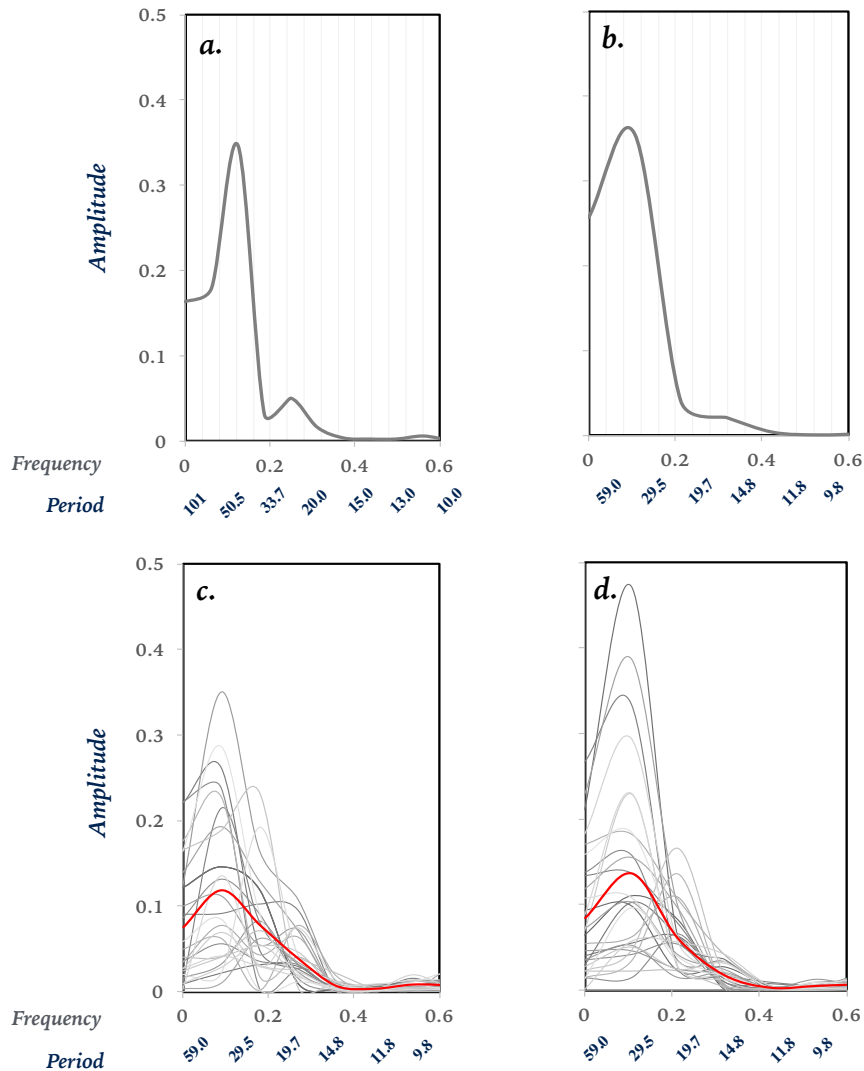
**Figure 3-5 a:** Spectral coherence amplitude between the NPI and the 15-years sliding correlation of observed cold season precipitation and temperature from 1908-2008. **b:** same as (a) but from 1928-1986. **c-d:** Same as (b) but for CESM1 derived historical (1928-1997) and future (2014-2072) PDO and SCORR outputs. The minimum number of time steps that could be used was 59 years because of the limited extent of CESM1's future run. As a result, only a comparable number of years in observations could be used to allow for easy comparisons. Similarly, red curves represent the ensemble mean here.
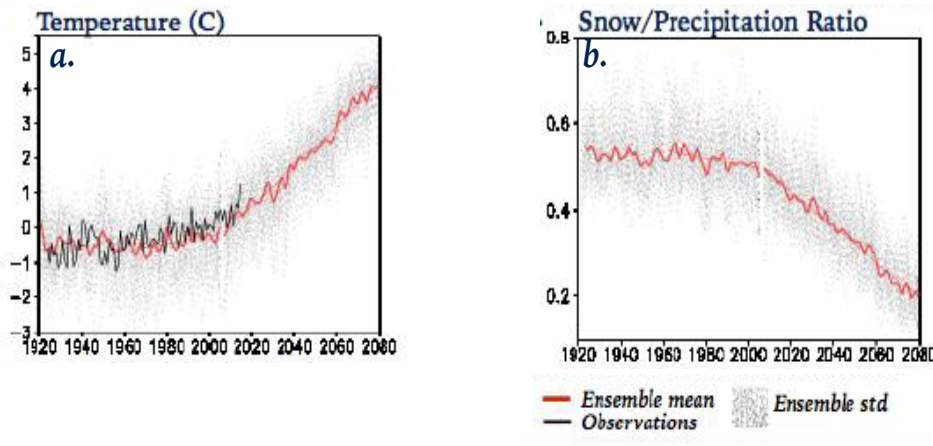
**Figure 3-6 a:** CESM1 LENS temperature - 5 years running mean applied to the ensemble average (in red) for 30 ensemble members relative to the 1950-2005 base period, for both historical (1920-2005) and future RCP8.5 (2006-2080) runs. The two epochs have been adjoined. Gray shading represents the standard deviation (std) range of the individual ensemble values corresponding to each time step relative to the mean. Trend lines for corresponding epochs are superimposed in red. Observed temperature is superimposed in black. **b:** Same as (a) but for snow to precipitation ratio (S/P) estimated from monthly data of precipitation and temperature

**Table 3-1** Climate indices correlation with SCORR. Indices obtained from (http://www.esrl.noaa.gov/psd/data/climateindices/list/)

| Climate Index | Acronym | Sliding Correlation |
|---|---|---|
| Artic Oscillation | AO | 0.181 |
| Atlantic Multidecadal Oscillation | AMO | -0.473 |
| Central Pacific Teleconnection Index | CP | 0.199 |
| Central Tropical Pacific SST | Nino4 | 0.125 |
| East Atlantic Teleconnection Index | EA | 0.347 |
| East Pacific Teleconnection Index | EP | 0.013 |
| Eastern Tropical Pacific SST | Nino3 | 0.138 |
| East Central Tropical Pacific SST | Nino3+4 | 0.101 |
| Extreme Eastern Tropical Pacific SST | Nino1+2 | 0.128 |
| North Atlantic Oscillation | NAO | 0.405 |
| North Pacific Oscillation | NPO | 0.119 |
| North Pacific Index | NPI | -0.512 |
| Pacific North American Index | PNA | 0.351 |
| Pacific Meridional Mode SST | PMM | 0.139 |
| Pacific Decadal Oscillation | PDO | 0.532 |
| Tropical/ Northern Hemisphere | TNH | 0.161 |
| Western Pacific Teleconnection Index | WP | 0.174 |

CHAPTER 4

SYNOPTIC AND CLIMATE ATTRIBUTIONS OF THE DECEMBER 2015

EXTREME FLOODING IN MISSOURI, USA[3]

ABSTRACT

Three days of extreme rainfall in late December 2015 in the middle of the Mississippi River led to severe flooding in Missouri. The meteorological context of this event was analyzed through synoptic diagnosis and forecast attribution into the atmospheric circulation that contributed to the precipitation event's severity. The midlatitude synoptic waves that induced the extreme precipitation and ensuing flooding were traced to the Madden Julian Oscillation (MJO), which amplified the trans-Pacific Rossby wave train likely associated with the strong El Niño of December 2015. Though the near historical El Niño contributed to a quasi-stationary trough over the western U.S. that induced the high precipitation event, a constructive interference between the MJO and El Niño teleconnections resulted in a relatively weak atmospheric signature of the El Niño in comparison to that of the MJO. The influence of anthropogenic climate change on the relationship between ENSO and precipitation across several central U.S. states was also using investigated using 17 CMIP5 models from the historical single-forcing experiments. A regime change in ENSO-related precipitation anomalies appears to have occurred, from being negatively correlated before 1950 to positive and significantly correlated after 1970, suggesting a likely effect of anthropogenic warming on the December 2015 extreme

precipitation event. In addition, a forecast attribution analysis was conducted on the MJO-associated circulation anomalies of the late December event using NCEP's Climate Forecast System (CFSv2). It was found that skillful subseasonal predictions of the MJO with lead times exceeding two weeks are rarely achievable.

## 1. Introduction

During late December 2015, a low-pressure system moved ashore onto the West Coast of the United States and later tracked northeastwards. This trough system induced a strong band of thunderstorms across the U.S. Central and Southern Plains, bringing unseasonably numerous tornadoes and unprecedented flooding (Figure 1a). The storm and its aftermath caused 50 fatalities and an estimated $3 billion damages in 13 U.S. states, with Missouri being the most impacted by flooding [1]. The meteorological causes of the flooding in Missouri are evident: First, antecedent soil moisture conditions were saturated (Figure 1b) due to a consistently wet year with record rainfall in November (Figure 1c). Statewide precipitation was 300% of normal, making it the second wettest December on record and the wettest since 1982 (Figure 1d). The soil conditions exacerbated the effect of the widespread rains received in December (not shown), before the late-December storm dropped about eight inches of precipitation. The atypical nature of the flooding is further highlighted by the time of year it occurred, since major precipitation and flooding events along the Mississippi River and Missouri have historically taken place in spring or summer (e.g. [2]).

The persistent synoptic patterns associated with the flooding (Figure 1a) seems to suggest a modulation effect from large-scale circulation anomalies. During December

2015, the El Niño Southern Oscillation (ENSO) was at a near record positive phase, and it is well known that ENSO and its teleconnection can modulate the frequency of wintertime extremes in the U.S. (e.gs [3,4]). Coincidentally, a mature Madden Julian Oscillation (MJO) episode developed in December and appears to have interfered constructively with the El Niño effect (Figure 2a). As the primary source of intraseasonal variability in the Earth's climate system [5], the MJO's modulation of tropical convection can initiate poleward propagating Rossby waves that impact extratropical weather patterns and, in turn, influence the leading modes of low-frequency northern hemisphere variability, particularly in the Boreal winter [6,7].

Against this backdrop, the purpose of this study is to evaluate the extent to which large-scale circulation patterns associated with the El Niño and MJO may have facilitated the late-December 2015 extreme precipitation in Missouri. In terms of long-term changes, it has been reported that the ENSO teleconnection has enhanced under a warming climate, along with its impacts on the southern U.S. [8-10]. In view of this, we also investigate the relationship between ENSO and precipitation across the central U.S. (with emphasis on West-North Central and the Southern Plains) and how that has changed under global warming. This is followed by an assessment of the ability of forecast models to capture the associated circulation anomalies.

The rest of the paper is structured as follows: in Section 2, we outline the methods used to align the typical MJO phase with this case in December 2015, as well as the approach used for assessing the role of the El Niño teleconnection. We move on to results and discussion in Section 3, and provide some concluding remarks in Section 4.

**2. Data and Methodology**

2.1 Data Sources

The Climate Prediction Center's (CPC) model-calculated monthly soil moisture at 0.5° grid spacing is used to estimate monthly soil moisture anomalies [11]. For precipitation, we utilize the CPC morphing technique (CMORPH, [12]) and the Parameter-Elevation Regressions on Independent Slopes Model (PRISM, [13]) datasets for daily and monthly fields respectively. To analyze atmospheric circulation, output from the National Centers for Environmental Prediction/National Center for Atmospheric Research (NCEP/NCAR) global reanalysis at 2.5-degree resolution is used [14].

Attribution analysis is carried out by assessing current and future changes to ENSO's teleconnection impact on precipitation using 17 models from phase 5 of the Coupled Model Intercomparison Project (CMIP5). We specifically analyze two historical single-forcing experiments, i.e. the natural-only forcing (NAT) and the greenhouse gas (GHG)-only forcing [15]. Each experiment produced multiple members initialized from a long-stable preindustrial (1850) control run up to 2005. Table 1 in the supporting information provides the full name, institute, ensemble size, and spatial resolution of each model.

To assess the subseasonal prediction of the December extreme flooding, we evaluate operational forecasts from NCEP's Climate Forecast System version 2 (CFSv2) [16], which includes outputs from four model runs, each made 6-hourly at 00, 06, 12, and 18Z UTC. The forecast from each initial condition covers 9 full months. For daily forecasts, an ensemble of all the 16 initial conditions each day is used. All model forecast products

are re-gridded to a 2.5° × 2.5° resolution to enable comparisons with results from the NCEP/NCAR reanalysis to focus on the large-scale circulation features.

2.2 Determining Relevant MJO Phases

The MJO has often been identified by use of an empirical orthogonal function (EOF) analysis. In this study, the state of the MJO is defined by projecting daily anomaly data onto the leading pair of empirical orthogonal functions (EOFs) of equatorially averaged (15°S-15°N) 200 hPa velocity potential ($\chi_{200}$) fields. The EOF analysis covers a three months' period (Dec 1 - Feb 28), and is performed on yearly basis, i.e. from 1979 to 2015. Prior to the EOF computation, $\chi_{200}$ is bandpass filtered to the intraseasonal period of 30-60 days to isolate the MJO signal, a method dating back to several MJO studies. The MJO can also be viewed in a two-dimensional phase space defined by the two-leading pair of principal component (PC) from the EOF analysis. Since the phase space diagram is a method to observe both the amplitude and the phase of the MJO during its propagation, we construct yearly phase space diagrams and use them to identify "MJO activity days," defined as days when the MJO amplitude ($i.e.\ \sqrt{PC1^2 + PC2^2}$) is greater than or equal to one. Note that before the phase space diagrams are constructed, the two PCs are normalized with their respective mean and standard deviation.

This approach generally follows the methodology of [17] (WH04), but unlike WHO4, we use velocity potential ($\chi_{200}$) for the EOF representation instead of a combination of OLR, 850-hPa zonal wind (u850) and 200-hPa zonal wind (u200). [18] shows that OLR is a relatively noisy field both spatially and temporally, with variability mostly limited to the Eastern Hemisphere. Additionally, the inverse Laplacian used to calculate $\chi_{200}$ acts as

a smoother, which makes $\chi_{200}$ more sensitive to global-scale variations of divergence rather than being concentrated on the Indo-Pacific warm pool like OLR.

2.3 Synoptic Attribution Methods

This section outlines the attribution methods employed to assess the relative contributions of the MJO and El Niño to the synoptic conditions associated with the late December 2015 extreme rainfall, and subsequent flooding in Missouri. This is quite a lengthy section but is necessary to properly interpret the ensuing results from our diagnostic methods.

a. The 2015 December MJO Episode

First, the spatial representation and evolution of the MJO event during which the late December 2015 Missouri flooding occurred is constructed. For the remainder of this paper, we call this MJO event the "December MJO episode." In accordance with the phase space diagram for year 2015, the spatial evolution of the December MJO episode is developed by averaging all MJO activity days (*i.e. amplitude* $\geq 1$) in each given phase. This is done for both 200 hPa velocity potential ($\chi_{200}$) and streamfunction ($\psi_{200}$) over a domain spanning the globe longitudinally and from latitude 40ºS-80ºN. Both $\chi_{200}$ and $\psi_{200}$ are bandpass-filtered within a 30-60 day intraseasonal frequency.

Next, we take an approach based on the idea that the contribution of the December MJO episode to the synoptic conditions that caused the Missouri flooding can statistically be separated. This can be achieved through regression analysis that involves an "MJO phase composite" comprising past MJO events with identical characteristics to the

December 2015 MJO episode. In line with this, 36 MJO episodes before 2015 are constructed on yearly basis, from 1979 to 2014 by following the initial steps outlined above. The so-called MJO phase composite is created from these 36 MJO episodes. But before the composition is done, we take measures to ensure that the eight phases of the MJO phase composite can correctly align with the corresponding phases of the December 2015 MJO episode. This is necessary for two reasons: First, it provides an objective basis for a more direct empirical comparison between the MJO's general structure and the December episode. Second, it ensures that the MJO phase composite can serve to attribute the source of the December 2015 circulation anomalies.

To achieve the aforementioned alignment, corresponding phases of the December 2015 MJO episode and past MJO episodes are subjected to a spatial correlation analysis. If the resulting correlation coefficients at all eight phases for any past episode remains robust above 0.8, that episode is retained. Twenty five out of the 36 past MJO episodes satisfy the criteria and are synthesized to create two MJO phase composites - one for $\chi_{200}$ and the other for $\psi_{200}$.

b. MJO Related Anomalies

The MJO's contribution to the synoptic conditions that led to the late December 2015 Missouri flooding is calculated by linearly regressing the eight phases of the 2015 December MJO episode on the eight phases of the MJO phase composite. This can be expressed by

$$Y_{(x,y)} = \alpha X_{(x,y)} + b$$

where $Y$ and $X$ are the December MJO episode and the MJO phase composite respectively, both are on a spatial longitude-latitude (lat-lon) domain. The regression coefficient $\alpha$ is considered an estimate of the historical effect of the MJO in December. Therefore $\alpha_{(x,y)}$ is composed of the regression coefficients of several time series regressions at every given grid point within a specified domain. Consider a least-squares regression between two datasets with eight time steps (representative of the MJO phases) over a lat-lon domain (i.e. 180°E-180°W, 40°S-80°N), instead of a regression between two sets of time series. At this point, the statistical estimation of the MJO "component" of the December 2015 circulation anomalies becomes possible by multiplying the regression output $\alpha_{(x,y)}$ to the December MJO episode at every phase. This is done for both $\chi_{200}$ and $\psi_{200}$.

One may argue that a more straightforward calculation of the MJO's contribution to the flooding can be achieved by simply replacing the MJO phase composite with MJO amplitude in the regression. However, MJO amplitude is calculated from the two leading principal components (PCs) generated through EOF analysis ( $i.e.\,amplitude = \sqrt{PC1^2 + PC2^2}$ ) and therefore, will not include the phase information of the MJO in a regression. While the WH04 RMM indices or PC's of MJO proxies have emerged as the optimal way of explaining MJO variability, unless taken together, a single PC index by itself cannot explain all the variability associated with the MJO. On the other hand, employing the phase composite as used here accounts for both the amplitude of the MJO and its "correct" phase, which is critical in terms of the actual MJO event days. Although somewhat unconventional, our composite approach ensures that both the phasing and amplitude of the MJO are accounted for in the regression.

c. ENSO Related Anomalies

On the seasonal timescale, the effect of the strong El Niño in December 2015 on circulation is also assessed. The ENSO signal is defined as the Niño 3.4 index (N34), i.e. the normalized SST anomaly over the 5° S - 5° N and 170° W-120° W region of the Pacific Ocean. Here, we use monthly N34 anomalies to approximate the impact of ENSO during each phase of the MJO. For each MJO phase, monthly N34 values are assigned to the 25 previously selected past MJO episodes. The initial outcome is a 25-point index for each MJO phase. However, for the subsequent regression analysis we only use a version of each index with N34 anomalies greater than one standard deviation (i.e. strong ENSO events), which we call a "strong N34 index." While this may appear subjective, it follows previous research that during weak ENSO events, there is no clear Pacific/North American oscillation pattern which prevents influential energy propagation towards the continental U.S. [19,20].

To calculate the portion of circulation anomalies attributable to ENSO, $\psi_{200}$ (on a spatial domain) is regressed on the strong N34 index at every phase. The resulting regression outputs are taken as representative of the historic ENSO effect on each MJO phase. We then multiply the regression outputs by values of the N34 index corresponding to the 2015 December MJO episode, to obtain statistical estimates of the December 2015 circulation anomalies attributable to the El Niño by phase.

Once the attributable components of the MJO and ENSO have been calculated for the December MJO episode, a synoptic attribution analysis is carried out. For $\chi_{200}$, we only remove MJO component (i.e. the portion of the circulation anomalies attributable to the MJO) from the December MJO episode. For $\psi_{200}$ , both the MJO and ENSO components (i.e. the typical MJO impact, plus strong ENSO signals regressed out of the 2015 December

MJO signal) are removed. What is left, the residual, is then regarded as the portion of the circulation that cannot be explained by ENSO and the MJO.

## 3. Results and Discussion

Figure 1 shows the synoptic evolution leading up to the late December 2015 extreme precipitation event and characteristics of the moisture fields associated with it. Precipitation occurred during an extended period (Dec 25-28) over several central U.S. states in a band of thunderstorms generally stretching from Illinois to Texas, with a center over Missouri. Concomitant with this was a quasi-stationary trough over the western U.S., which deepened prior to inducing the strongest precipitation event on December 27. Markedly, the anomalies of vertically integrated moisture flux as shown in Figure 1 are effective in highlighting the strongest areas of moisture transport associated with the heaviest rainfall, where instability remained strong upstream of the trough along the axis of the mean wind.

To characterize the December 2015 circulation patterns and associated ENSO teleconnection, we first show in Figure 3a a regression of the Niño 3.4 index on 250-hPa height anomalies from 1950 to 2014, in comparison with the December 2015 circulation anomalies plotted in Figure 3b. A trans-pacific wave train emanating from Asia into North America is discernable in either case, and depicts an anomalous Aleutian low over the Northern Pacific with a height anomaly of opposite polarity over the Plains states [21].

Next, we illustrate in Figure 3c the Hovmöller diagram of the 20-year sliding correlation between Niño 3.4 and precipitation averages along a longitudinal cross section of the central U.S. (95°W-85°W; during December), to depict the link between the

changing ENSO teleconnection pattern and local precipitation response. The 20-year sliding window is chosen to examine the decadal-scale variations between ENSO and precipitation [22]. There exists an apparent "regime change" in the ENSO-related precipitation anomalies across the target region, from being negatively correlated before 1950 to positively and significantly correlated after 1970. This implies a general amplification effect of the El Niño teleconnection on Southern Plains precipitation as was reported in [10,23]. Different sliding windows ranging from 10 to 25 years were also tested. The result did not indicate any significant difference in the correlation pattern.

The MJO episodes embedded in the December 2015 event are also examined. Figure 4a illustrates the evolution of the global $\chi_{200}$ from early December to mid-January, revealing an eastward propagating pattern that shows a clear association with the MJO. As expected, the December MJO episode (Figure 4a) and the corresponding composite of past MJO cycles (Figure 4b; created from the alignment method introduced in Section 2.2a) show a coherent eastward propagation. While it may be difficult to differentiate between the two patterns, the residual plot in Figure 4c, computed by subtracting Figure 4b from Figure 4a, does show only regional and somewhat stationary features. This implies that the MJO did have a discernable impact on the global divergent circulation during December 2015. The inadvertent difference in magnitude between the phases of the December MJO episode and that of the composite may be considered a limitation in our regression approach. Although all MJO event days are selected using the same criteria, the magnitude of a well-defined MJO event (amplitude $\geq 1$ for consecutive pentads and lasts longer than 25 days, Figure 2b) like the December episode would always be greater than that of any

MJO composite. However, a correct phase of the MJO is equally important as its amplitude to North American weather (24-25) and is a key factor in the context of this study.

One of the fundamental and underlying mechanisms by which tropical convection, such as that associated with the MJO excites Pacific/North American (PNA) like teleconnection patterns (*ref* Figure 3a) is through the linear dispersion of a Rossby wave triggered by the tropical heating [25]. To examine this extratropical wave train induced by the MJO's convective forcing, we repeat the analyses of Figure 4 using $\psi_{200}$. This time, we superimpose the wave-activity flux for stationary waves as derived by [26] (Figure 5). The general characteristics of the anomalous circulation patterns between the December 2015 MJO cycle (Figure 5a) and the composite MJO cycle (Figure 5b) are similar. Focusing on the period prior to the floods (Phase 6), strong Rossby wave trains steadily propagate eastward from the tropical Pacific towards North America during the preceding weeks (phases 4 and 5; Figure 5a). The circulation patterns from phases 4 to 6, particularly in phase 6, resemble the ENSO-induced teleconnection pattern; these are consistent with previous findings that MJO-storm track variability associated with ENSO and phases 5 and 6 of MJO have qualitatively similar characteristics to that associated with the PNA [27,28]. Furthermore, Figure 5a lends support to the notion that it takes a week for any tropical diabatic heating signal to propagate into North America [29] and about 2 weeks for the extratropical response to fully develop [30]. The relatively strong amplitude of the December MJO (*ref* Figure 2b) forced the eastward flux of Rossby waves which, in turn, triggered robust extratropical atmospheric responses prior to phase 6 (the storm event) as shown by streamfunction and the wave activity flux in Figure 5.

The residuals in Figure 5c reflect what is left from the December 2015 cycle after the linear removal of the combined impacts of the MJO and ENSO, as outlined in sections 2.2b and 2.2c. Of the remaining circulation anomalies, the wave-activity flux in Figure 5c does not resemble any prominent teleconnection source and therefore, mostly comes from internal variability associated with synoptic disturbances over the north Pacific. It is important to mention that, only the removal of strong ENSO events as discussed earlier had a noteworthy impact on the anomalous circulations as seen in Figure 5c. Yet, ENSO's effect was not as large as the MJO's subseasonal contribution. These results demonstrate that the synoptic patterns associated with the heavy precipitation can be primarily attributed to MJO-related circulation anomalies.

As is shown in [31, 32], the extratropical response to the MJO is enhanced when MJO-related convection is in phase with heating and convection anomalies associated with certain ENSO phases. However, attempts to uncover a systematic relationship between the MJO and ENSO have yielded conflicting results [33] due to nonlinearity in their combined impact [33]. Reference [6] showed that the occurrence probabilities of Pacific North America (PNA) like MJO teleconnection patterns are more likely to occur during El Niño periods than during La Nina or neutral periods, while a more recent study by [34] shows that strong MJO activity significantly weakens the atmospheric branch of ENSO. That said, the simple fact that ENSO imprints are longer than the episodic MJO phases makes attribution difficult. These are the likely reasons why the atmospheric signature of a near historical El Niño was relatively weak in comparison to the MJO during late December 2015.

3.1 Climate Change Impacts

Recall that Figure 3c depicts a regime change in the ENSO-related precipitation anomalies across several parts of the Central and Southern Plains. To attribute the causes of this apparent regime change, we repeat the analysis in Figure 3c using two forcing scenarios of 17 CMIP5 models. The result is presented in Figure 6 - the CMIP5 representation of the 20-years sliding correlation between the Nino-3.4 index and precipitation. In the GHG run (Figure 6a), the model spread (contours), along with the ensemble mean (shading), which is the composite mean of 17 models (Table 1), depict a general strengthening of the relationship between ENSO and precipitation across the central U.S. Note that only statistically significant contours based on the Student's t-test at the 95% confidence level are drawn. On the contrary, the NAT run (Figure 6b) exhibits a relatively weak relationship between ENSO and precipitation. Although this result does not directly address the impact of climate change specifically on the December 2015 Missouri flooding, it does lend support to the observations (Figure 6c) and previous studies (e.g., [10]) that the regime change in the ENSO-induced precipitation anomalies across the Southern Plains is likely linked to the warming climate. Further examination of the MJO's effect on precipitation in the Southern Plains will be needed when the CMIP5 models' performance in the tropical intraseasonal variability is improved.

3.2 Climate Forecast Attribution

The fact that both ENSO and MJO are relatively predictable climate features leads to an intuitive question concerning how predictable the MJO's impact on the Dec 2015 event was. We analyze the CFSv2's forecast of the December 2015 case of the MJO and

its related circulation anomalies. We compute the ensemble mean forecast of $\chi_{200}$ (Figure 7a) *and* $\psi_{200}$ (Figure 7b) anomalies relating to phase 6 of the MJO for up to 15 days' lead time. Each forecast is a five-day mean prediction for December 24-28. Generally, the model can resolve both the MJO's velocity potential (Figure 7a) and streamfunction signatures (Figure 7b) up to 15 days in advance; this is consistent with earlier findings from studies of this nature (e.gs. [35,36). The CFSv2 also realistically simulates the spatial patterns of the MJO, although the robustness (correlation score of 0.5 or greater) of the waveform in the streamfunction is underestimated as compared to the observations. Additionally, the pattern correlation between daily December circulation anomalies from model forecasts and the observations is computed for $\chi_{200}$ (Figure 7c) *and* $\psi_{200}$ (Figure 7d) – in terms of a 92-day forecast skill chart. It appears that the highest model skill is achieved in the first 10-20 days after which predictability begins to drop (Figures 7c and 7d), as was the case reported by [36].

When it comes to the MJO, skillful subseasonal predictions with lead times exceeding two weeks are rarely achievable (e.g. [37]). In the case of December 2015, the model skill is particularly low during the two weeks from December 8-21, corresponding to phases 4 and 5 when the MJO is over the maritime continent (Figures 4 and 5). This appears to corroborate the so-called Maritime Continent prediction barrier [38]. Based on Kim et al. (2014), the 2 weeks' time frame also corresponds to the nominal time for the transition between alternative periods of enhanced and suppressed convection by the MJO, and shows prediction of the MJO in the CFSv2 is sensitive to, and varies with MJO phase. Thus, while the forecast skill of the MJO with tropical velocity potential (Figure 7a) is good for about 20 days, the extratropical teleconnection in terms of streamfunction is only

predictable up to five days. This limitation signifies the need to improve the simulation of MJO teleconnection, an outstanding challenge facing intraseasonal prediction as was identified in the recent U.S. Climate Variability and Predictability Program (CLIVAR) Summit Meeting Report (https://indd.adobe.com/view/481cb04c-8540-4a09-b47c-568e5a62e7c3).

## 4. Concluding Remarks

The spatial and temporal features of the large-scale circulation anomalies associated with the late-December 2015 flood in Missouri were analyzed. Through synoptic attribution analyses, we found a constructive interference between certain MJO phases and the El Niño during the time leading up to the Missouri flood. Consequently, an unusually high precipitation event occurred during phase 6 of the MJO cycle, i.e. from 23 to 28 December. At this time, the MJO's convection amplified a trans-Pacific Rossby wave train that resembles the ENSO-driven teleconnection pattern from the tropics to form the constructive interference. This contributed to an energized upper-level circulation and strong jet stream flow over the contiguous United States and led to the advection of intense cyclone activity into the Central and Southern Plains (e.g. [39]). In the long term, the effect of anthropogenic warming on the December event is also implied through the analysis of several CMIP5 models. The models suggest that the response of precipitation in the central U.S. to ENSO would be enhanced owing to a warming climate.

With this study, we seek to provide a meaningful contribution to the literature on the synoptic attribution of climate extremes and help improve the prediction of climate extremes. Examination of the MJO's prediction skill in the CFSv2 shows that the model

realistically simulated the spatial patterns and propagation associated with the MJO during December 2015 up to about 20 days in advance. However, the prediction skill of the MJO in the CFSv2 varied by phase for this event. While this paper generally exploits the predictability of the MJO in the CFSv2 model as has been demonstrated in some past studies, future studies could be centered on how the prediction of the MJO in other climate forecast models are directly related to the forecast of the tropical intraseasonal variations and associated midlatitude teleconnections.

**References**

1. Holmes, R.R.; Watson, K.M.; Harris, T.E. Preliminary Peak Stage and Streamflow Data at Selected U.S. Geological Survey Streamgages for Flooding in the Central and Southeastern United States during December 2015 and January 2016: U.S. Geological Survey Open-File Report 2016–1092; U.S. Geological Survey: Reaton, VA, USA, 2016; p. 27.

2. Hirschboeck, K.K. Climates and floods. In National Water Summary 1988-89 Floods and Droughts: Hydrologic Perspectives on Water Issues; Paulson, R.W., Chase, E.B., Roberts, R.S., Moody, D.W., Eds.; U.S. Geological Survey: Reaton, VA, USA, 1991; pp. 67–88. Available online: http://pubs.usgs.gov/wsp/2375/report.pdf (accessed on 12 June 2016).

3. Higgins, R.W.; Schemm, J.K.E.; Shi, W.; Leetmaa, A. Extreme precipitation events in the Western United States related to tropical forcing. J. Clim. 2000, 13, 793–820.

4. Schubert, S.D.; Chang, Y.; Suarez, M.J.; Pegion, P.J. ENSO and wintertime extreme precipitation events over the contiguous United States. J. Clim. 2008, 21, 22–39.

5. Zhang, C. Madden-julian oscillation: Bridging weather and climate. Bull. Am. Meteorol. Soc. 2013, 94, 1849–1870.

6. Riddle, E.E.; Stoner, M.B.; Johnson, N.C.; L'Heureux, M.L.; Collins, D.C.; Feldstein, S.B. The impact of the MJO on clusters of wintertime circulation anomalies over the North American region. Clim. Dyn. 2013, 40, 1749–1766.

7. Rodney, M.; Lin, H.; Derome, J. Subseasonal Prediction of Wintertime North American Surface Air Temperature during Strong MJO Events. Mon. Weather Rev. 2013, 141, 2897–2909.

8. Meehl, G.A.; Tebaldi, C.; Teng, H.; Peterson, T.C. Current and future U.S. weather extremes and El Niño. Geophys. Res. Lett. 2007, 34, L20704.

9. Stevenson, S.; Fox-Kemper, B.; Jochum, M.; Neale, R.; Deser, C.; Meehl, G. Will There Be a Significant Change to El Niño in the Twenty-First Century? J. Clim. 2012, 25, 2129–2145.

10. Wang, S.-Y.; Huang, W.-R.; Hsu, H.-H.; Gillies, R.R. Role of the strengthened El Niño teleconnection in the May 2015 floods over the southern Great Plains. Geophys. Res. Lett. 2015, 42, 8140–8146.

11. Fan, Y.; van den Dool, H. Climate Prediction Center global monthly soil moisture data set at 0.5 resolution for 1948 to present. J. Geophys. Res. 2004, 109, D10.

12. Joyce, R.J.; Janowiak, J.E.; Arkin, P.A.; Xie, P. CMORPH: A method that produces global precipitation estimates from passive microwave and infrared data at high spatial and temporal resolution. J. Hydrometeorol. 2004, 5, 487–503.

13. Daly, C.; Halbleib, M.; Smith, J.I.; Gibson, W.P.; Doggett, M.K.; Taylor, G.H.; Curtis, J.; Pasteris, P.A. Physiographically-sensitive mapping of temperature and precipitation across the conterminous United States. Int. J. Climatol. 2008, 28, 2031–2064.

14. Kalnay, E.; Kanamitsu, M.; Kistler, R.; Collins, W.; Deaven, D.; Gandin, L.; Iredell, M.; Saha, S.; White, G.; Woollen, J.; et al. The NCEP/NCAR 40-year reanalysis project. Bull. Am. Meteorol. Soc. 1996, 77, 437–471.

15. Taylor, K.E.; Stouffer, R.J.; Meehl, G.A. An overview of CMIP5 and the experiment design. Bull. Am. Meteorol. Soc. 2012, 93, 485–498.

16. Saha, S and Coauthors. The NCEP Climate Forecast System version 2. J. Climate. 2014, 27, 2185–2208

17. Wheeler, M.C.; Hendon, H.H. An All-Season Real-Time Multivariate MJO Index: Development of an Index for Monitoring and Prediction. Mon. Weather Rev. 2004, 132, 1917–1932.

18. Ventrice, M.J.; Wheeler, M.C.; Hendon, H.H.; Schreck, C.J.; Thorncroft, C.D.; Kiladis, G.N. A Modified Multivariate Madden–Julian Oscillation Index Using Velocity Potential. Mon. Weather Rev. 2013, 141, 4197–4210.

19. Huang, J.; Higuchi, K.; Shabbar, A. The relationship between the North Atlantic Oscillation and El Nino-Southern Oscillation. Geophys. Res. Lett. 1998, 25, 2707–2710.

20. Mourtzinis, S.; Ortiz, B.V.; Damiandis, D. Climate Change and ENSO Effects on Southeastern US Climate Patterns and Maize Yield. Sci. Rep. 2016, 6, 29777. [PubMed]

21. Chen, T. A. North Pacific Short-Wave Train during the Extreme Phases of ENSO. J. Clim. 2002, 15, 2359–2376.

22. McCabe, G.J.; Dettinger, M.D. Decadal variations in the strength of ENSO teleconnections with precipitation in the western United States. Int. J. Climatol. 1999, 19, 1399–1410.

23. Bonfils, C.J.; Santer, B.D.; Phillips, T.J.; Marvel, K.; Leung, L.R.; Doutriaux, C.; Capotondi, A Relative Contributions of Mean-State Shifts and ENSO-Driven Variability to Precipitation Changes in a Warming Climate. J. Clim. 2015, 28, 9997–10013.

24. Yao, W.; Lin, H.; Derome, J. Submonthly Forecasting of Winter Surface Air Temperature in North America Based on Organized Tropical Convection. Atmos. Ocean 2011, 49, 51–60.

25. Johnson, R.H.; Ciesielski, P.E. Structure and Properties of Madden–Julian Oscillations Deduced from DYNAMO Sounding Arrays. J. Atmos. Sci. 2013, 70, 3157–3179.

26. Takaya, K. and Nakamura, H. A Formulation of a Phase-Independent Wave-Activity Flux for Stationary and Migratory Quasigeostrophic Eddies on a Zonally Varying Basic Flow. J. Atmos. Sci. 2001, 58, 608–627

27. Grise, K.M.; Son, S.-W.; Gyakum, J.R. Intraseasonal and Interannual Variability in North American Storm Tracks and Its Relationship to Equatorial Pacific Variability. Mon. Weather Rev. 2013, 141, 3610–3625.

28. Goss, M.; Feldstein, S.B. The impact of the initial flow on the extratropical response to Madden–Julian oscillation convective heating. Mon. Weather Rev. 2015, 143, 1104–1121.

29. Lin, H.; Brunet, G.; Derome, J. The nonlinear transient atmospheric response to tropical forcing. J. Clim. 2007, 20, 5642–5665.

30. Jin, F.; Hoskins, B.J. The direct response to tropical heating in a baroclinic atmosphere. J. Atmos. Sci. 1995, 52, 307–319.

31. Moon, J.Y.; Wang, B.; Ha, K.J. MJO Modulation on 2009/10 winter snowstorms in the United States. J. Clim. 2012, 25, 978–991.

32. Roundy, P.E.; MacRitchie, K.; Asuma, J.; Melino, T. Modulation of the global atmospheric circulation by combined activity in the Madden–Julian Oscillation and the El Niño-Southern Oscillation during Boreal winter. J. Clim. 2010, 23, 4045–4059.

33. Hendon, H.H.; Wheeler, M.C.; and Zhang, C. Seasonal Dependence of the MJO–ENSO Relationship. J. Climate. 2007, 20, 531–543

34. Hoell, A.; Barlow, M.; Wheeler, M.C.; Funk, C. Disruptions of El Niño–Southern Oscillation Teleconnections by the Madden–Julian Oscillation. Geophys. Res. Lett. 2014, 41, 998–1004.

35. Weaver, S.J.; Wang, W.Q.; Chen, M.Y.; Kumar, A. Representation of MJOvariability in the NCEP Climate Forecast System. J. Clim. 2011, 24, 4676–4694

36. Wang, W.; Hung, M.P.; Weaver, S.J.; Kumar, A.; Fu, X. MJO prediction in the NCEP climate forecast system version 2. Clim. Dyn. 2014, 42, pp. 2509-2520

37. Liu X, Wu T, Yang S, Li T, Jie W, Zhang L, Wang Z, Liang X, Li Q, Cheng Y, Ren H, Fang Y, Nie S (2016) MJO prediction using the sub-seasonal to seasonal forecast model of Beijing Climate Center. Clim Dyn.

38. Vintzileos, A and Pan, H.-L. On the importance of horizontal resolution and initial conditions to forecasting tropical intraseasonal oscillations: The Maritime Continent prediction barrier. Extended Abstracts, 2007 NOAA/CTB-COLA Joint Seminar, Camp Springs, MD, NOAA/CTB and COLA

39. Bell, G.D.; Janowiak, J.E. Atmospheric Circulation Associated with the Midwest Floods of 1993. Bull. Am. Meteorol. Soc. 1995, 76, 681–695.

**Figures**
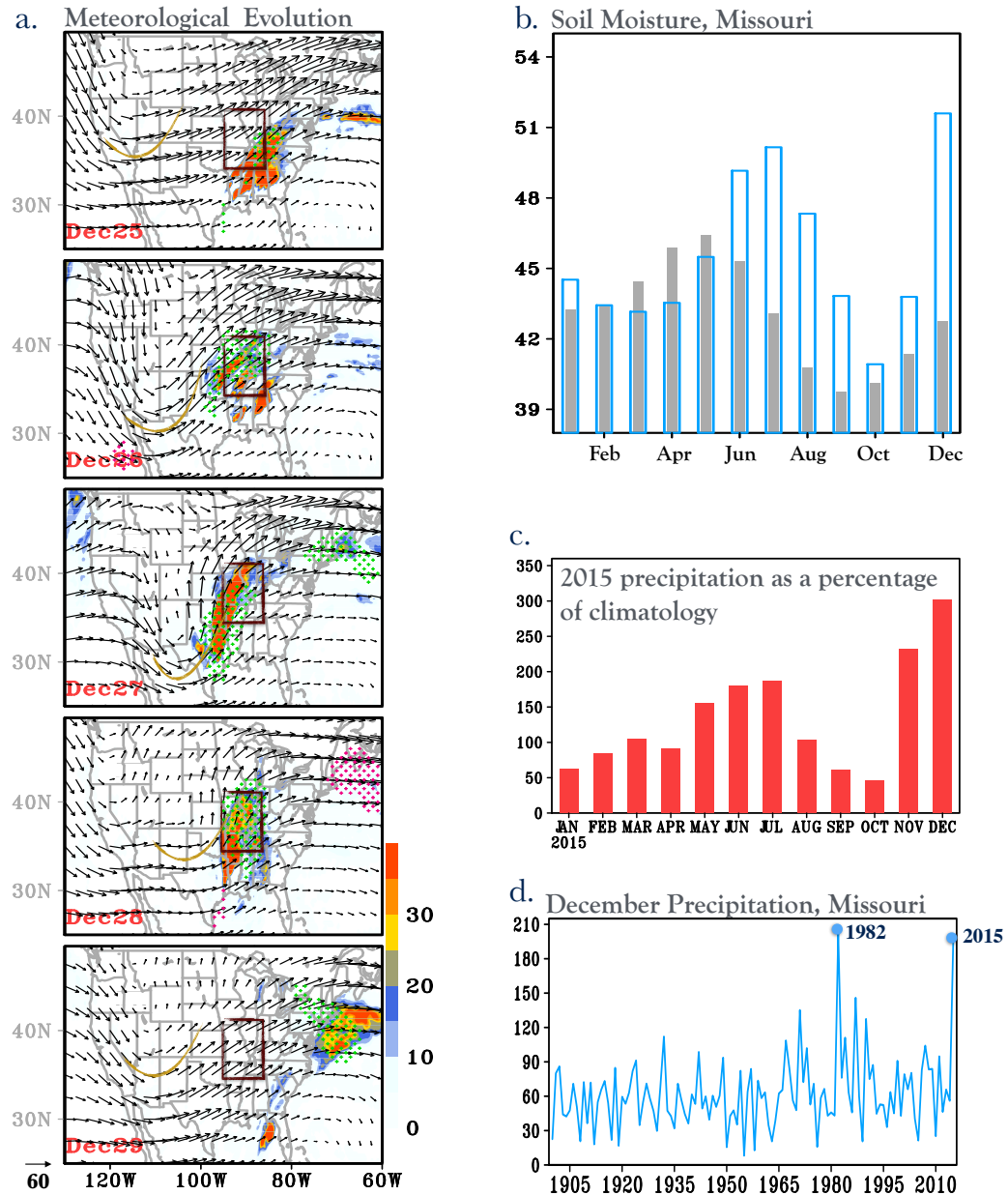


**Figure 4-1 a.** Meteorological evolution of the late December event: 250-hPa winds (vectors) and precipitation (mm, shading), from 25–29 Dec 2015. Areas of positive (negative) vertically integrated (from 1000-300 mb) moisture flux convergence greater than $3x10^{-4}$ kgs⁻¹ are represented by magenta (green) stipplings. Upper-level short wave troughs are marked with yellow curves. The dark red box delineates the most affected storm areas, i.e. the study region. **b.** 2015 monthly soil moisture (blue outline) (cm) in comparison to the 1950-2010 climatology (gray bars). **c.** 2015 monthly precipitation (bars) expressed as a percentage of the 1950-2010 climatology and **d.** Statewide December precipitation (mm, time series) for Missouri.
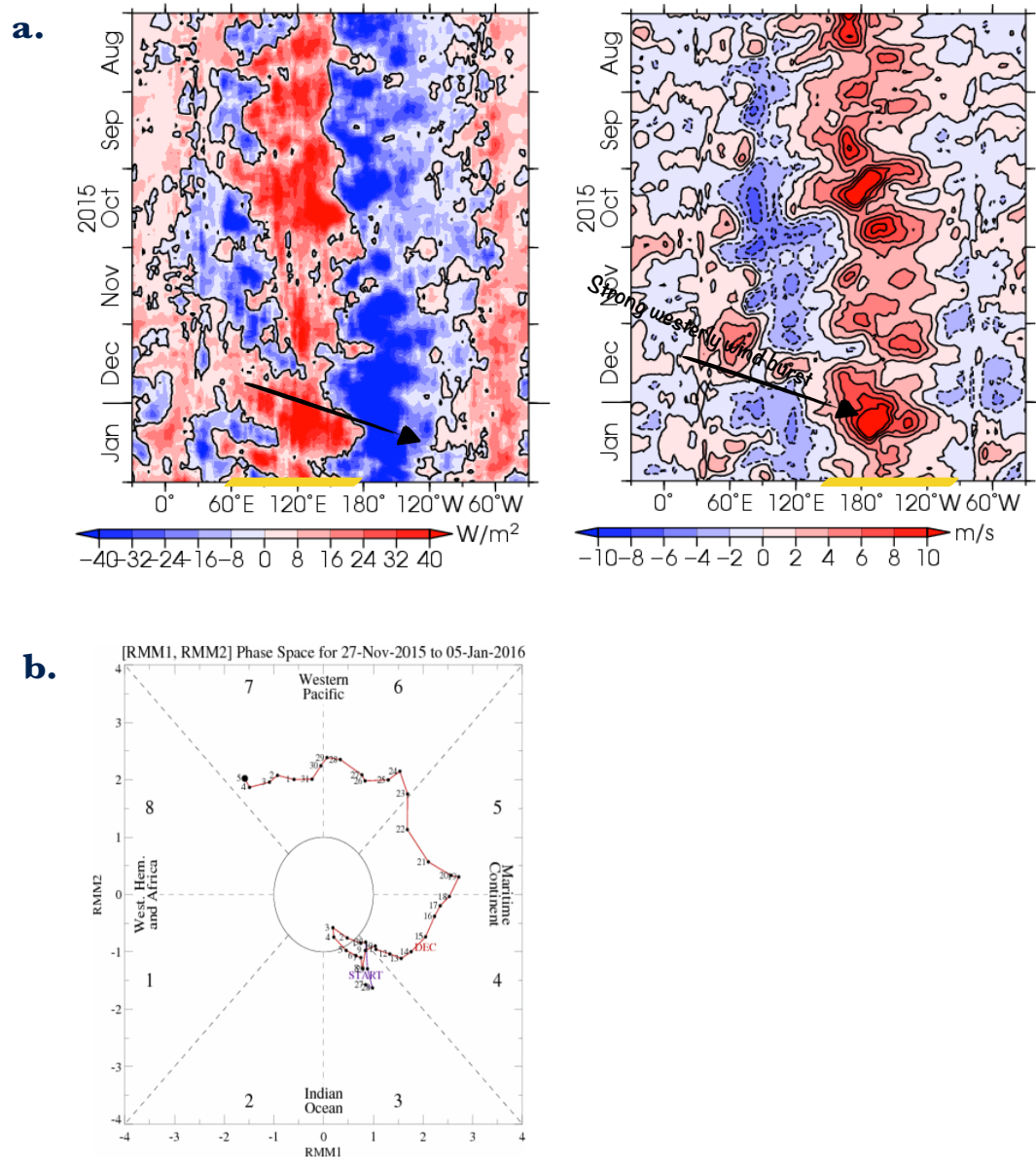
**Figure 4-2** Longitude-time plot of the 7-day mean **a.** outgoing longwave radiation (OLR) and 850 mb wind anomalies (base period: 1981-2010) averaged over 5S-5N, from July-Dec 2015. The thick yellow bars on the longitudinal axes highlight the ENSO region. **b.** Phase space diagram for 27Nov2015 - 5Jan2016 illustrating the phase and amplitude of the activity days of the 2015 MJO cycle, based on the principal components (RMM) of the first two EOFs from a combined EOF analysis using 850 hPa zonal wind, 200 hPa zonal wind and OLR. Counter-clockwise movement around the diagram indicates an eastward propagating signal across eight phases from the Indian Ocean to the Pacific and later the western hemisphere. Color of lines distinguish different months and dates are annotated. The farther away from the center of the circle the stronger the MJO signal.
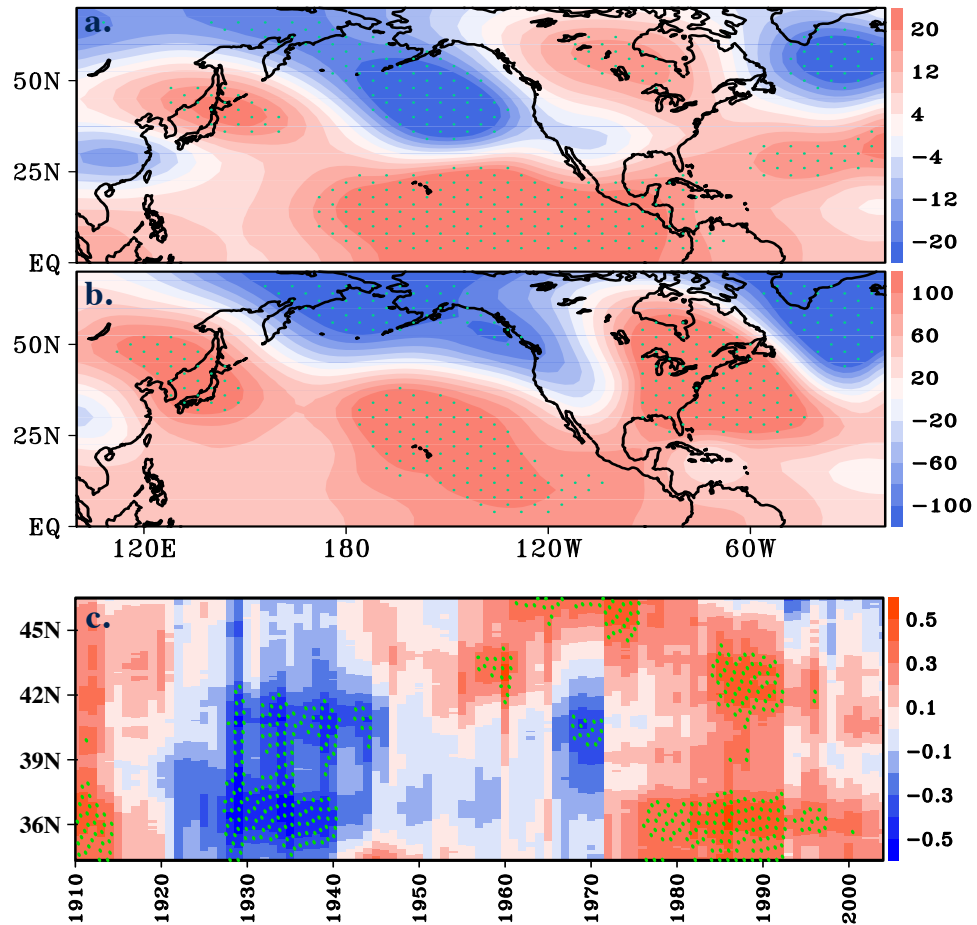
**Figure 4-3 a.** Regression of 250-hPa height anomalies with Niño 3.4 in December, from 1950-2014 **b.** December 2015 250 hPa height anomalies as a departure from the 1950-2010 base period. **c.** Latitude-time plot of the 20-years sliding correlation between Nino 3.4 and December precipitation averaged over longitude 95°W-85°W. On the x-axis are the central years of the correlation window. Green stipplings show significant areas at the 95% confidence level.
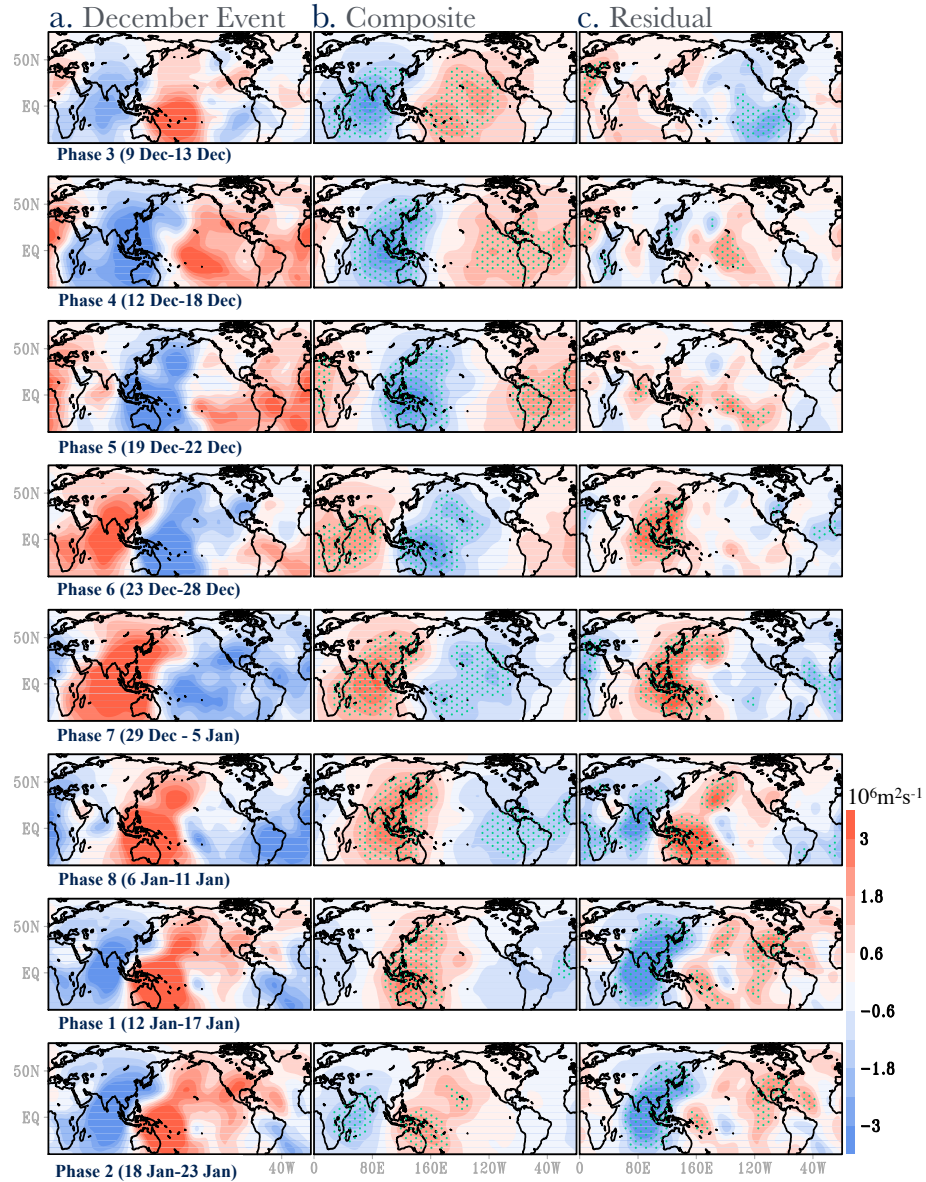
**Figure 4-4 a.** 200-hPa velocity potential anomalies based on the eight phases of the December 2015 MJO episode described in the text. **b.** Composite of 200-hPa velocity potential anomalies based on 25 prior MJO episodes **c.** Velocity potential anomalies not linearly explained by the MJO (i.e. linearly regressed construction of the MJO's impact subtracted from the December event anomalies of χ). Green stipplings show significant areas at the 95% confidence level.
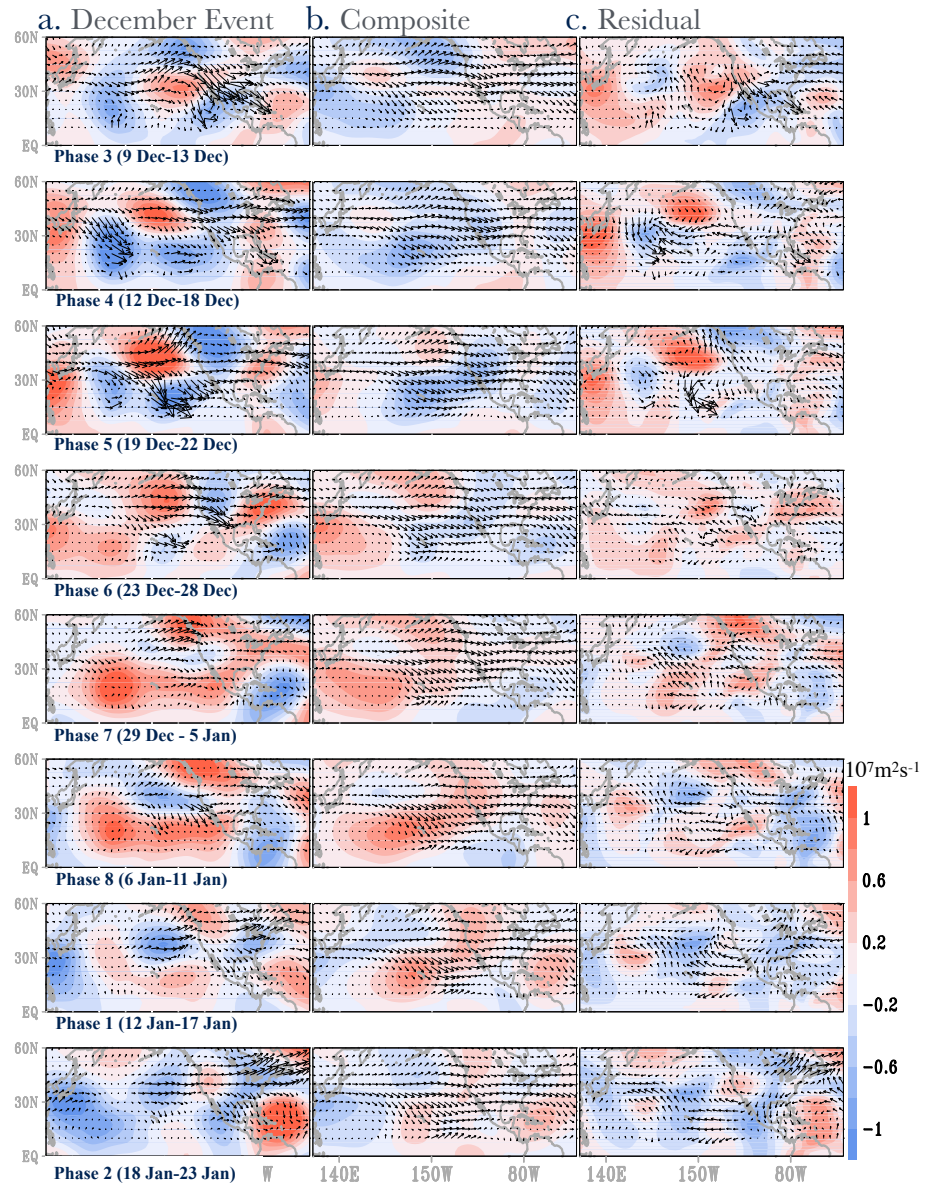
**Figure 4-5 a.** 200-hPa streamfunction anomalies based on the eight phases of the December 2015 MJO episode described in the text. **b.** Composite of 200-hPa streamfunction anomalies based on 25 prior MJO episodes **c.** Streamfunction anomalies not linearly explained by the MJO and ENSO (i.e. linearly regressed constructed impact of both the MJO and ENSO subtracted from the December event anomalies of $\psi$). Corresponding wave-activity fluxes are superimposed in vectors.
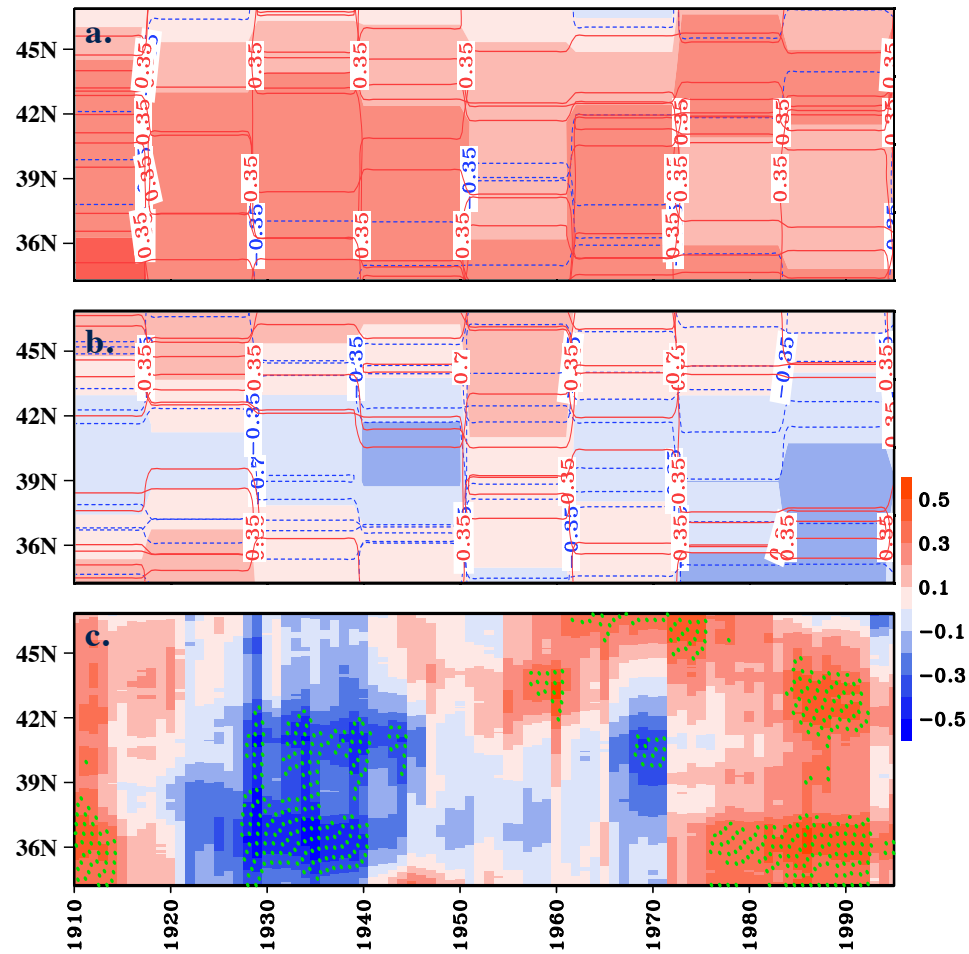
**Figure 4-6** 20-years sliding correlation between the December Nino 3.4 index and precipitation averaged longitudinally over 95°W-85°W, as depicted by 17 CMIP5 models in two scenarios - (a) GHG run and (b) Natural run. Shading represents the ensemble mean. Years on the *x* axis represent the central years of the sliding window. The ensemble spread is in contours and only statistically significant contours based on the Student's t-test at the 95% confidence level are drawn. Figure 6c is a repeat of Figure 3c with a comparable timespan to the model runs.
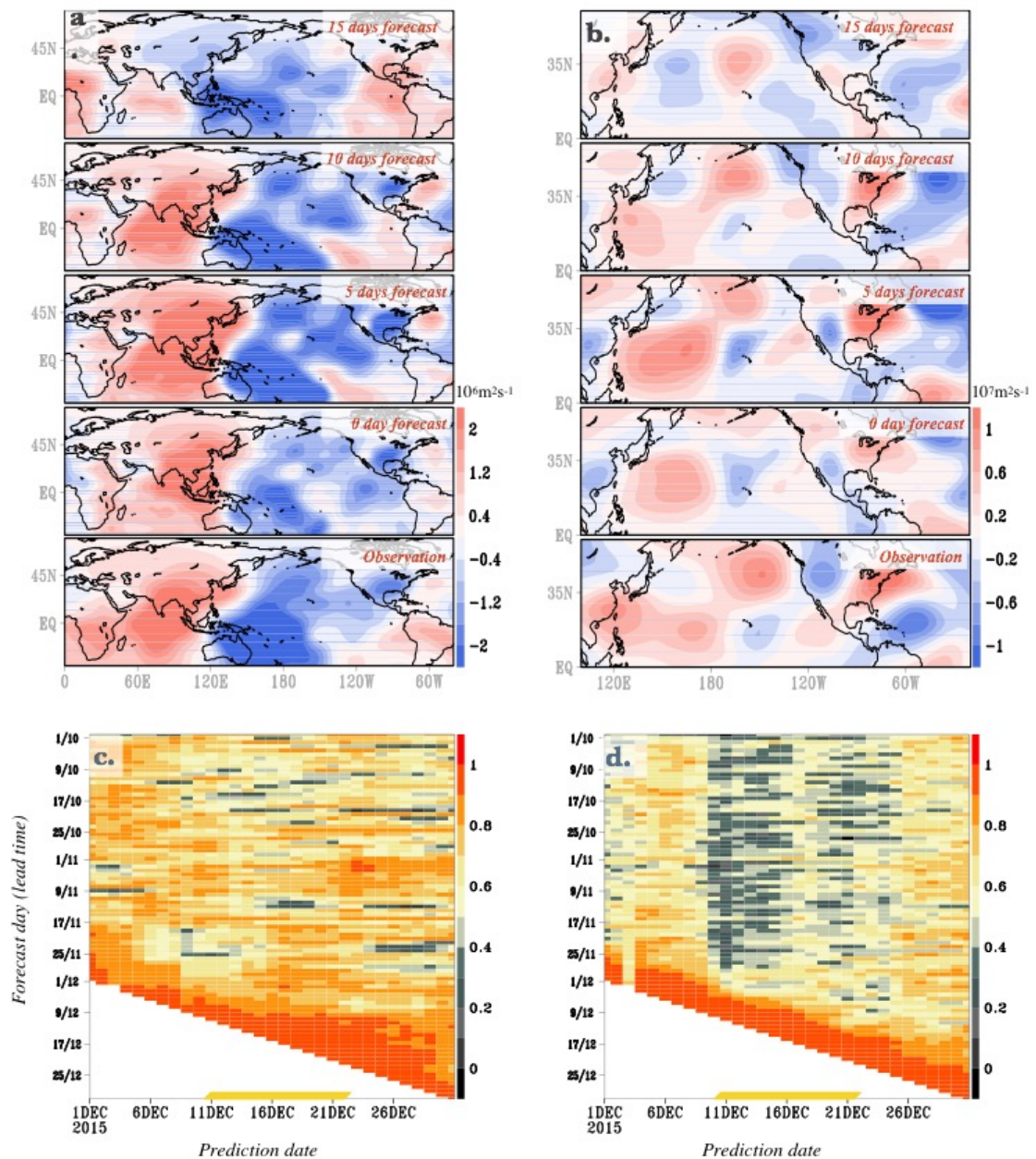
**Figure 4-7** CFSv2 ensemble mean forecast of **a.** χ *and* **b.** ψ anomalies relating to phase 6 of the December MJO episode for up to 15 days' lead time. 92-days forecast of **c.** χ *and d.* ψ *anomalies* that are associated with the MJO for December 2015. The thick yellow lines show the times corresponding to phases 4 and 5 when the MJO is over the maritime continent.

**Table 4-1** Full name, institute, ensemble size, and spatial resolution of the CMIP5 models

| Acronym | Model full name | Center/Institute, country | Resolution (lon.xlat.) | Ensemble size (max) |
|---|---|---|---|---|
| BCC-CSM1 | Beijing Climate Center, Climate System Model, version 1.1 | Beijing Climate Center, Meteorological Administration, China | 2.8° x 2.8° | 1 |
| BNU-ESM | Beijing Normal University—Earth System Model | College of Global Change and Earth System Science (GCESS), China | 2.8° x 2.8° | 1 |
| CanESM2 | Canadian Earth System Model, version 2 | Canadian Center for Climate Modeling and Analysis, Canada | 2.8° x 2.8° | 5 |
| CCSM4 | Community Climate System Model, version 4 | National Center for Atmospheric Research, USA | 1.25°x1.0° | 5 |
| CNRM-CM5 | Centre National de Recherches Météorologiques Coupled Global Climate Model, version 5 | National Centre for Meteorological Research, France | 1.4° x 1.4° | 10 |
| CSIRO-Mk3 | Commonwealth Scientific and Industrial Research Organisation Mark, version 3.6.0 | Commonwealth Scientific and Industrial Research Organization/ Queensland Climate Change Centre of | 1.8° x 1.8° | 10 |
| FGOALS-g2 | Flexible Global Ocean-Atmosphere-Land System Model, grid point version 2 | LASG, Institute of Atmospheric Physics, Chinese Academy of Sciences, China | 2.8° x 1.6° | 4 |
| GFDL-CM3 | Geophysical Fluid Dynamics Laboratory Climate Model version 3 | NOAA Geophysical Fluid Dynamics Laboratory, USA | 2.5° x 2.0° | 5 |
| GFDL-ESM2 | Geophysical Fluid Dynamics Laboratory Earth Science Model 2 with Modular Ocean Model (MOM), version 4.1 | NOAA Geophysical Fluid Dynamics Laboratory, USA | 2.5° x 2.0° | 3 |
| GISS-E2-H | Goddard Institute for Space Studies Atmospheric Model E, version 2, coupled with the Hybrid Coordinate Ocean Model | NASA Goddard Institute for Space Studies, USA | 2.5° x 2.0° | 5 |
| GISS-E2-R | Goddard Institute for Space Studies Model E, version 2, coupled with Russell ocean model | NASA Goddard Institute for Space Studies, USA | 2.5° x 2.0° | 5 |
| HadGEM2-ES | Hadley Centre Global Environmental Model 2, Earth System | Met Office Hadley Centre, UK | 1.8° x 1.25° | 4 |
| IPSL-CM5A-MR | L'Institut Pierre-Simon Laplace Coupled Model, version 5A, medium resolution | Institute Pierre Simon Laplace, France | 2.5° x 1.25° | 1 |
| MIROC-ESM-CHEM | Model for Interdisciplinary Research on Climate Earth System Model, chemistry coupled version | Japan Agency for Marine-Earth Science and Technology, Atmosphere and Ocean Research Institute (The | 2.8° x 2.8° | 3 |
| MIROC-ESM | Model for Interdisciplinary Research on Climate Earth System Model | Japan Agency for Marine-Earth Science and Technology, Atmosphere and Ocean Research Institute, and National | 2.8° x 2.8° | 3 |
| MRI-CGCM3 | Meteorological Research Institute Coupled General Circulation Model, version 3 | Meteorological Research Institute, Japan | 1.1° x 1.1° | 3 |
| NorESM1-M | Norwegian Earth System Model, version 1, intermediate resolution | Norwegian Climate Center, Norway | 2.5° x 1.9° | 3 |

CHAPTER 5

UNDERSTANDING LONG-LEAD ENSO PREDICTIONS:  EXPLORING THE

EXTRATROPICS AS A PRIMARY SOURCE OF ENSO'S

ATMOSPHERIC FORCING

ABSTRACT

The Western North Pacific (WNP) mode and the Pacific Meridional Mode (PMM) are two North Pacific ENSO precursor patterns. This study investigates the evolution of the WNP and PMM and their dynamical relationship using a decomposition of the ocean mixed layer heat budget equation and the vertical mass of the Walker circulation. It is found that strong upward equatorial heat flux anomalies and advection occur in concert with a warming SST in both the WNP and the PMM during the development of an El Niño (sign reversed for La Nina), illustrating the two precursor patterns are inherently linked to equatorial ocean dynamics and reflect the dominant mechanisms that lead to SST changes during ENSO development. In the early stages of ENSO development, SST anomalies lag air-sea fluxes by about a season, whiles the development of the PMM generally lags the WNP by another season. In addition, in comparison to the PMM,  the WNP appears to have a more robust temporal and spatial relationship with the Pacific Walker circulation, which is an inherent part of ENSO variability.

**1. Introduction**

Long-lead predictions of the El Niño Southern Oscillation (ENSO) relies critically upon the identification and tracking of the so-called conduits (or precursor patterns) in sea

surface temperature (SST) and wind anomaly fields that precede an ENSO event (Wang et al. 2014). Previous studies have linked the onset of ENSO events to mid-to-high latitude atmospheric variability. Specifically, forcing from the second leading mode of atmospheric variability over the North Pacific, the North Pacific Oscillation (NPO) [Rogers, 1981] is thought to significantly influence the state of the tropical Pacific 12-15 months prior to the maturation of ENSO events.

Higher latitude forcing act through certain conduits or precursor patterns that in turn trigger ENSO. These types of precursors have an ocean temperature component either at the surface or subsurface, tapping into the high heat capacity and slow ocean thermal inertia that aids in predictability. In recent times, two optimal ENSO precursor patterns have been identified in the North Pacific: (1) the analogous western North Pacific (WNP) pattern of SSTA located in the east of Taiwan and south of Japan that forms (with opposite signed SSTA) 1 year before a full-fledged ENSO event (Wang et al. 2012, 2013) and (2) the Pacific Meridional Mode (PMM) over the eastern half of the North Pacific (Chang et al. 2007; Chiang and Vimont 2004) in which the atmospheric variability during the preceding spring influences SSTA across the equatorial Pacific and then triggers ENSO; this is known as the Seasonal Footprinting Mechanism (Alexander et al. 2010; Anderson 2003; Vimont et al. 2001, 2003).

The WNP shares some characteristics with the PMM: both are linked to off-equatorial SSTA and low-level wind anomalies, and both appear to be strongly related to wintertime variability of the NPO [Wang et al. 2012]. However, in contrast to the PMM the WNP is associated with an opposite-signed SSTA dipole located off southeastern Asia and in the western tropical Pacific, which is accompanied by equatorial winds that may

influence the level of oceanic Kelvin wave activity that precedes ENSO events. Additionally, the WNP lasts longer into the year and has stronger correlations with indices of both ENSO (Wang et al. 2012) and the NPO. The improved statistical performance of the WNP with ENSO over the PMM has led to the supposition that the WNP may be an improved conduit and a better predictor between mid-latitude atmospheric variability and ENSO. However, the dynamical processes by which these precursors interact with midlatitude atmospheric forcing and ENSO a year later are poorly understood, particularly in the case of the WNP. Just how independent they are of each other, or a part of the same process is also not clear.

In this study, the extent to which the WNP and PMM precursor patterns are a part of one broad basin-wide dynamic is studied using : (1) the ocean mixed layer heat budget equation (often called the SST heat budget) and (2) the vertical mass flux associated with the local Pacific Walker circulation. Knowledge gained from this study will complement our understanding of ENSO dynamics and predictability.

**2. Datasets**

2.1 Data Sources

The Hadley Centre Sea Ice and Sea Surface Temperature dataset (HadISST) is used to describe global SST variation patterns (Rayner et al. 2003). For analysis of ocean warm water volume and temperature, we utilize the NCEP Global Ocean Data Assimilation System at the resolution of 0.333° latitude × 1.0° longitude with vertical levels ranging from 5 to 4,479 m depth (Behringer et al. 1998). Mass stream function is calculated from

wind variables from the National Centers for Environmental Prediction/National Center for Atmospheric Research reanalysis dataset (NCEP-1; Kalnay et al. 1996)

To calculate the ocean mixed layer heat budget, the following variables and datasets are used: SST from HadISST and Mixed layer depth ($h_m$) from Argo float profiles based on density criterion $\Delta\rho$ =0.03 kg (Gould et al. 2004). Others include wind stress calculated as $\tau = C_D\rho_{air}u^2$ with data from NCEP-1, where $C_D$ is the dimensionless drag coefficient with a typical value of 0.0013, $\rho_{air}$ is the density of air which is equal to 1.22 kg$m^2$, and $U^2$ is wind speed at 10 m. Air-sea heat fluxes ($Q_{net}$) were calculated using NCEP-1.

## 2.2 Precursor Indices

The PMM is a low-frequency atmosphere-ocean coupled variability comprising of opposite-signed meridional sea surface temperature anomalies (SSTA) gradient located in the central-eastern North Pacific, with one sign of the anomaly maximizing in the subtropics (10°–30°N) and the other sign located on the equator (Chiang and Vimont 2004); and is defined using a maximum covariance analysis (MCA) between SST and surface wind anomalies. On the other hand, the WNP is an SSTA dipole in the western North Pacific. It is also defined using MCA between low level winds and SSTA. Inter-seasonal variations are simply identified using the de-trended boreal SSTA in the western North Pacific (122°–132°E to 18°–28°N) centered at the upstream Kuroshio Current east of Taiwan (Wang et al. 2012).

To describe El Niño development, the sign of the WNP must be reversed. Prior to all computations, we de-trend and normalize all indices and variables with their mean and

standard deviation to remove the impact of warming, as well as multi- annual trends that could obscure trends related to interannual variability.

## 3. Physical Background

3.1 Upper-Ocean Mixed Layer Heat Budget

Sea surface temperature is governed by both atmospheric and oceanic processes. On the atmospheric side, wind speed, air temperature, cloudiness, and humidity are the dominant factors regulating the exchange of energy at the sea surface. On the oceanic side, heat transport by currents, vertical mixing, and boundary layer depth influence SST (Deser et al. 2009). A heat budget analysis is therefore performed to estimate the contributions of surface heat fluxes and oceanic processes to the SST change regarding the evolution of ENSO precursor patterns, and variability associated with the development of ENSO. Following Dong et al. 2007, we decompose the SST tendency equation into its various terms, derived by integrating the heat budget over the mixed layer. It can be written as (Fig. 2):

$$\frac{\partial Tm}{\partial T} = \frac{Qnet - q(-h_m)}{\rho_o c_p h_m} - u_m.\nabla T_m + \kappa \nabla^2 T_m - \frac{W_e \Delta T}{h_m}$$

where $T_m$ (approximated with SST) is the mixed layer temperature, $h_m$ is the mixed layer depth, $w_e$ is the entrainment velocity, $\Delta T$ is the temperature difference between the mixed layer and just below the mixed layer, $\kappa$ is eddy diffusivity (set to be 500 $m^2s^{-1}$), $\rho_o$ (1027 $kg$m$^{-3}$) is the reference density of seawater, and $c_p$ (4000 J kg$^{-1}$s k$^{-1}$) is the specific heat of seawater at constant pressure. Here $Qnet$ denotes the net surface heat flux, which is positive into the ocean, and $q(-h_m)$ is the downward radiative heat flux at the bottom of

the mixed layer. The downward radiative heat flux at the bottom of the mixed layer $q(-h_m)$ is derived from the NCEP-1 solar radiation values based on an assumption of exponential decay with depth (Paulson and Simpson 1977; Qiu and Kelly 1993), written as:

$$q(-h_m) = q(0)[\text{Re}^{\left(\frac{-h_m}{\gamma_1}\right)} + (1-R)e^{\left(\frac{-h_m}{\gamma_2}\right)}]$$

where q (0) is the downward shortwave radiative flux at the sea surface; and R, $\gamma_1$, and $\gamma_2$ are constants depending on the water properties as defined by Jerlov (1968). The horizontal velocity $u_m$ includes both the geostrophic ($u_g$) and Ekman ($u_e$) components.

## 3.2 Mass Streamfunction

The El Niño Southern Oscillation (ENSO) is thought to be inextricably connected to the Pacific Walker Circulation (PWC). Conceptually, it is useful to partition the three-dimensional tropical circulation into meridional and zonal components, namely, the Hadley and Walker circulations. But the averaging involved in their definitions can introduce ambiguities, which can be circumvented by first partitioning the total vertical mass flux into components associated with overturning in the meridional and zonal directions, respectively, called the local Hadley and local Walker circulations here. Defining the local Hadley and local Walker circulations this way ensures the pair of two-dimensional overturning circulations can be added to give the original three-dimensional circulation, even when the averages are taken over limited domains (Schwendike et al. 2014).

Following Schwendike et al. 2015, a version of the streamfunction ($\psi$)vector method, originally developed by Keyser et al. 1989 is used to decompose the tropical atmosphere into a pair of orthogonal overturning circulations which are the local Hadley and local Walker circulations. If averaged over a restricted latitudinal band, part of the

meridional overturning circulation (the Hadley circulation) is aliased into the definition of the Walker circulation. To avoid this problem, the Walker circulation is defined as the meridional average of the local Walker circulation. This aliasing problem is potentially important when analyzing trends in the Walker circulation as these trends may be conflated with trends in the Hadley circulation.

Mathematically, the structure of PWC can be described by an integral of tangential wind speed along a closed circle of the equatorial Pacific vertical sector, like the Hadley circulation that is usually represented by the mean meridional mass streamfunction, which is computed by the vertical integration of the zonal mean density-weighted meridional wind from the top level downward (Ma et al. 2015). To have a direct measure of the whole structure of PWC, namely the thermally divergent circulation in the vertical plane over the equatorial Pacific, PWC can be defined as an equatorial Pacific zonal circulation cell represented by the zonal mass streamfunction, written in mathematical notation as follows:

$$\psi_z = \frac{\alpha \Delta \varphi}{g} \int_0^p u_D \, d_p$$

where $\psi_z$ denotes the zonal mass streamfunction, $\alpha$ is the radius of Earth, $\Delta \varphi$ is the width of the band 5°S − 5°N along the equator in radians, g is the gravitational acceleration, $u_D$ is the divergent component of the zonal wind, and p is the pressure. The divergent component of the zonal wind is obtained by solving the Poisson equation globally for the potential function with divergence as the forcing term and then calculating the divergent wind. The zonal mass flux streamfunction is computed subsequently by vertically integrating $u_D$ meridionally averaged between 5°S − 5°N, from the top of the troposphere downwards. Thus, the calculation of $\psi_z$ depends on accurate analyses of $u_D$.

**3. Results**

3.1 SST Budget Decomposition

The lead-lag regression of SST and warm water volume (subsurface potential temperature, i.e. from the surface to about 300m depth) on the December-February (DJF) averaged WNP and PMM at different is shown in Fig. 3. In both cases, the linear regression of SSTA depicts a gradual evolution of tropical Pacific SSTA from being negative in DJF to positive after a year (the development of an El Niño the following winter), which is concomitant with the growth of the WWV. Even one year in advance of the maximum surface warming, the precursor of El Niño is visible in the subsurface of the Pacific in both the WNP and PMM. The depression of the WWV, also indicative of the approximate position of the thermocline extends slowly from the west to the east along the equator, and when these warm subsurface temperature anomalies caused by the thermocline deepening move eastward, they are carried by equatorial upwelling to the surface.

In comparison to the SST anomalies, the WWV appears to be the better precursor to ENSO variability as changes in the thermocline can be detected much earlier with WWV as shown in Fig. 3. This is consistent with studies that have shown that ocean WWV is one of the most robust precursors to ENSO (e.g. Hu et al. 2017). Notwithstanding, the differences between WNP and PMM related SSTA and WWV anomalies are not easily discernable. In an attempt to understand the extent to which the WNP and PMM are different, we diagnose further using a decomposition of the SST budget terms.

Before examining the spatial distribution of the SST heat budget terms relative to the two North Pacific ENSO precursors, we evaluate how well the heat balance closes on

the scale of the entire Northern Pacific Ocean (120ºE – 110ºW, 0 – 45ºN). Due to data limitations, the computation is limited to 15 years, from 1995 to 2009. The domain-averaged temperature tendency, Fig. 4, compares well with the sum of contributions from the other terms. The temperature tendency is dominated by the seasonal cycle, mainly controlled by the surface heat fluxes. The surface ocean is warmed during spring and summer and cooled during fall and winter. The second largest term is the advection, which is negative in the domain average. The entrainment term is negative, and comparable to advection in terms of magnitude. The diffusion term is the smallest, and does not contribute much to the mixed layer temperature $T_m$. The sum of all the terms captures not only the seasonal cycle in the temperature tendency, but also the short-term fluctuations. Since the air-sea and advection terms contribute the most to the SST budget equation, we will focus on those two terms going forward.

Prior research has shown that the seasonal cross-correlations of ENSO precursors with the wintertime (December–February; DJF) Niño-3.4 index in the following year has peak correlations occurring at about 4–5 seasons (Wang et al. 2014) for the WNP and three seasons (Chiang and Vimont 2003) for PMM (Fig. 1b). As such, for the remaining set of analysis, we will define the WNP index in winter (i.e. DJF-WNP) and the PMM index in spring (i.e. MAM-PMM). This will help curb any confusion of thought in the results since we are using the optimal precursor index for each precursor mode.

Fig. 5 shows the regression of SSTA (contours) and air-sea fluxes (shading) on the December-February (DJF) averaged WNP and PMM indices at several lead times. In the case of the PMM, the DJF map is slightly obscured since it leads MAM. Clear differences between the WNP and PMM ca now be seen. The initial development of positive heat

fluxes across the equatorial Pacific starts in MAM for both the WNP and PMM. However, there is a strong negative heat flux in the eastern equatorial pacific with the PMM, which gradually transitions to positive in the following seasons. Until the mature ENSO phase, the WNP generally feature a more robust air-sea flux anomalies. This explains why in the summer and fall, an El Nino event (SST, contours) is already perceptible from the WNP (Fig. 5). In contrast, the PMM is only able to project an EL Nino in the fall, a few months before the mature phase of ENSO. Also, the time evolution of ocean heating as seen in Fig. 5 is similar to ocean advection (Fig. 6).

What's more, the monthly lead-lag relationships between heat flux and advection terms of the SST budget, and indices of the WNP and PMM (all meridionally-averaged over 5°S - 5°N) are provided in Fig. 7. The strongest anomalies of both the equatorially-averaged air-sea heat fluxes and advection lead the WNP precursor by about a season (Fig 7a), which is consistent with Fig 5. The PMM (Fig. 7b) associated anomalies become evident a season later. A clearer depiction is by the difference plot in Fig. 7c.

3.2 Pacific Zonal Circulation Variability

The large amplitude of ENSO anomalies in the tropical Pacific is essentially explained by the strong coupling between the Walker circulation, the zonal gradient of sea surface temperature and the longitudinal tilt of the thermocline (Ballester et al. 2017). In line with this, Fig. 8 shows the regional Walker circulation defined by averaging zonal mass streamfunction over the latitudinal band of 5°S - 5°N. Here, zonal mass streamfunction is regressed on the DJF and MAM indices of the WNP and PMM respectively. The thick green bars in Fig. 8 outline the equator-wide domain of the Pacific Walker circulation

(PWC). In general, two distinct cells comprise the regional Pacific Walker circulation throughout the year: one in the equatorial Western Pacific Ocean and the other in the Eastern Pacific, characterized by ascent over the Maritime Continent and western Pacific Ocean and descent in the eastern Pacific during La Nina. The reverse would be true for El Nino conditions. The PWC cell is much more pronounced in the WNP (Fig. 8a) related anomalies than that of the PMM (Fig. 8a) at every lead time, suggesting a stronger association between the WNP and PWC. It appears the WNP dynamical association with the ocean and atmospheric dynamics of ENSO, especially during the early stages of development is stronger than the PMM.

## 4. Summary and Discussion

The mechanisms of two North Pacific ENSO precursor patterns, as well as their differences are studied using terms of the SST heat budget and analysis of the Pacific Walker Circulation from zonal mass stream function. It is found that equatorial heat flux anomalies associated with the WNP start developing in the spring before an ENSO event and lead SST by about a season. This is not surprising since it takes time for ocean subsurface processes to reflect the initial atmospheric heating, which later become evident at the surface as positive SSTA. In the case of the PMM, heat fluxes are not readily visible until the fall. Analysis of the advection term of the SST heat budget leads to a similar conclusion.

During ENSO development, positive air-sea heat fluxes and air-sea coupling feedback play a crucial role. Energy absorbed by the ocean leads to changes in the subsurface heat content. In the western and equatorial Pacific, these changes are known to

enhance oceanic Kelvin wave initiation and propagation which eventually triggers the Bjerknes feedback (Wang et al. 2012, Hu et al. 2017). Ocean advection processes play an important role during the Bjerknes feedback and an El Niño development, driving the initial subsurface warming in the western equatorial Pacific, amplified by the ocean-atmosphere coupling to the east (i.e. central Pacific) through the equatorial undercurrent.

These results explain why the WNP has peak correlation with ENSO a season ahead of the PMM and why at longer lead times, the WNP appears to be a better predictor than the PMM. Recall that peak correlations of DJF-averaged WNP (PMM) with ENSO is maximum at about 4-5 seasons (2-3 seasons) in advance (Fig. 1b). We also find that the PWC cell, which is inherently part of ENSO dynamics and variability is much more pronounced in WNP related anomalies than that of the PMM at every lead time. It must be noted that several studies have shown huge disparities in different reanalysis datasets for SST budget equation terms, particularly the heat fluxes terms (Thumm et al. 2015, Dong et al. 2007). Therefore, care should be taken in interpreting these results.

A possible midlatitude forcing that can link strong air-sea fluxes to the WNP, and the WNP to the PWC is the East Asia Winter Monsoon (EAWM). During the earliest stages of ENSO development ($DJF_{yr-1}$), the EAWM features a predominant low-level northeasterly wind blowing from East Asia to the low latitudes in the western Pacific Ocean. This can cause deep convection over the Maritime Continent, reinforcing the convection center of the Pacific Walker circulation due to the intrusion of cold air carried from land into the tropics. The cold air advection is enhanced in the WNP region leading to the  development of an SST dipole (i.e. the WNP DJF precursor pattern), whereupon wind vectors are directed from the cold WNP region to the warm tropical region. The

persistent westerlies could trigger equatorial Kelvin waves, pushing the tropical convection center and the WWV eastward, eventually leading to an El Nino. Future studies will focus on testing the proposed mechanism and ascertain the degree to which the EAWM modulates the ENSO-related atmospheric forcing along the equatorial Pacific Ocean.

**References**

Alexander MA, Vimont DJ, Chang P and Scott JD (2010) The impact of extratropical atmospheric variability on ENSO: Testing the seasonal footprinting mechanism using coupled model experiments. *J. Clim.*, 23, 2885–2901,

Behringer DW and Xue Y (2004) Evaluation of the global ocean data assimilation system at NCEP: The Pacific Ocean, Eighth Symposium on Integrated Observing and Assimilation System for Atmosphere, Ocean, and Land Surface, AMS 84th Annual Meeting, Seattle, Washington, 11-15.

Ballester J, Bordoni S, Petrova D and Rodo X (2016), Heat advectionprocesses leading to El Ni~no events as depicted by an ensemble of ocean assimilation products, J. Geophys. Res. Oceans, 121, 3710–3729

Bjerknes J (1969) Atmospheric teleconnections from the equatorial Pacific. Mon. Weather Rev., 97, 163-172.

Chang P, Zhang L, Saravanan R, Vimont DJ, Chiang JCH, Ji L, Seidel H and Tippett MK (2007) Pacific meridional mode and El Ni??o - Southern oscillation. *Geophys. Res. Lett.*, 34, 0–4.

Chiang JCH and Vimont DJ (2004) Analogous Pacific and Atlanticmeridional modes of tropical atmosphere–ocean variability, J. Clim., 17,4143–4158

Clarke AJ and Gorder Van (2003) Improving El Niño prediction using a space-time integration of Indo-Pacific winds and equatorial Pacific upper ocean heat content. Geophys Res Lett 30(7):1399

Deser C, Alexander MA, Xie SP, Phillips AS (2010) Sea surface temperature variability: patterns and mechanisms. *Annu. Rev. Mar. Sci.* 2:115–43

Dong SJ, S. T. Gille, and J. Sprintall (2007) An assessment of the Southern Ocean mixed layer heat budget. J. Climate, 20, 4425–4442

Gutzler DS and Harrison D (1987) The structure and evolution of seasonalwind anomalies over the near-equatorial eastern Indian and western Pacific Oceans. Mon Wea Rev 115(1):169–192

Hu Z-Z, Kumar A, Zhu J, Huang B, Tseng Y, Wang X (2017) On the Shortening of the Lead Time of Ocean Warm Water Volume to ENSO SST Since 2000. Scientific Reports 2045-2322

Izumo T, Vialard J, Lengaigne M, de Boyer Montegut C, Behera SK, Luo J-J, Cravatte S, Masson S, Yamagata T (2010) Influence of the state of the Indian Ocean dipole on the following year's El Nino. Nat Geosci 3(3):168–172

Jerlov N G (1968) Optical Oceanography. Elsevier, 199 pp.

Jin F F (1997) An equatorial ocean recharge paradigm for ENSO. Part I: Conceptual model. J. Atmos. Sci., 54, 811-829.

Kalnay E and Coauthors (1996) The NMC/NCAR 40- Year Reanalysis Project. Bull. Am. Meteorol. Soc., 77, 437–471.

Karoly DJ, Plumb RA and Tang M (1989) Examples of the horizontal propagation of quasi-stationary waves. J. Atmos. Sci., 46, 2802–2811

Keyser D, Schmidt BD and Duffy DG (1989) A technique for representing three-dimensional vertical circulations in baroclinic disturbance, Mon. Weather Rev., 117, 2463–2494.

Larson S and Kirtman K (2013) The Pacific Meridional Mode as a trigger for ENSO in a high-resolution coupled model. *Geophys. Res. Lett.*, 40, 3189–3194,

Larson SM and Kirtman BP (2014) The Pacific Meridional Mode as an ENSO Precursor and Predictor in the North American Multi-Model Ensemble. *J. Clim.*, 27, 7018–7032

Ma S and Zhou T (2016) Robust strengthening and westward shift of the tropical Pacific Walker circulation during 1979–2012: a comparison of 7 sets of reanalysis data and 26 CMIP5 models J. Clim. 29 3097–118

McPhaden MJ and Yu X (1999) Equatorial waves and the 1997-1998 El Niño. *Geophys. Res. Lett.*, 26, 2961–2964

Meinen CS, McPhaden MJ (2000) Observations of warm water volume changes in the equatorial Pacific and their relationship to El Nino and La Nina. J Clim 13:3551–3559

Paulson CA and Simpson JJ (1977) Irradiance measurements in the upper ocean. J. Phys. Oceanogr., 7, 952–956.

Penland C, Sardeshmukh PD (1995) The optimal growth of tropical sea surface temperature anomalies. J Clim 8:1999–2024

Qiu B and K. A. Kelly (1993) Upper-ocean heat balance in the Kuroshio Extension region. J. Phys. Oceanogr., 23, 2027– 2041.

Rayner NA, Horton EB, Parker DE, Folland CK and Hackett RB (1996) Version 2.2 of the global sea ice and sea surface temperature data set, 1903–1994, *Clim. Res. Tech. Note CRTN74*, Hadley Cent., Met Office, Bracknell, UK, 1996.

Rogers JC (1981) The north Pacific oscillation. J Climatol 1:39–57.

Schwendike J, Govekar P, Reeder MJ, Wardle R, Berry GJ and Jakob C (2014) Local partitioning of the overturning circulation in the tropics and the connection to the Hadley and Walker circulations. J. Geophys. Res., 119, 1322–1339,

Schwendike J, Berry GJ, Reeder MJ, Jakob C, Govekar P and Wardle R (2015) Trends in the local Hadley and local Walker circulations, J. Geophys. Res. Atmos., 120, 7599–7618

Vimont DJ, Battisti DS and Hirst AC (2001) Footprinting: A seasonal connection between the tropics and mid-latitudes. *Geophys. Res. Lett.*, 28, 3923–3926

Vimont DJ, Wallace JM and Battisti DS (2003) The seasonal footprinting mechanism in the Pacific: Implications for ENSO. *J. Clim.*, 16, 2668–2675

Vimont DJ, Alexander M and Fontaine A (2009) Midlatitude excitation of tropical variability in the pacific: The role of thermodynamic coupling and seasonality. *J. Clim.*, 22, 518–534

Vimont DJ, Alexander MA and Newman M (2014) Optimal growth of Central and East Pacific ENSO events. *Geophys. Res. Lett.*, 41, 4027–4034

Wang S, Heureux ML and Yoon J (2012) Is Global Warming Changing the ENSO Precursor in the Western North Pacific ? 22–25.

Wang S Y, L'Heureux M and Chia HH (2012) ENSO prediction one year in advance using western North Pacific sea surface temperatures. *Geophys. Res. Lett.*, 39, 2–7

Wang SY, Jiang X, Fosu B (2015) Global eastward propagation signals associated with the 4–5-year ENSO cycle. Clim Dyn 44(9):2825–2837

Zhu J, Kumar A, Huang B (2015) The relationship between thermocline depth and SST anomalies in the eastern equatorial Pacific: seasonality and decadal variations. Geophys Res Lett

**Figures**
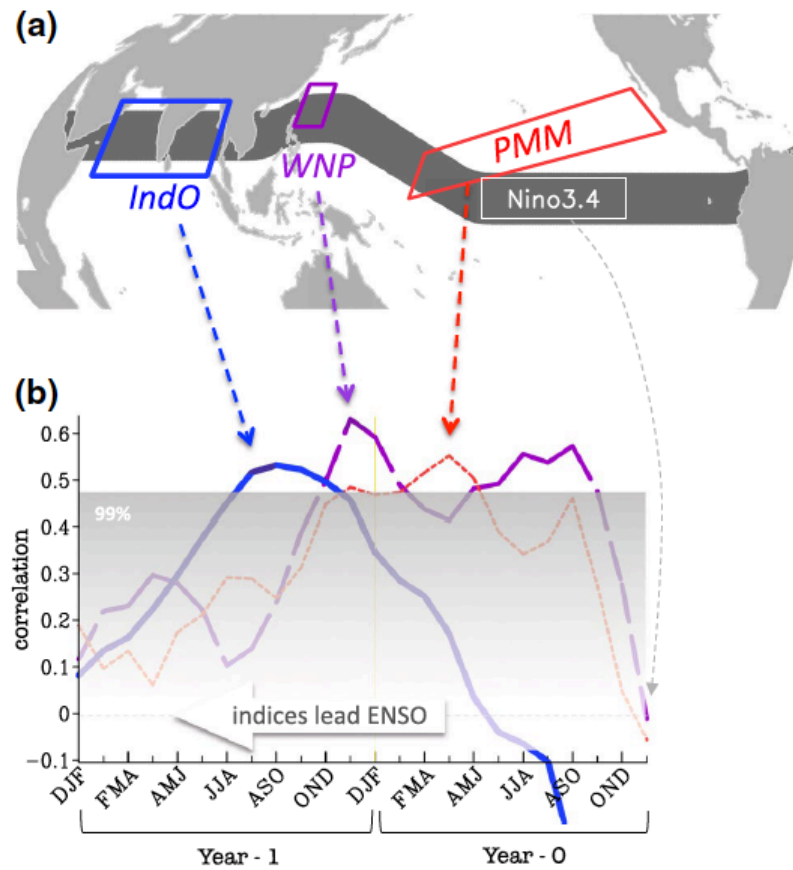


**Figure 5-1** a Domains of common ENSO precursors outlined for the Indian Ocean mode (IndO), the Western North Pacific mode (WNP; sign reversed), the Pacific Meridional Mode (PMM) and the Niño-3.4 region. The dark strip that runs across these three domains indicate the section from which the longitude-time evolution in Figure 4 was constructed. **b** Cross-correlations of the DJF Niño-3.4 index with the 3-month mean IndO (blue), WNP (purple; sign reversed), and PMM (red) over the preceding 2 years. Shaded area indicates the 99 % confidence interval (***Wang et al. 2014).***
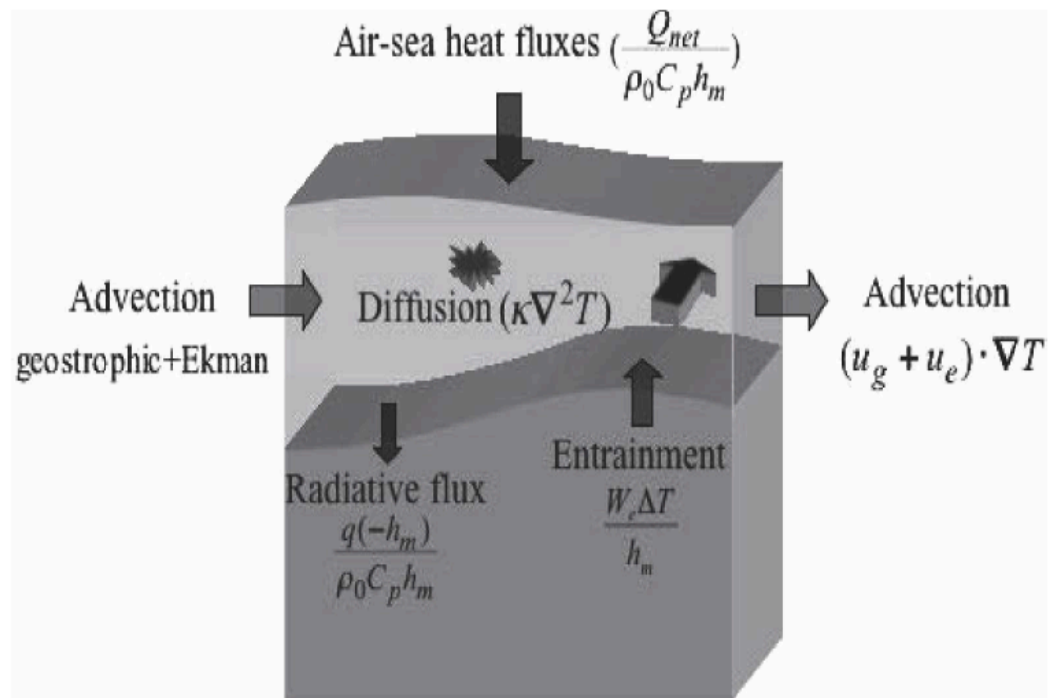
**Figure 5-2** Schematic diagram showing the processes governing the mixed layer temperature variations. Dong et al. 2007
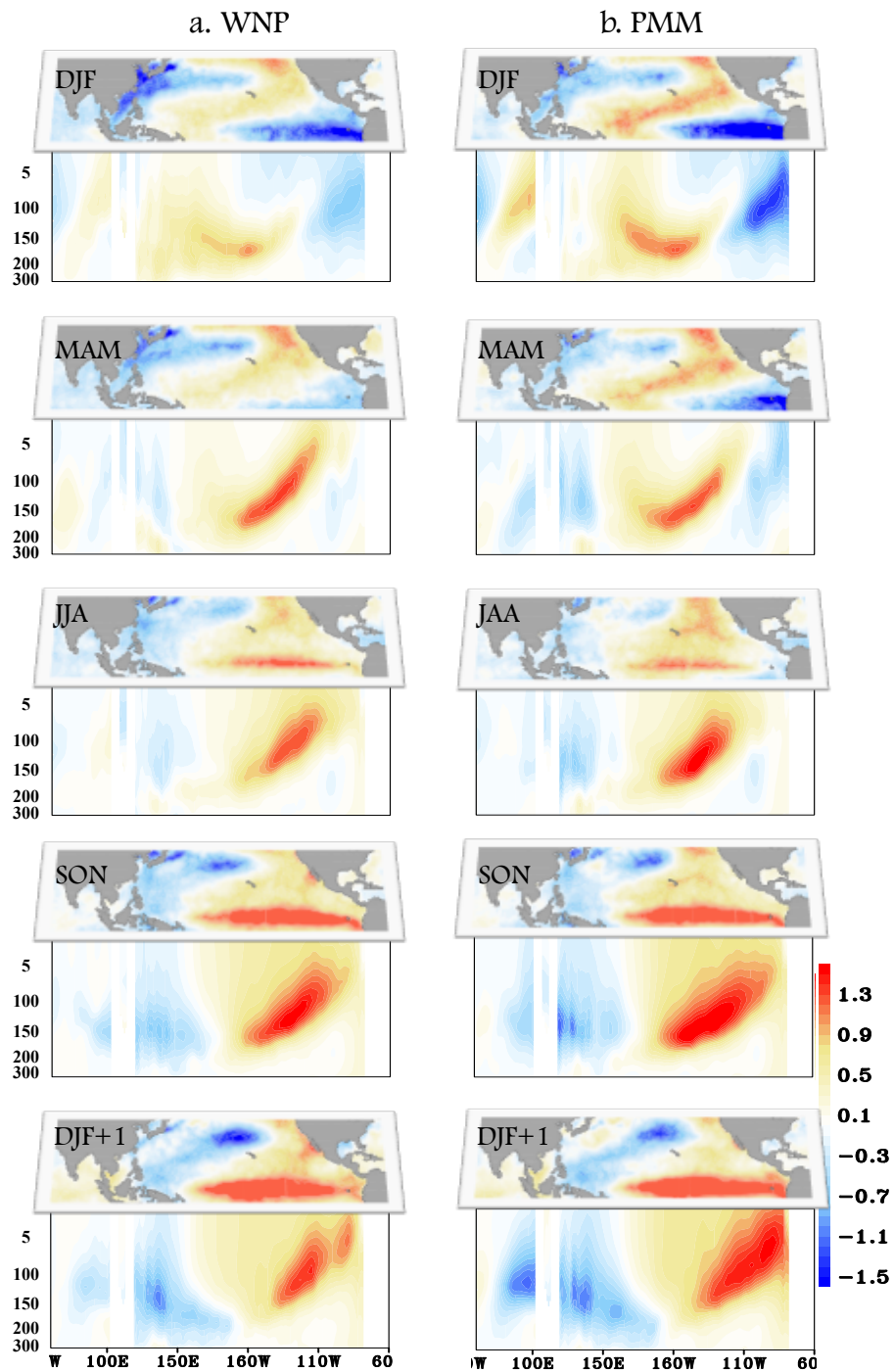
**Figure 5-3 a.** Regression map between the December-February (DJF) averaged WNP index, and SSTA (contours, ºC) and potential temperature anomaly in the upper 300 m of the ocean (shading) at several lead times (MAM, JJA, SON and DJF+1). **b.** Same as **(a)** but for the PMM. The ocean potential temperature was averaged meridionally across 5°S-5°N from 1981-2015.
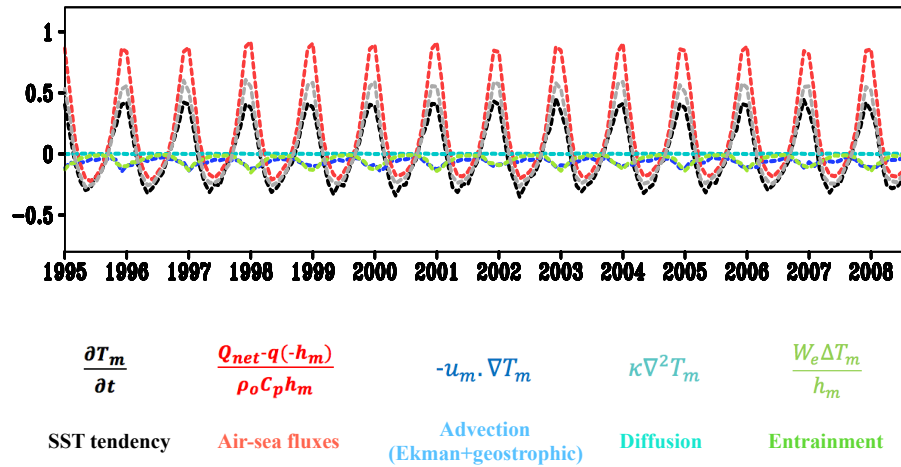
**Figure 5-4** Domain-averaged heat budget ($10^{-6}$°Cs$^{-1}$) in the North Pacific: The gray curve is the sum of the contributions of surface heating (red), oceanic advection(blue), diffusion (cyan), and vertical entrainment (green) to the temperature tendency (black).
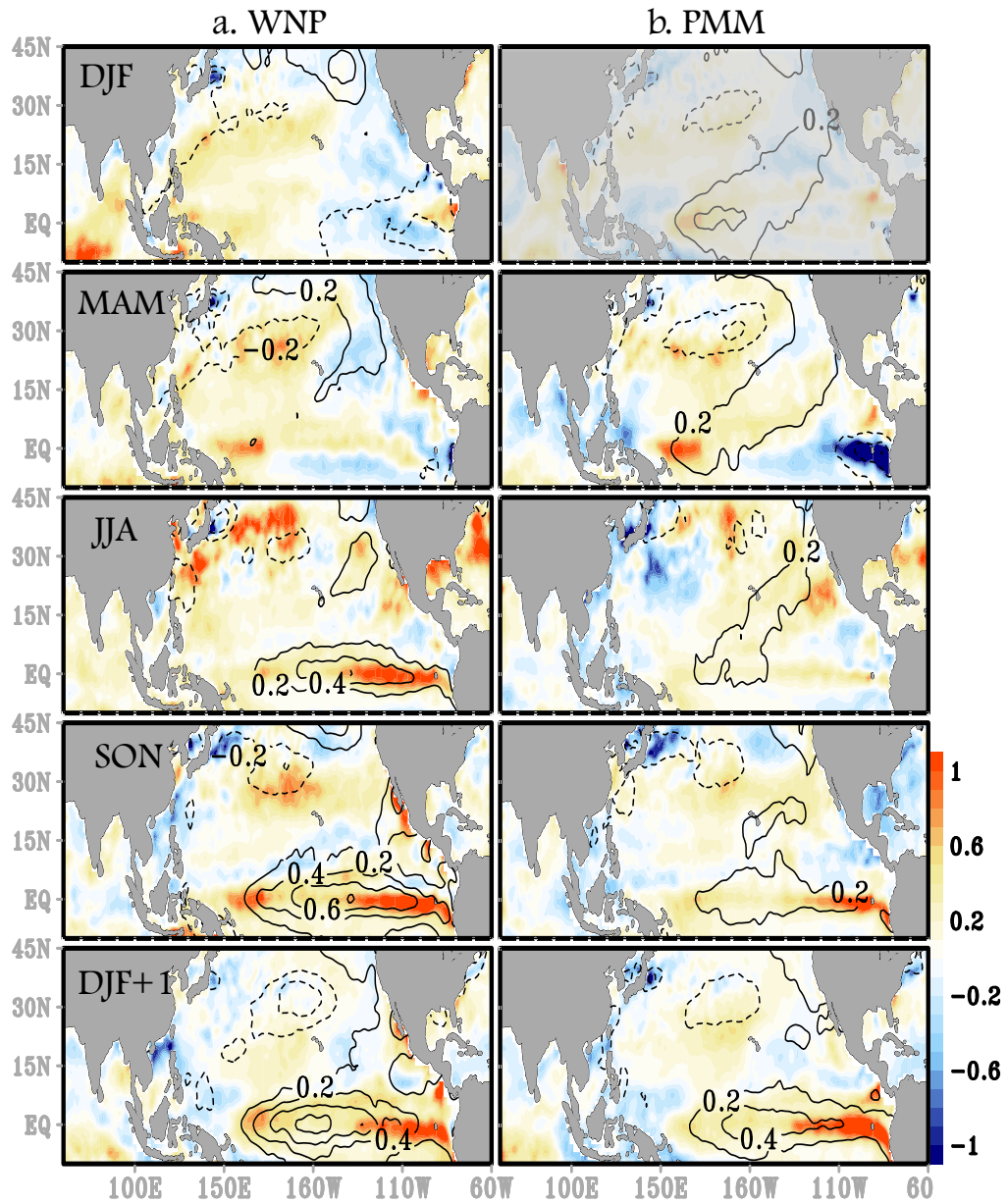
**Figure 5-5 a.** Regression map between the December-February (DJF) averaged WNP index, and SSTA (contours, °C) and air-sea fluxes (shading, $10^{-6}$°Cs$^{-1}$) at several lead times (MAM, JJA, SON and DJF+1). **b.** Same as **(a)** but for the PMM, with its MAM index used in the regression instead of the DJF as used in the case of WNP.
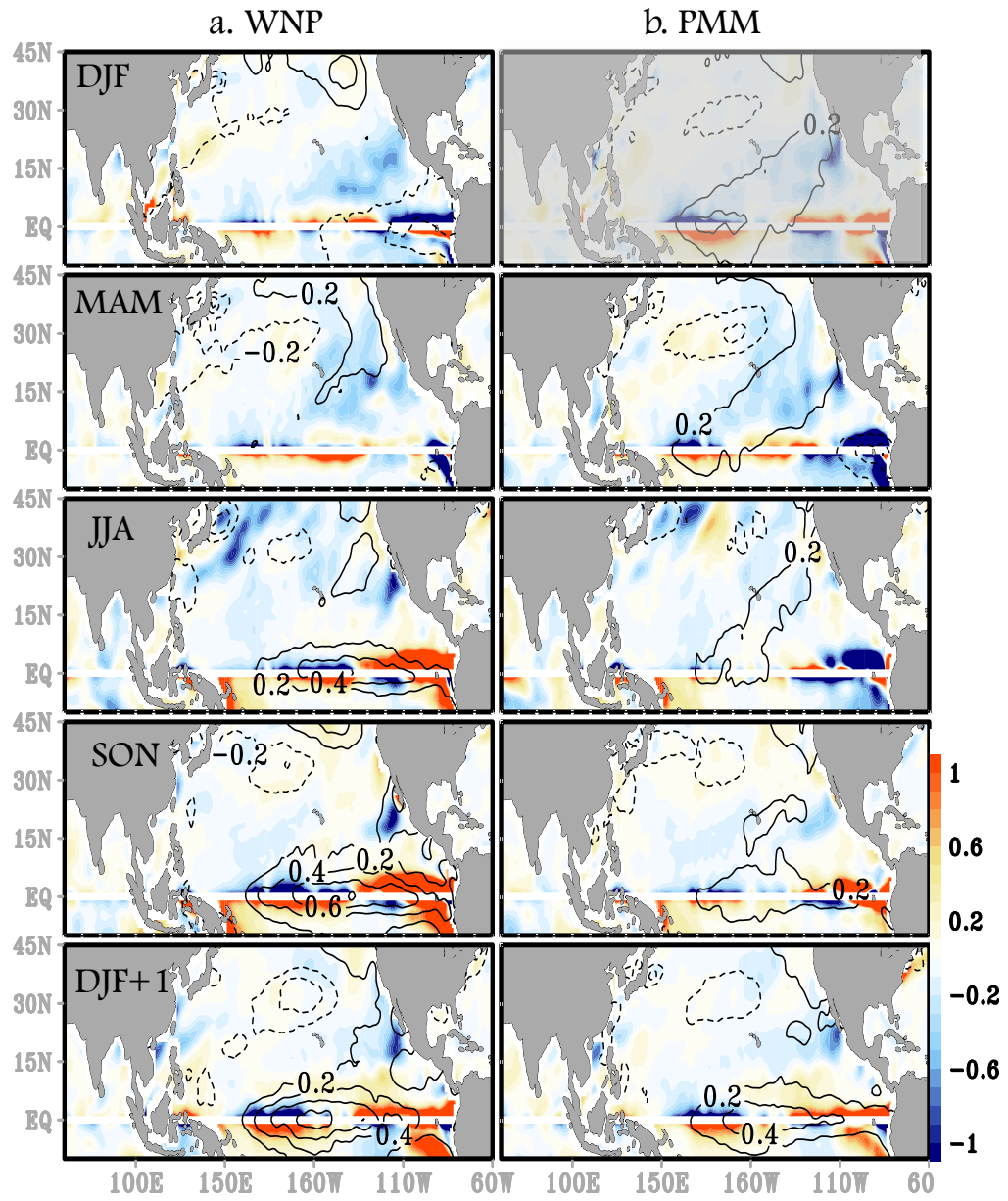
**Figure 5-6** Same as Figure 5 but for the advection term.
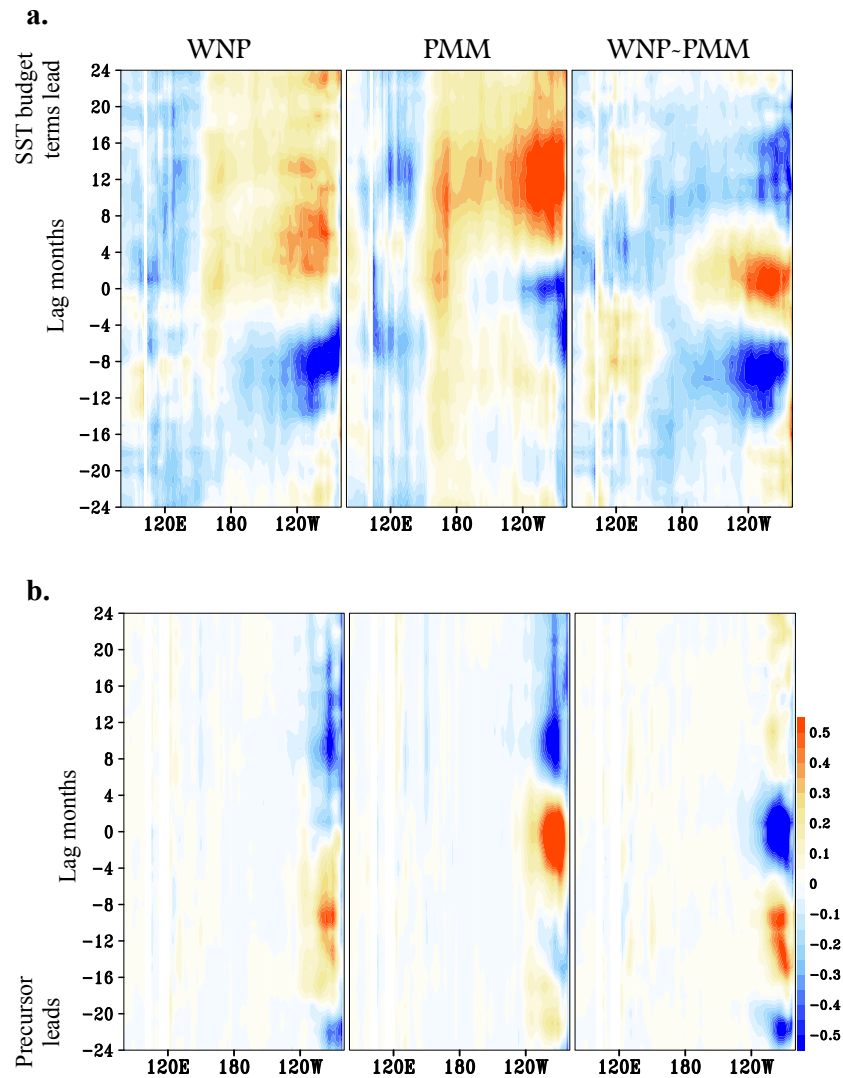
**Figure 5-7** Lead/lag regression between ENSO precursor indices (WNP and PMM) and **a.** Air Sea Fluxes ($10^{-6}$°Cs$^{-1}$) and **b.** Advection ($10^{-6}$°Cs$^{-1}$) meridionally averaged across 5°S-5°N. The lagged correlations include all months and years from 1951-2015.
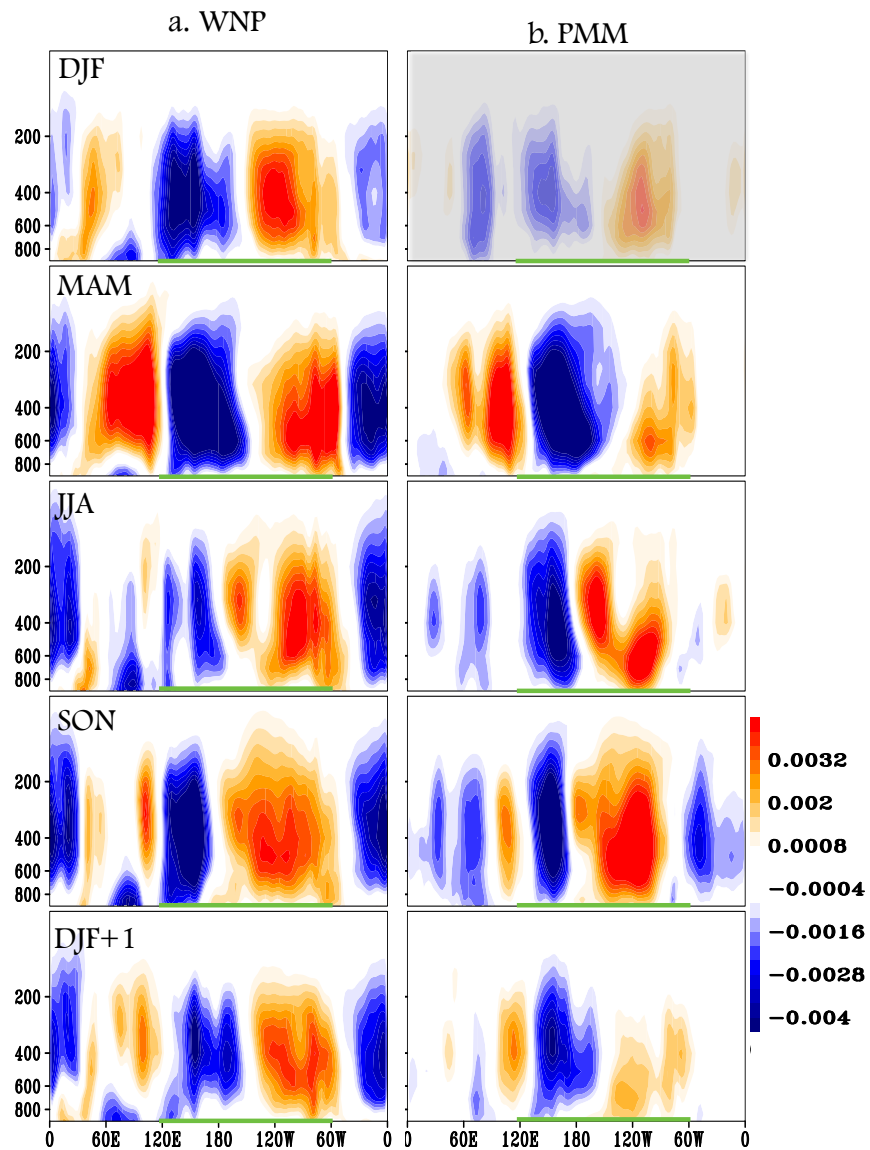
**Figure 5-8** Regression map between the December-February (DJF) averaged WNP index and zonal mass streamfunction (Pacific Walker Circulation, kgm⁻²s⁻¹) at several lead times from 1951-2015. **b.** Same as **(a)** but for the PMM, with its MAM index used in the regression instead of the DJF as used in the case of WNP. The zonal mass streamfunction was averaged meridionally across 5°S-5°N.

CHAPTER 6

CONCLUSIONS

This work was conducted under the broad research theme of climate variability, predictability and change with an emphasis on extreme climate detection, attribution and prediction. Three interrelated, yet regionally unique climate phenomena were investigated to characterize changes in the variability of climate that lead to extremes, augmented by the development of tools to supplement the prediction of climate extremes. At the core of this dissertation is the need to improve weather and climate predictions, particularly for extremes, on time-scales ranging from short forecast lead-times to subseasonal-seasonal climate predictions and beyond.

In Chapter 2 the relationship between increasing greenhouse gas (GHG) emissions and particulate matter (PM) concentration in basin terrain, specifically the IndoGangetic Plains (IGP) was investigated. It was determined that GHG's as a singular factor can lead to a consequent increase in PM concentration (i.e. pollution) even when emissions remain constant – this was hitherto unknown. Moreover, a positive feedback exits whereupon aerosol themselves can induce stabilization in the atmosphere and lead to the accumulation of PM. The knowledge gained from this study can inform scholarly, policy, and public debates on emissions from fossil fuel and biomass burning, especially in basin terrain like the IGP.

The next two Chapters evaluated two extreme phenomena at either side of the water cycle, i.e. droughts and floods. The 2014/15 snowpack drought in Washington state and its climate forcing was evaluated in Chapter 3. This drought resulted from exceedingly high temperatures in the state of Washington notwithstanding normal precipitation. It was found

that the 2014/15 snowpack drought in Washington state was largely driven by natural climate variability in the form of the North Pacific Index (NPI) with a modulation from the North Pacific Oscillation. Specifically, a unique cyclical relationship between temperature and precipitation (both variables averaged along the Washington Cascades) was discovered that is apparently driven by the low frequency variability of the NPI. This three way correspondence between temperature, precipitation and the NPI can be utilized as a supplementary tool for projecting future snowpack droughts and underscores the role naturally driven climate variability can play in forcing severe droughts, especially in a warming world.

On the other end of the spectrum, we conducted research to identify the climate drivers of the late December 2015 flooding in Missouri, discussed in Chapter 4. Results show the severity of the rainfall that resulted in the flooding was caused by an interference between two dominant modes of climate variability, namely the Madden Julian Oscillation (MJO) and the El Niño Southern Oscillation (ENSO). This interaction resulted in a relatively weak atmospheric signature of the El Niño. As a result, the MJO signal dominated the atmospheric circulation anomalies associated with the flooding. The Climate Forecast System version 2 was then tested for performance in reproducing the observed relationship. It was found that when it comes to the MJO, skillful subseasonal predictions with lead times exceeding two weeks are rarely achievable. Next, the influence of anthropogenic climate change on the relationship between ENSO and precipitation across several central US states was also investigated using 17 Coupled Model Intercomparison Project Phase 5 models. A regime change in ENSO-related precipitation anomalies appears to have occurred after 1970, suggesting a likely effect of anthropogenic

warming on the December 2015 extreme precipitation event.

In Chapter 5, we analyzed important mechanisms that govern the evolution of two primary North Pacific ENSO precursor patterns and their relationship using terms of the SST heat budget and analysis of zonal mass stream function associated with the Pacific Walker Circulation. It was found that equatorial heat flux anomalies associated with the WNP start developing in the spring before an ENSO event and lead SST by about a season. In the case of the PMM, heat fluxes were not readily visible until the fall. Analysis of the advection term of the SST heat budget led to a similar conclusion. The results explain why the WNP has peak correlation with ENSO a season ahead of the PMM and why at longer lead times, the WNP appears to be a better predictor than the PMM.

CHAPTER 7

FUTURE STUDIES

**Long-Lead ENSO Predictions**

Wang et al. 2015 argued that the NPO is intrinsically connected to another profound feature associated with ENSO development – the seasonally phase-locked propagation of wind and SSTA signals, which allows tracking of the progression of an ENSO event two years in advance. The phase-locked propagating signal first appears in the eastern Indian Ocean in the middle of the year before an El Niño and then moves eastward, reaching the western Pacific during the beginning of the El Niño year and then amplifying in the central equatorial Pacific (Gutzler and Harrison 1987); similar but opposite-signed propagating signals also appear during La Niña.

Such propagation may signal a connection between the northern/tropical Indian Ocean (IndO) mode, the WNP and The PMM as is illustrated by their seasonal cross-correlations with the wintertime (December–February; DJF) Niño-3.4 index in the following year (Chapter 5, Figure 1b): Peak correlations between IndO and ENSO occur at six seasons prior to a mature ENSO, four to five seasons in WNP and three seasons in PMM. The entire propagation is manifested as a narrow, southwest-northeast oriented SSTA band across the subtropical North Pacific, and its journey takes about 2–3 years (Wang et al. 2015).

Results from Chapter 5 appear consistent with these findings. The fact that air-sea fluxes lead SSTA anomalies for about two seasons in the WNP and the WNP leads the PMM for another seasons seems consistent with the peak correlations shown in Figure 1b.

Future studies will extend the analysis in Chapter 5 to include the northern/tropical Indian Ocean (IndO), and try to answer the following question: to what extent is an IndO, WNP, and PMM part of a broader system that impacts the tropics and ENSO development, and how is this possible pathway intrinsically linked to extratropical climate forcing like the NPO.

**References**

Gutzler DS and Harrison D (1987) The structure and evolution of seasonalwind anomalies over the near-equatorial eastern Indian and western Pacific Oceans. Mon Wea Rev 115(1):169–192

Wang SY, Jiang X, Fosu B (2015) Global eastward propagation signals associated with the 4–5-year ENSO cycle. Clim Dyn 44(9):2825–2837

APPENDICES

# PERMISSIONS AND RELEASE LETTERS

## License Agreement I: Materials for Chapter 2

**JOHN WILEY AND SONS LICENSE
TERMS AND CONDITIONS**

Jul 10, 2018

This Agreement between Boniface Fosu ("You") and John Wiley and Sons ("John Wiley and Sons") consists of your license details and the terms and conditions provided by John Wiley and Sons and Copyright Clearance Center.

| | |
|---|---|
| License Number | 4385451160534 |
| License date | Jul 10, 2018 |
| Licensed Content Publisher | John Wiley and Sons |
| Licensed Content Publication | Atmospheric Science Letters |
| Licensed Content Title | Greenhouse gases stabilizing winter atmosphere in the Indo-Gangetic plains may increase aerosol loading |
| Licensed Content Author | Boniface O. Fosu, S.-Y. Simon Wang, Sheng-Hsiang Wang, et al |
| Licensed Content Date | Apr 5, 2017 |
| Licensed Content Volume | 18 |
| Licensed Content Issue | 4 |
| Licensed Content Pages | 7 |
| Type of use | Dissertation/Thesis |
| Requestor type | Author of this Wiley article |
| Format | Print and electronic |
| Portion | Full article |
| Will you be translating? | No |
| Title of your thesis / dissertation | TOWARDS THE PREDICTION OF CLIMATE EXTREMES WITH ATTRIBUTION ANALYSIS THROUGH CLIMATE DIAGNOSTICS AND MODELING: CASES FROM ASIA TO NORTH AMERICA |
| Expected completion date | Aug 2018 |
| Expected size (number of pages) | 140 |
| Requestor Location | Boniface Fosu<br>441 W 950 N<br>Apt 3<br><br>LOGAN, UT 84321<br>United States |

Attn: Boniface Fosu

| | |
|---|---|
| Publisher Tax ID | EU826007151 |
| Total | 0.00 USD |
| Terms and Conditions | |

**TERMS AND CONDITIONS**

This copyrighted material is owned by or exclusively licensed to John Wiley & Sons, Inc. or one of its group companies (each a"Wiley Company") or handled on behalf of a society with which a Wiley Company has exclusive publishing rights in relation to a particular work (collectively "WILEY"). By clicking "accept" in connection with completing this licensing transaction, you agree that the following terms and conditions apply to this transaction (along with the billing and payment terms and conditions established by the Copyright Clearance Center Inc., ("CCC's Billing and Payment terms and conditions"), at the time that you opened your RightsLink account (these are available at any time at http://myaccount.copyright.com).

**Terms and Conditions**

- The materials you have requested permission to reproduce or reuse (the "Wiley Materials") are protected by copyright.

- You are hereby granted a personal, non-exclusive, non-sub licensable (on a stand- alone basis), non-transferable, worldwide, limited license <u>to reproduce the Wiley Materials for the purpose specified in the licensing process.</u> This license, **and any CONTENT (PDF or image file) purchased as part of your order,** is for a one-timeuse only and limited to any maximum distribution number specified in the license. The first instance of republication or reuse granted by this license must be completed within two years of the date of the grant of this license (although copies prepared before the end date may be distributed thereafter). The Wiley Materials shall not be used in any other manner or for any other purpose, beyond what is granted in the license. Permission is granted subject to an appropriate acknowledgement given to the author, title of the material/book/journal and the publisher. You shall also duplicate the copyright notice that appears in the Wiley publication in your use of the Wiley Material. Permission is also granted on the understanding that nowhere in the text is a previously published source acknowledged for all or part of this Wiley Material. Any third party content is expressly excluded from this permission.

- With respect to the Wiley Materials, all rights are reserved. Except as expressly granted by the terms of the license, no part of the Wiley Materials may be copied, modified, adapted (except for minor reformatting required by the new Publication), translated, reproduced, transferred or distributed, in any form or by any means, and no derivative works may be made based on the Wiley Materials without the prior permission of the respective copyright owner.**For STM Signatory Publishers clearing permission under the terms of the STM Permissions Guidelines only, the terms of the license are extended to include subsequent editions and for editions in other languages, provided such editions are for the work as a whole in situ and does not involve the separate exploitation of the permitted figures or extracts**

- You may not alter, remove or suppress in any manner any copyright, trademark or other notices displayed by the Wiley Materials. You may not license, rent, sell, loan, lease, pledge, offer as security, transfer or assign the Wiley Materials on a stand-alonebasis, or any of the rights granted to you hereunder to any other person.

- The Wiley Materials and all of the intellectual property rights therein shall at all times remain the exclusive property of John Wiley & Sons Inc, the Wiley Companies, or their respective licensors, and your interest therein is only that of having possession of and the right to reproduce the Wiley Materials pursuant to Section 2 herein during the continuance of this Agreement. You agree that you own no right, title or interest in or to the Wiley Materials or any of the intellectual property rights therein. You shall have no rights hereunder other than the license as provided for above in

Section 2. No right, license or interest to any trademark, trade name, service mark or other branding ("Marks") of WILEY or its licensors is granted hereunder, and you agree that you shall not assert any such right, license or interest with respect thereto

- NEITHER WILEY NOR ITS LICENSORS MAKES ANY WARRANTY OR REPRESENTATION OF ANY KIND TO YOU OR ANY THIRD PARTY, EXPRESS, IMPLIED OR STATUTORY, WITH RESPECT TO THE MATERIALS OR THE ACCURACY OF ANY INFORMATION CONTAINED IN THE MATERIALS, INCLUDING, WITHOUT LIMITATION, ANY IMPLIED WARRANTY OF MERCHANTABILITY, ACCURACY, SATISFACTORY QUALITY, FITNESS FOR A PARTICULAR PURPOSE, USABILITY, INTEGRATION OR NON-INFRINGEMENT AND ALL SUCH WARRANTIES ARE HEREBY EXCLUDED BY WILEY AND ITS LICENSORS AND WAIVED BY YOU.

- WILEY shall have the right to terminate this Agreement immediately upon breach of this Agreement by you.

- You shall indemnify, defend and hold harmless WILEY, its Licensors and their respective directors, officers, agents and employees, from and against any actual or threatened claims, demands, causes of action or proceedings arising from any breach of this Agreement by you.

- IN NO EVENT SHALL WILEY OR ITS LICENSORS BE LIABLE TO YOU OR ANY OTHER PARTY OR ANY OTHER PERSON OR ENTITY FOR ANY SPECIAL, CONSEQUENTIAL, INCIDENTAL, INDIRECT, EXEMPLARY OR PUNITIVE DAMAGES, HOWEVER CAUSED, ARISING OUT OF OR IN CONNECTION WITH THE DOWNLOADING, PROVISIONING, VIEWING OR USE OF THE MATERIALS REGARDLESS OF THE FORM OF ACTION, WHETHER FOR BREACH OF CONTRACT, BREACH OF WARRANTY, TORT, NEGLIGENCE, INFRINGEMENT OR OTHERWISE (INCLUDING, WITHOUT LIMITATION, DAMAGES BASED ON LOSS OF PROFITS, DATA, FILES, USE, BUSINESS OPPORTUNITY OR CLAIMS OF THIRD PARTIES), AND WHETHER OR NOT THE PARTY HAS BEEN ADVISED OF THE POSSIBILITY OF SUCH DAMAGES. THIS LIMITATION SHALL APPLY NOTWITHSTANDING ANY FAILURE OF ESSENTIAL PURPOSE OF ANY LIMITED REMEDY PROVIDED HEREIN.

- Should any provision of this Agreement be held by a court of competent jurisdiction to be illegal, invalid, or unenforceable, that provision shall be deemed amended to achieve as nearly as possible the same economic effect as the original provision, and the legality, validity and enforceability of the remaining provisions of this Agreement shall not be affected or impaired thereby.

- The failure of either party to enforce any term or condition of this Agreement shall not constitute a waiver of either party's right to enforce each and every term and condition of this Agreement. No breach under this agreement shall be deemed waived or excused by either party unless such waiver or consent is in writing signed by the party granting such waiver or consent. The waiver by or consent of a party to a breach of any provision of this Agreement shall not operate or be construed as a waiver of or consent to any other or subsequent breach by such other party.

- This Agreement may not be assigned (including by operation of law or otherwise) by you without WILEY's prior written consent.

- Any fee required for this permission shall be non-refundable after thirty (30) days from receipt by the CCC.

- These terms and conditions together with CCC's Billing and Payment terms and conditions (which are incorporated herein) form the entire agreement between you and WILEY concerning this licensing transaction and (in the absence of fraud) supersedes all prior agreements and representations of the parties, oral or written. This Agreement may not be amended except in writing

signed by both parties. This Agreement shall be binding upon and inure to the benefit of the parties' successors, legal representatives, and authorized assigns.

- In the event of any conflict between your obligations established by these terms and conditions and those established by CCC's Billing and Payment terms and conditions, these terms and conditions shall prevail.

- WILEY expressly reserves all rights not specifically granted in the combination of (i) the license details provided by you and accepted in the course of this licensing transaction, (ii) these terms and conditions and (iii) CCC's Billing and Payment terms and conditions.

- This Agreement will be void if the Type of Use, Format, Circulation, or Requestor Type was misrepresented during the licensing process.

- This Agreement shall be governed by and construed in accordance with the laws of the State of New York, USA, without regards to such state's conflict of law rules. Any legal action, suit or proceeding arising out of or relating to these Terms and Conditions or the breach thereof shall be instituted in a court of competent jurisdiction in New York County in the State of New York in the United States of America and each party hereby consents and submits to the personal jurisdiction of such court, waives any objection to venue in such court and consents to service of process by registered or certified mail, return receipt requested, at the last known address of such party.

**Permission to Reprint from Co-authors: Chapter 2**

July 16, 2018

Boniface Fosu
441 W 950 N
Logan, UT 84321
Boniface.fosu@aggiemail.usu.edu

Dear Dr. Wang:

I am preparing my dissertation in the Plants, Soils, and Climate department at Utah State University, in fulfillment of my degree program for Ph.D., Climate Science.

I am requesting your permission to include as a chapter in my dissertation the paper: Greenhouse gases stabilizing winter atmosphere in the Indo-Gangetic plains may increase aerosol loading, published in Atmospheric Science Letters, which you are listed as co-author. A footnote with citation information will appear on the first page of this chapter, and a copy of this permission letter will be included as an appendix to the dissertation.

Please indicate your approval of this request by filling in the form below granting permission to include this work in my dissertation. If you have any questions, please email me.

Thank you for your cooperation,
Boniface Fosu

_____

I hereby give permission to Boniface Fosu to reprint the following material in his dissertation.

Fosu, B. O., Wang, S. S., Wang, S. , Gillies, R. R. and Zhao, L. (2017), Greenhouse gases stabilizing winter atmosphere in the Indo-Gangetic plains may increase aerosol loading. Atmos. Sci. Lett., 18: 168-174. doi:10.1002/asl.739

Signed: Dr. Sheng-Hsiang Wang _____

July 16, 2018

Boniface Fosu
441 W 950 N
Logan, UT 84321
Boniface.fosu@aggiemail.usu.edu

Dear Dr. Zhao:

I am preparing my dissertation in the Plants, Soils, and Climate department at Utah State University, in fulfillment of my degree program for Ph.D., Climate Science.

I am requesting your permission to include as a chapter in my dissertation the paper: Greenhouse gases stabilizing winter atmosphere in the Indo-Gangetic plains may increase aerosol loading, published in Atmospheric Science Letters, which you are listed as co-author. A footnote with citation information will appear on the first page of this chapter, and a copy of this permission letter will be included as an appendix to the dissertation.

Please indicate your approval of this request by filling in the form below granting permission to include this work in my dissertation. If you have any questions, please email me.

Thank you for your cooperation,
Boniface Fosu

_____

I hereby give permission to Boniface Fosu to reprint the following material in his dissertation.

Fosu, B. O., Wang, S. S., Wang, S. , Gillies, R. R. and Zhao, L. (2017), Greenhouse gases stabilizing winter atmosphere in the Indo-Gangetic plains may increase aerosol loading. Atmos. Sci. Lett., 18: 168-174. doi:10.1002/asl.739

Signed: Dr. Lin Zhao _____

## License Agreement II: Materials for Chapter 3

July 10, 2018.

BAMS
45 Beacon Street Boston
MA 02108-3693

To the Permissions Editor:

I am in the process of preparing my dissertation in the department of plants, soils, and climate at Utah State University. I hope to complete my degree program in August 2018.

The article The 2014/15 Snowpack Drought in Washington State And Its Climate Forcing, of which I am first author, and which appeared in your journal (Vol. 97, No. 12, December 2016, pp 19-24) reports an essential part of my dissertation research. I would like permission to reprint it as a chapter in my dissertation, which may require some revision. Please note that USU sends every thesis and dissertation to ProQuest to be made available for reproduction.

I will include acknowledgment to the article on the first page of the chapter, as shown below. Copyright and permission information will be included in a special appendix. Please let me know if you would like a different acknowledgment.

Please indicate your approval of this request by signing in the space provided, and attach any other form necessary to confirm permission. If you charge a reprint fee for use of an article by the author, please indicate that as well.

If you have any questions, please contact me at the email below. Thank you for your assistance.

Boniface Fosu
(617) 548-7211
Boniface.fosu@aggiemail.usu.edu

---

Dear Mr. Fosu,

Your email regarding permissions was forwarded to me. This signed message constitutes permission to use the material requested below.

You may use your article as part of your dissertation with the following conditions:

+ please include the complete bibliographic citation of the original source, and

+ please include the following statement with that citation: ©American Meteorological Society. Used with permission.

Thank you for your query. If you need any further information, please feel free to contact me.

Best regards,

Rebecca Perriello
Senior Peer Review Support Associate &
Permissions Specialist

American Meteorological Society
45 Beacon Street, Boston, MA 02108
permissions@ametsoc.org | ametsoc.org

**License Agreement III: Materials for Chapter 4**

Copyrights

**Copyright and Licensing**

For all articles published in MDPI journals, copyright is retained by the authors. Articles

are licensed under an open access Creative Commons CC BY 4.0 license, meaning that

anyone may download and read the paper for free. In addition, the article may be reused

and quoted provided that the original published version is cited. These conditions allow

for maximum use and exposure of the work, while ensuring that the authors receive

proper credit.

In exceptional circumstances articles may be licensed differently. If you have specific

condition (such as one linked to funding) that does not allow this license, please mention

this to the editorial office of the journal at submission. Exceptions will be granted at the

discretion of the publisher.

**Reproducing Published Material from other Publishers**

It is absolutely essential that authors obtain permission to reproduce any published

material (figures, schemes, tables or any extract of a text) which does not fall into the

public domain, or for which they do not hold the copyright. Permission should be

requested by the authors from the copyrightholder (usually the Publisher, please refer to

the imprint of the individual publications to identify the copyrightholder).

Permission **is required** for:

1.  Your own works published by other Publishers and for which you did not retain copyright.

2.  Substantial extracts from anyones' works or a series of works.

3.  Use of Tables, Graphs, Charts, Schemes and Artworks if they are unaltered or slightly modified.

4.  Photographs for which you do not hold copyright.

    Permission **is not required** for:

1.  Reconstruction of your *own* table with data already published elsewhere. Please notice that in this case you must cite the source of the data in the form of either "Data from..." or "Adapted from...".

2.  Reasonably short quotes are considered *fair use* and therefore do not require permission.

3.  Graphs, Charts, Schemes and Artworks that are completely redrawn by the authors and significantly changed beyond recognition do not require permission.

**Permission to Reprint from Co-author: Chapter 4**

July 16, 2018

Boniface Fosu
441 W 950 N
Logan, UT 84321
Boniface.fosu@aggiemail.usu.edu

Dear Dr. Pegion:

I am preparing my dissertation in the Plants, Soils, and Climate department at Utah State University, in fulfillment of my degree program for Ph.D., Climate Science.

I am requesting your permission to include as a chapter in my dissertation the paper: Synoptic and Climate Attributions of the December 2015 Extreme Flooding in Missouri, USA, published in Water, which you are listed as co-author. A footnote with citation information will appear on the first page of this chapter, and a copy of this permission letter will be included as an appendix to the dissertation.

Please indicate your approval of this request by filling in the form below granting permission to include this work in my dissertation. If you have any questions, please email me.

Thank you for your cooperation,
Boniface Fosu

_____

I hereby give permission to Boniface Fosu to reprint the following material in his dissertation.

Fosu, B.; Wang, S.; Pegion, K. Synoptic and Climate Attributions of the December 2015 Extreme Flooding in Missouri, USA. Water 2018, 10, 350. doi:10.3390/w10040350

Signed: Dr. Kathleen Pegion _____

CURRICULUMN VITAE

Boniface Fosu
441 W 950 N
Logan, UT 84321
(617) 548-7211
Boniface.fosu@aggiemail.usu.edu

**Education**

**Utah State University**                                          **Logan, Utah**
Ph.D. Climate Science                                              2018

**Utah State University**                                          **Logan, Utah**
MSc Climate Science                                               2014

**Kwame Nkrumah University of Science and Technology**   **Kumasi, Ghana**
BSc. Meteorology and Climate Science                         2011

**Publications**

**Fosu, B. O**., S.-Y. Wang, Kathleen Pegion, 2018. Synoptic and Climate Attributions of the December 2015 Extreme Flood in Missouri, USA. Water. doi:10.3390/w10040350

**Fosu, B. O**., S.-Y. Wang, Sheng-Hsiang Wang, and Robert R. Gillies, 2017. Greenhouse Gases Stabilizing Winter Atmosphere in the Indo-Gangetic Plains May Increase Aerosol Loading. Atmospheric Science Letters. doi:10.1002/asl.739

**Fosu, B. O**., S.-Y. Wang, Jin-Ho Yoon, 2016. The 2014/15 Snowpack Drought in Washington State and its Climate Forcing. Bulletin of the American Meteorological Society. doi:10.1175/BAMS-D-16-0154.1

Wang, S.-Y., **B. Fosu,** R. R. Gillies, and P. M. Singh, 2015. The Deadly Himalayan Snowstorm of October 2014: Synoptic Conditions and Associated Trends. Bulletin of the American Meteorological Society. doi:10.1175/BAMS-D-15-00113.1

**Fosu, B. O.**, and S.-Y. Wang, 2014. Bay of Bengal: Coupling of pre-monsoon tropical cyclones with the monsoon onset in Myanmar. Climate Dynamics. doi:10.1007/s00382-014-2289-z

Wang, S.-Y., X. Jiang, and **B. Fosu**, 2014. Global eastward propagation signals associated with the 4-5-year ENSO cycle. Climate Dynamics. doi: 10.1007/s00382-014-2422-z

Wang, S.-Y., B. Buckley, J.-H. Yoon and **B. Fosu**, 2013. Intensification of pre-monsoon tropical cyclones in the Bay of Bengal and its impacts on Myanmar. Journal of Geophysical Research. doi: 10.1002/jgrd.50396

**Fosu, B. O.,** and Simon S.-Y. Wang, 2014. Coupling of Bay of Bengal Tropical Cyclones with the Myanmar Monsoon Onset. NOAA's Climate Prediction S & T Digest

**Presentations**

**International Meetings**

CLIVAR Open Science Conference. Qingdao, China, Sep 2016 (two posters) - [1] Explaining the widespread Extreme Events of December 2015. [2] Greenhouse Gases Stabilizing Winter Atmosphere in the Indo-Gangetic Plains May Increase Aerosol Loading.

The World Weather Open Science Conference. Montreal, Canada, Aug 2014 (poster) - Bay of Bengal: The Coupling of pre-monsoon tropical Cyclones with the monsoon onset in Myanmar.

**National Meetings**

98th American Meteorological Society Annual Meeting. Austin, Texas, Jan 2018 (poster) -Long-lead ENSO Predictions in the Framework of Recent ENSO Events.

SERDP & ESTCP Symposium. Washington DC, Nov 2017 (poster) - Useful Prediction of Climate Extreme Risk for Texas-Oklahoma at 4-6 Years.

The National Diversity in STEM Conference (SACNAS). Salt Lake City, Utah, Oct 2017 (talk) - Understanding Snowpack Drought and Its Climate Forcing.

42nd Climate Diagnostics & Prediction Workshop. Norman, Oklahoma, Oct 2017 (two posters) – [1] Understanding Long-lead ENSO predictions within the framework of recent ENSO events. [2] The Snowpack Drought in Washington State and its Climate Forcing.

Pacific Climate Workshop, Pacific Groove, California, Mar 2017 (talk) - The Snowpack Drought in Washington State and its Climate Forcing.

AGU Fall Meeting. San Francisco, Dec 2015 (poster) - Texas Floods, El Nino, and Climate Change.

40th Climate Diagnostics & Prediction Workshop, Denver, Colorado, Oct 2015 (poster) - Extended Inversions and worsening winter smog in the Indo-Gangetic Plains.

Pacific Climate Workshop, Pacific Groove, California, Mar 2015 (talk) - Fire and Ice: California Drought and "Polar Vortex" in a Changing Climate.

95th AMS Annual Meeting, Phoenix, Arizona, Jan 2015 (two posters) - [1] Bay of Bengal: The Coupling of pre-monsoon tropical Cyclones with the monsoon onset in Myanmar. [2] Intensification of pre-monsoon tropical cyclones in the Bay of Bengal

National Weather Association 39th Meeting, Salt Lake City, Utah, Oct 2014 (talk) - Precipitation in the Intermountain West: The ENSO-PDO Teleconnection.

38th Climate Diagnostics & Prediction Workshop. College Park, Maryland, Oct 2013 (talk) – Bay of Bengal Cyclones and the Myanmar Monsoon Onset in a Changing Climate.

**Regional Meetings**

2014 Spring Runoff Conference. Logan, Utah, Apr 2014 (talk) - Precipitation in the Intermountain West: The ENSO-PDO Teleconnection.

**Awards**

2017 Doctoral Student Researcher of the year            2017
College of Agriculture and Applied Sciences, USU, Logan, Utah

2016 Graduate Student Researcher of the year            2016
Department of Plants, Soils and Climate, Utah State University, Logan, Utah

Robert N. Love Scholarship Award            2015
College of Agriculture and Applied Sciences, USU, Logan, Utah

Robert N. Love scholarship award            2013
College of Agriculture and Applied Sciences, USU, Logan, Utah

**Travel Awards**

National Oceanic and Atmospheric Administration (NOAA) travel grant: 42nd Climate Diagnostics & Prediction Workshop, Norman, Oklahoma - Oct 2017

United States Geological Survey (USGS) grant: Pacific Climate Workshop travel support, Pacific Groove, California - Mar 2017

US Climate Variability and Predictability Program (US CLIVAR) and National Science Foundation (NSF) Early Career Scientist travel grant: CLIVAR Open Science Conference, Qingdao, China - Aug 2014

National Center for Atmospheric Research (NCAR) travel support: Community Earth System Model (CESM) Tutorials, Boulder, Colorado - Aug 2016

National Oceanic and Atmospheric Administration (NOAA) travel grant: 40th Climate Diagnostics & Prediction Workshop, Denver, Colorado - Oct 2015

National Science Foundation (NSF) support grant: The World Weather Open Science Conference, Montreal, Canada - Aug 2014

National Oceanic and Atmospheric Administration (NOAA) travel grant: 38th Climate Diagnostics & Prediction Workshop, College Park, Maryland - Oct 2013

**Professional Development**

CLIVAR Open Science Conference Early Career Scientist Workshop. Qingdao, China - Sep 2016

Community Earth System Model (CESM) Tutorials. NCAR Mesa Lab, Boulder - Aug 2016

The World Weather Open Science Conference Early Career Scientist Workshop. Montreal, Canada - Aug 2014